Volume 5 March, 2026 ISSN 1560-201X

# Journal of Remote Sensing and Environment

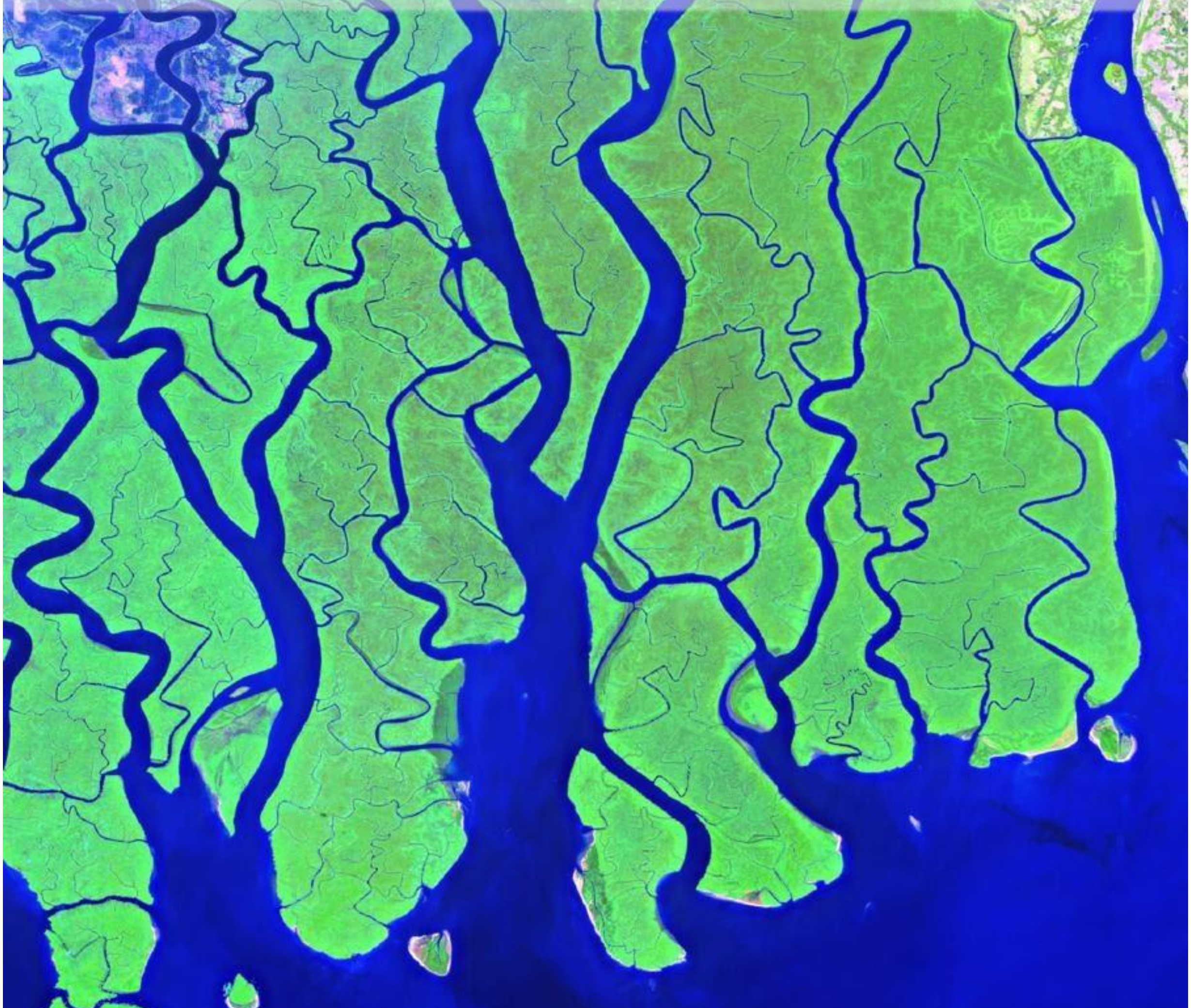

Bangladesh Space Research and Remote Sensing Organization
(SPARRSO)

ISSN: 1560-201X

Journal of Remote Sensing and Environment
Volume 5, 2026

**Published by:**

Bangladesh Space Research and Remote Sensing Organization (SPARRSO)
Agargaon, Sher-e-Bangla Nagar, Dhaka-1207, Bangladesh.
Phone: +88-02-48117692
Fax: +88-02-48111169
E-mail: admin@sparrso.gov.bd/jrse@sparrso.gov.bd

**Cover design:**

*The cover is designed based on the published article in this volume and the image has been collected from Sentinel 2B (ESA).*

ISSN: 1560-201X

# Journal of Remote Sensing and Environment

## Volume 5, 2026

Journal of Remote Sensing and Environment
Volume 5, 2026

# Editorial

The Bangladesh Space Research and Remote Sensing Organization (SPARRSO) has made significant contributions to the research of space technology and its applications over the years as a national space research center. Here, we are very pleased to publish the 5$^{th}$ volume of the Journal of Remote Sensing and Environment, which is a multidisciplinary journal published by Bangladesh Space Research and Remote Sensing Organization (SPARRSO).

In this volume, six research articles cover a wide range of topics, including the Earth's surface processes, natural resource monitoring, and disaster management, particularly in Bangladesh. The first article assesses the land use and land cover (LULC) change following a disastrous cycle (Remal) in the Sundarbans region of Bangladesh, which significantly contributed to our understanding of the impacts and showcases the application of satellite-based monitoring for effective disaster risk reduction. The second article focuses on the application of high-resolution satellite data (World View 0.3 m) for fisheries resource management in south-western Bangladesh, and significantly contributes to the fisheries resource mapping, which is a prerequisite for effective fisheries resource management in Bangladesh. The third article explores the compatibility of machine learning tools for mapping impervious surfaces of the Dhaka Metropolitan areas of Bangladesh, which contributes to the improvement of the methodological approach of mapping the impervious surface. Furthermore, the fourth article focuses on the dynamics of land cover, particularly the forest loss due to the Rohingya influx in Bangladesh. This article contributes to the advancement of Google Earth Engine (GEE)-based remote sensing techniques in the monitoring of the unwanted forest cover change in Cox's Bazar, Bangladesh. The fifth article is related to the comparative seasonality assessment of water extent area mapping in Hakaluki Haor, Bangladesh. This article contributes to the development of a Synthetic Aperture Radar (SAR)-based monitoring system, which can play a crucial role in water extent area mapping in the Haor region of Bangladesh. The sixth and final article examines urban expansion and population growth efficiency using sustainable development goal indicators in the Lower Turag River Basin, Bangladesh, which may play a critical role in developing the sustainable urban framework. Hence, we believe the published research article in this volume will significantly contribute to the advancement of remote sensing technology and will play a crucial role in different sectoral policies, strategic planning, and decision-making in South Asia, particularly in Bangladesh.

Furthermore, we would like to express our gratitude to the intellectual services of the relevant anonymous reviewers from different universities and research organizations of Bangladesh, who significantly improved the manuscript through their critical but insightful comments during the peer-review process.

**B. M. Refat Faisal; Ph.D.**
**Editor**
**Journal of Remote Sensing and Environment**

# Journal of Remote Sensing and Environment

## Volume 5, 2026


## Table of Content

# Assessing Land Cover Changes in the Sundarbans After Cyclone Remal Using Remote Sensing

Mahfuzul Islam[a] and Syed Hafizur Rahman[b*]

[a]*Graduate student, Department of Environmental Sciences, Jahangirnagar University, Savar, Dhaka-1342, Bangladesh.*

[b*]*Professor, Department of Environmental Sciences, Jahangirnagar University, Savar, Dhaka-1342, Bangladesh.*

**Corresponding author:* *hafizsr@juniv.edu* *(Syed Hafizur Rahman)*

**Article info**

***Keywords:***
*LULC,*
*Cyclone Remal,*
*Sundarbans,*
*NDVI,*
*GEE*

**Article History:**
Received-25 Oct 2025
Revised-01 Feb 2026
Accepted-08 Feb 2026
Published-31 March 2026

**DOI:**
https://doi.org/10.66268/jrse.2026.05.531843

**ABSTRACT**

The Sundarbans, the world's biggest mangrove forest and swamp, is notable for its biodiversity, ecology, and local economy. However, the ecosystem's distinct structure is increasingly vulnerable to both natural disasters, particularly cyclones, and pressurized human activity. The purpose of this study was to evaluate changes in land use and land cover (LULC) before and after Cyclone Remal (May 2024) in the Sundarbans region of Bangladesh, utilizing the Sentinel 2 imageries in the Google Earth Engine (GEE) platform. Here, the Normalized Difference Vegetation Index (NDVI) and supervised classification techniques have been used to assess the changes in landcover pattern, including the waterlogging, vegetation loss, and built-up areas, following the disaster. Here, an increase in water bodies (1.4%) and healthy vegetation (29.41%), where a decrease in built-up (0.17%), mudflat (1.83%), and less healthy vegetation (28.82%) have been observed, which crucially impacts the residents of the Sundarbans. Therefore, this study urges the utilization of satellite remote sensing-based management techniques to address the ecological and socioeconomic impacts that result from extreme weather events, such as cyclones.

## 1. Introduction

The world's largest mangrove forest, the Sundarbans, spans more than 10,000 sq.km from Bangladesh to India. Bangladesh owns over 62% of the forest. This biodiversity and ecological hotspot is home to more than 1186 species (Rahman & Begum, 2011). This environment is home to numerous uncommon and endangered species, including *Batagur baska*, *Pelochelys bibroni*, *Chelonia mydas*, *Panthera tigris*, and a variety of reptiles (Gopal & Chauhan, 2006). The Sundarbans offer special benefits to the local and national economies in addition to their ecological significance. Because of the Sundarbans' ecosystem services, people rely on this forest to manage their way of life. *Heritiera fomes, Nypa fruticans, Ceriops decandra, Rhizophora mucronata, Sonneratia apetala, Xylocarpus mekongensis, Excoecaria agallocha, Avicennia ofcinalis, Amoora cucullata, and Xylocarpus granatum* are among the economically useful plants found in the forest (Chaffey et al., 1985). Additionally, the Sundarbans are home to 873 species of invertebrates and more than 177 kinds of fish. The primary sources of revenue in this area include fishing, shrimp and crab farming, honey and wax gathering, wood and non-wood goods, and tourism (Islam & Islam, 2011). The Sundarbans have long been a focus for resource exploitation due to its great potential for ecological services and socioeconomic benefits. Additionally, overfishing, land reclamation, shrimp and crab farming, deforestation, and other resource extraction practices are causing environmental disturbances to the forest (Chowdhury & Maiti, 2016).

In addition, the Sundarbans' geographic location makes it extremely susceptible to natural calamities like cyclones, coastal floods, salinization, etc. One frequent natural disaster that frequently affects the surrounding area is a cyclone. There have been a few significant cyclones in these regions over the past few decades. The important ones include Sidr (2007), Aila (2009), Fani and Bulbul (2019), Amphan (2020), Yaas (2021), Sitrang (2022), and Remal (2024) (Ghosh & Mistri, 2023). The most recent of these was Remal, which happened on May 26, 2024. At 8:30 p.m. on May 26, Cyclone Remal made landfall on the coasts of West Bengal, India, and the southwest coast of Bangladesh. With strong storm surges, high tide, and exceptionally heavy rainfall, the maximum wind speed was between 111 and 120 km/h (IFRC, 2024a). According to the Department of Disaster Management (DDM) of the Ministry of Disaster Management and Relief (MoDMR), Cyclone Remal affected about 4.6 million people in 19 districts and killed 16 people in seven districts. About 807,023 people were evacuated to 9,424 shelters spread over 19 districts (IFRC, 2024b). The purpose of this study was to assess the immediate effects of Remal on the land usage and land cover of the Sundarbans. To determine the alterations, the landscape circumstances before and after the cyclone will be evaluated utilizing remote sensing and GIS technologies.

## 2. Materials and Methods

### 2.1 Study area

The study's primary emphasis was the Sundarbans mangrove forest in Bangladesh. Six upazilas that encompass Bangladesh's Sundarbans region are located in the country's southwest. These include Shyamnagar in the Satkhira district, Mongla, Morelganj, and Sharankhola in the Bagerhat district, and Dacope and Koyra in the Khulna district. These upazilas are all part of the Khulna division. The study region is between 22.2865° N, 88.9927° E and 22.5013° N, 89.9701° E, and between 22.6511° N, 89.4812° E and 21.6525° N, 89.2116° E. 11,955.814 sq.km of landscapes make up the entire research area.

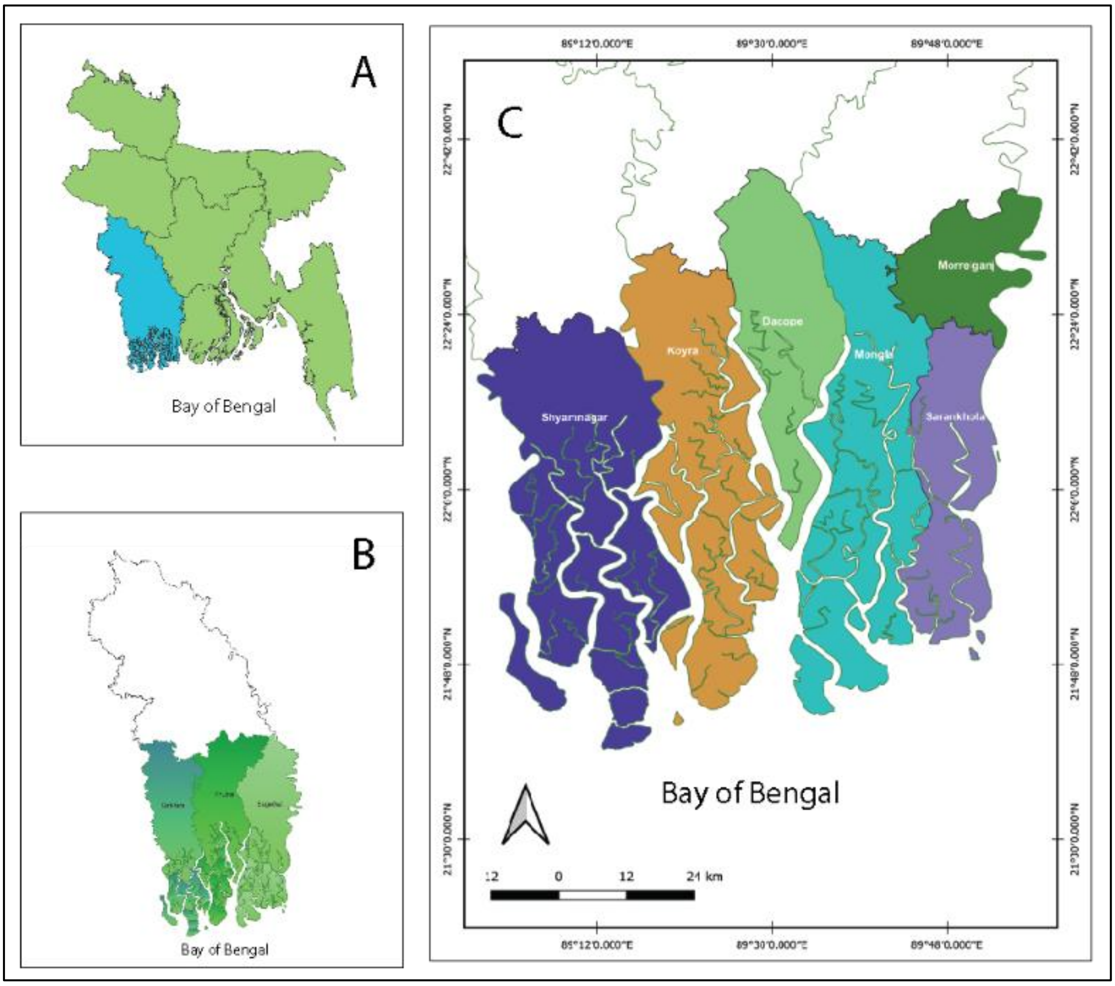


**Fig. 1.** Map of study area showing A) division boundary of Bangladesh, B) Khulna, Bagerhat, and Satkhira districts covering the Sundarbans, and C) area of interest with upazila boundary

### 2.2 Methodology

The study employed satellite imagery to assess the vegetation and landscape. The better resolution (10 m) of Sentinel-2 imagery led to its selection (ESA, 2015). The vegetation types and land use/cover were identified using the NDVI and supervised classification. The activities were carried out using QGIS 3.22 and Google Earth Engine (GEE). Since Cyclone Remal occurred on May 26, 2024, the earlier evaluation of the disaster covered the period from March 1 to May 20, 2024, and the post-disaster assessment covered the period from June 1 to October 10, 2024. Pre-disaster and post-disaster condition assessments were based on a total of 24 and 5 data sets (Cloud Coverage of <10%), respectively. Due to the limited time frame and the ongoing rainy season in Bangladesh, which makes it impossible to get cloudless satellite data, there were fewer satellite photos in the second section. In contrast, Sentinel 2 takes pictures between 10.30 and 10.35 AM, which coincides with the Sundarbans' low tide. The bias caused by the tidal influence is prevented because all of the photos are taken at the same time and under the same tidal conditions. Less than 20% of the data sets are cloud-covered. Table 1 provides information regarding the Sentinel 2B data set, whereas Table 2 provides the precise date of the data sets used.

**Table 1.** Sentinel 2B data specification and band combination (European Space Agency, 2015)

| Used Band | Sensor | Band | Sentinel-2B | | Resolution (meters) |
|---|---|---|---|---|---|
| | | | Central wavelength (nm) | Bandwidth (nm) | |
| Blue | MSI | 2 | 492.1 | 65 | 10 |
| Green | | 3 | 559 | 35 | 10 |
| Red | | 4 | 665 | 30 | 10 |
| Vegetation Red Edge | | 5 | 703.8 | 15 | 20 |
| Vegetation Red Edge | | 6 | 739.1 | 15 | 20 |
| Vegetation Red Edge | | 7 | 779.7 | 20 | 20 |
| NIR | | 8 | 833 | 115 | 10 |
| SWIR–Cirrus | | 11 | 1376.9 | 30 | 60 |
| SWIR | | 12 | 1610.4 | 90 | 20 |

**Table 2.** Sentinel 2B data used in this study

| Event (26 May, 2024) | |
|---|---|
| Before Disaster (From 01/03/2024 to 20/05/2024) | After Disaster (From 01/06/2024 to 10/10/2024) |
| 01/03/2024; 06/03/2024; 09/03/2024; 11/03/2024; 16/03/2024; 21/03/2024; 24/03/2024; 26/03/2024; 31/03/2024<br>05/04/2024; 10/04/2024; 13/04/2024; 15/04/2025; 18/04/2024; 20/04/2024; 23/04/2024; 25/04/2024; 28/04/2024; 30/04/2024<br>03/05/2024; 05/05/2024; 10/05/2024; 15/05/2024; 18/05/2024; | 04/06/2024<br>07/09/2024<br>17/09/2024<br>20/09/2024<br>22/09/2024 |

### 2.2.1 Satellite data pre-processing

The region of interest was chosen by uploading the research area's shape file as an asset in order to carry out the required activities in GEE. Next, Sentinel 2B data sets were gathered from the GEE image collection using a filter based on the maximum cloud coverage, region, and date range. The 'MSK_CLDPRB' band was then used for cloud masking (Mueller-Wilm et al., 2016; You et al., 2023; Luo et al., 2024). The cloud masking function was then applied to every time series image that had been gathered.

### 2.2.2 Normalized Difference Vegetation Index (NDVI)-based detection

A prominent method for assessing the quantity and health of vegetation in a region is the Normalized Difference Vegetation Index (NDVI). Since healthy vegetation strongly reflects near-infrared (NIR) light while plants absorb red light for photosynthesis, it compares the reflectance of the two spectrums. The "addNDVI" function was utilized to compute the normalized difference vegetation index (NDVI) from the cloud-free processed images. Equation 1 was used to calculate the NDVI (Goward et al., 1991; Pettorelli, 2013).

$$NDVI=\frac{NIR\text{-}Red}{NIR+Red} \quad \ldots\ldots\ldots\ldots\ldots\ldots\ldots\; (1)$$

Where, NIR = Near-infrared band (R8 band); Red = Red band (R4 Band)

The NDVI has a range of -1 to +1. Water, bogs, and murky water canals typically have a low reflection. Because of this, the NDVI value in these places is negative; in contrast, built-up areas have a range of NDVI values near zero. Because of the strong reflection, the vegetative region has a higher NDVI value. Table 3 provides the ranges to identify vegetation and other land use types based on the NDVI values study (Alphan & Derse, 2013; Gandhi et al., 2015; Myeong et al., 2006). The NDVI maps were visualized using QGIS.

**Table 3.** Land type and its corresponding NDVI Values

| Land use type | NDVI value range |
|---|---|
| Water | -1 to -0.0001 |
| Built-up and barren land | 0 to 0.180 |
| Partially grown vegetation | 0.181 to 0.340 |
| Well-grown vegetation | 0.341 to 1 |

### 2.2.3 Land Use and Land Cover (LULC) classification

For further evaluation, a supervised classification was done for each section of time series data sets. Supervised classification is the process of giving a class value to a group of grid cells based on the values of other grid cells that are comparable and have already been identified as typical of a class or group. It is done in a raster GIS database (Abburu & Golla, 2015). This means the user sets a group of classes by selecting some sample data and by the machine learning process, similar data is categorized into all the designated classes (Di Nunzio & Sordoni, 2014). A prepared sentinel map was projected and shown over the study region following the completion of the previously stated first data preparation. To identify the various types of land use within the research area, NDVI, NDWI (Normalize Difference Water Index), NDBI (Normalize Difference Builtup Index), BUI (Builtup Index), and IBI (Indexed Builtup Index) analyses were conducted. Next, based on the values of the indices, a number of points of interest were selected for five distinct classes. Table 4 lists the specific values obtained for each class. Water bodies, populated areas, mudflats, sparse vegetation, and dense vegetation were the classes. The classification method was then carried out by combining all of the classes into a single training data set. The before and after Remal scenarios received a total of 356 and 372 points, respectively. The study area was categorized using a "Random Forest" classifier. Each tree in this tree-based classifier casts a unit vote for the most popular class in order to classify an input vector (Belgiu & Drăguň, 2016; Pal, 2005; Parmar et al., 2019). There were fifty trees, one mean leaf population, and a half bag fraction. Following the classification, QGIS 3.22 was used to view the categorized map after it had been exported as a TIFF file.

**Table 4.** Land types and their descriptions.

| LULC class | Indices | Range | Description |
|---|---|---|---|
| Dense Vegetation | NDVI | >0.34 | Healthy vegetation with high chlorophyll quantity |
| Sparse Vegetation | NDVI | 0.18 to 0.34 | Vegetation with low chlorophyll quantity |
| Water body | NDWI | >0.00 | River, estuary, waterlogged areas, ocean. |
| Built-up areas | EBBI | (-)0.11 to 0.10 | Buildings, roads, and modified open barren areas |
| | IBI | >0.10 | |
| | NDVI | 0.00 to 0.18 | |
| Mudflats | EBBI | >0.10 | A stretch of muddy land left uncovered at low tide |
| | BUI | 0.00 to 0.10 | |

*Note: EBBI-Enhanced Built-up and Barrenness Index; IBI-Index of Biological Integrity; BUI-Buildup index*

### 2.2.4 Accuracy assessment

To test the accuracy of the classified images, five more classes were created corresponding to the previous ones. These were used as validation data against the classified images. In the process of accuracy assessment confusion matrix was created using the 'error matrix' function, where it compared the actual validated values (class) with the predicted values (classification) (Das et al., 2022). For the pre-disaster operation, 300 random points were selected, and for the post-disaster operation, 290 random points were selected using the multiple ROI creation function on QGIS. The acquired value of these parameters of the pre-disaster and post-disaster scenarios has been given in Table 5.

**Table 5.** Accuracy assessment result of the classified map of the pre-disaster scenario.

| Metric | Value (pre-disaster) | Value (post-disaster) |
|---|---|---|
| Producers Accuracy Class 1 | 1 | 1 |
| Producers Accuracy Class 2 | 0.944444 | 0.53125 |
| Producers Accuracy Class 3 | 0.125 | 0.75 |
| Producers Accuracy Class 4 | 0.69697 | 0.73913 |
| Producers Accuracy Class 5 | 0.918919 | 0.944444 |
| Users Accuracy Class 1 | 0.909091 | 0.878049 |
| Users Accuracy Class 2 | 0.73913 | 0.809524 |
| Users Accuracy Class 3 | 0.333333 | 0.375 |
| Users Accuracy Class 4 | 0.884615 | 0.772727 |
| Users Accuracy Class 5 | 0.944444 | 0.971429 |
| Overall Accuracy | 0.854167 | 0.854167 |
| Kappa Coefficient | 0.809692 | 0.809692 |

## 3. Results and Discussion

### 3.1 Spatial distribution of NDVI

There were minor variations across the water bodies in the two scenarios based on the NDVI assessment. Before the occurrence of the disaster, a total of 1961.044 sq.km of land was used as a body of water, whereas after the disaster, it spanned nearly 1952.23 sq.km. The data shows that the area of partially established vegetation has shrunk from 1741.88 sq.km to 534.34 sq.km. On the other hand, there was a noticeable rise in the quantity of healthy vegetation. It changed from 2182.67 sq.km to 3439.366 sq.km (Fig. 2).

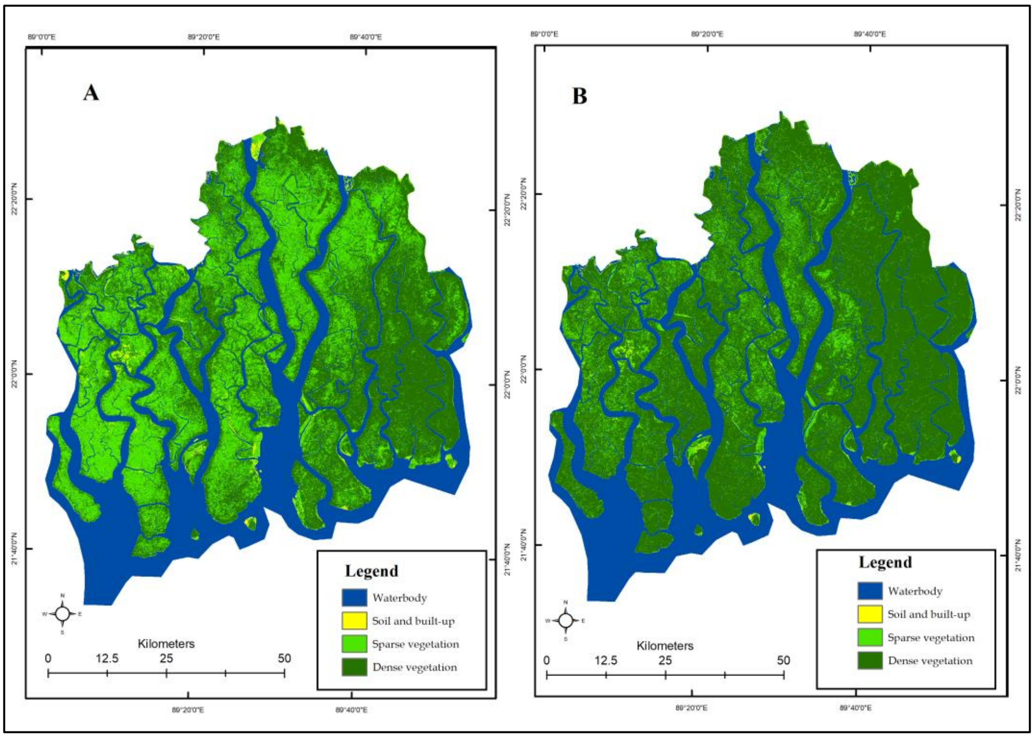


**Fig. 2.** The spatial distribution of the NDVI in A) Pre-disaster and B) Post-disaster situations along the study area.

### 3.2 Assessment of LULC classification

The LULC assessment shows the variations in the pre-disaster and post-disaster scenarios along the study sites. The Fig. 3 shows the categorized images, while Table 6 provide the classification reports. Following the disaster, the area of the water body increased in both NDVI and LULC classes assessment. This suggests that the cyclone caused waterlogging in the coastal districts. On the other hand, following the event, the number of built-up areas decreased. This demonstrates that there was waterlogging in the area where people reside. Similar information may be found in the news, where it was stated that during Cyclone Remal, the Sundarbans coastal region was submerged under ten feet of water (Somoy National Desk, 2024). This could pose a serious risk to the locals because the water is primarily brine or saltwater (Burman et al., 2013). The waterlogging and salinization would pose a serious threat to agricultural activities (Song et al., 2017; Zhao et al., 2019). The source of freshwater is another critical issue during this event. Also, social unrest and economic disruption may result from these issues. Additionally, excessive salinization may cause ecological disruption (Assiya et al., 2020; Gaybullaev et al., 2012).

However, this study reports an increase in well-grown vegetation in both NDVI and supervised categorization, which may be the result of less human disturbance and a significant dose of nutrients to the offshore due to the cyclone. There was a noticeable decrease in the area of mudflats and sparse vegetation, indicating that healthy vegetation currently covers these areas. The forest ecology may experience more chain reactions as a result of this alteration. According to Cannicci et al. (2008), Lobón-Cerviá et al. (2015), and Rasquinha et al. (2021), this could improve the ecological balance among the species.

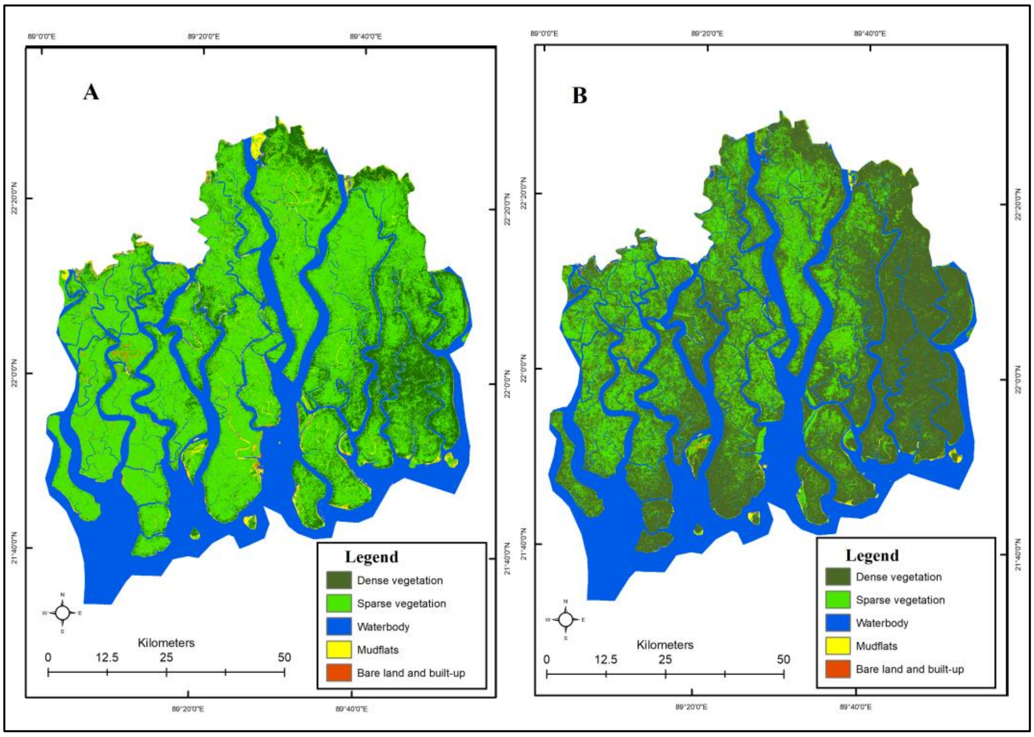


**Fig. 3**. LULC map of A) Pre-disaster and B) Post-disaster situations along the study area

**Table 6.** Percentage of LULC classes of the pre-disaster situation

| Class | Pre-disaster | | Post-disaster | |
|---|---|---|---|---|
| | Area (Sq.km) | Percentage % | Area (Sq.km) | Percentage % |
| Dense vegetation | 1030.20 | 14.65 | 3162.76 | 44.06 |
| Sparse vegetation | 4405.41 | 51.1 | 2364.62 | 22.28 |
| Waterbody | 2697.05 | 30.37 | 2809.46 | 31.77 |
| Mudflats | 201.88 | 2.39 | 40.07 | 0.56 |
| Built-up area | 159.17 | 1.49 | 116.76 | 1.32 |

## 4. Conclusions

This study assesses the impact of Cyclone Remal, which occurred on May 26, 2024, along the Sundarbans in Bangladesh, utilizing the NDVI and LULC-based classification. Waterlogging situation has been observed in populated areas, which has ultimately impacted on the local inhabitants along the coast of Bangladesh. Besides, a noticeable shift from sparse vegetation to mudflats and healthy vegetation, which suggested that the forest ecosystem had improved. It is necessary to make informed plans to preserve the Sundarbans ecosystem and sustainably utilize its resources. The Sundarbans are mostly threatened by humans who make their living and engage in different illicit activities within the forest, rather than by the natural environment. To avoid social and ecological upheaval in this region, the government can consider the evidence-based strategies more comprehensively.

**Acknowledgments**

The authors would like to thank the USGS for providing the satellite data.

**Data availability**

The data will be made available upon request to the corresponding author.

**Conflict of interest**

The authors declare that there is no conflict of interest regarding the publication of this paper.

## References

Abburu, S., Golla, S. B. (2015). Satellite image classification methods and techniques: A review. International Journal of Computer Applications, 119 (8). Doi: 10.5120/21088-3779

Alphan, H., Derse, M. A. (2013). Change detection in Southern Turkey using normalized difference vegetation index (NDVI). Journal of Environmental Engineering and Landscape Management, 21(1), 12–18. Doi:10.3846/16486897.2012.663091

Assiya, M., Jilili, A., Sanim, B., Botagoz, I., Zhassulan, S. (2020). Water balance of the Small Aral Sea. Environmental Earth Sciences, 79(3). https://doi.org/10.1007/s12665-019-8739-5

Belgiu, M., Drăguţ, L. (2016). Random forest in remote sensing: A review of applications and future directions. ISPRS Journal of Photogrammetry and Remote Sensing, 114, 24–31. https://doi.org/10.1016/j.isprsjprs.2016.01.011

Burman, D., Bandyopadhyay, B. K., Mandal, S., Mandal, U. K., Mahanta, K. K., Sarangi, S. K., Maji, B., Rout, S., Bal, A. R., Gupta, S. K. (2013). Land shaping—a unique technology for improving productivity of coastal land. Bulletin No. CSSRI/Canning Town/Bulletin/2013/02, 38.

Cannicci, S., Burrows, D., Fratini, S., Smith III, T. J., Offenberg, J., Dahdouh-Guebas, F. (2008). Faunal impact on vegetation structure and ecosystem function in mangrove forests: a review. Aquatic Botany, 89(2), 186–200. https://doi.org/10.1016/j.aquabot.2008.01.009

Chaffey, D., Miller, F., Sandom, J. (1985). A forest inventory of the Sundarbans, Bangladesh. https://agris.fao.org/search/en/providers/122621/records/647396913ed73003714cd01d

Chowdhury, A., Maiti, S.K. (2016). Identifying the source and accessing the spatial variations, contamination status, conservation threats of heavy metal pollution in the river waters of Sunderban biosphere reserve, India. Journal of Coastal Conservation 20, 257–269. https://doi.org/10.1007/s11852-016-0436-x

Das, C., Sahoo, A. K., Pradhan, C. (2022). Chapter 12 - Multicriteria recommender system using different approaches. In S. Mishra, H. K. Tripathy, P. K. Mallick, A. K. Sangaiah, G. S. Chae (Eds.), Cognitive Big Data Intelligence with a Metaheuristic Approach (pp. 259–277). Academic Press. https://doi.org/https://doi.org/10.1016/B978-0-323-85117-6.00011-X

Di Nunzio, G. M., Sordoni, A. (2014). Chapter 2 - Picturing Bayesian Classifiers: A Visual Data Mining Approach to Parameters Optimization. In Y. Zhao, Y. Cen (Eds.), Data Mining Applications with R (pp. 35–61). Academic Press. https://doi.org/https://doi.org/10.1016/B978-0-12-411511-8.00002-5

ESA (European Space Agency)- Sentinel-2. (2015). https://www.esa.int/Applications/Observing_the_Earth/Copernicus/Sentinel-2

ESA (European Space Agency). (2015). Sentinel-2 User Handbook (2nd ed., Vol. 1). European Space Agency.

Gandhi, G. M., Parthiban, S., Thummalu, N., Christy, A. (2015). NDVI: Vegetation change detection using remote sensing and GIS–A case study of Vellore District. Procedia Computer Science, 57, 1199–1210. https://doi.org/10.1016/j.procs.2015.07.415

Gaybullaev, B., Chen, S.C., Kuo, Y. M. (2012). Large-scale desiccation of the Aral Sea due to over-exploitation after 1960. Journal of Mountain Science, 9, 538–546. https://doi.org/10.1007/s11629-012-2273-1

Ghosh, S., Mistri, B. (2023). Cyclone-induced coastal vulnerability, livelihood challenges and mitigation measures of Matla-Bidya inter-estuarine area, Indian Sundarban. Natural Hazards, 116, 3857–3878. https://doi.org/10.1007/s11069-023-05840-2

Gopal, B., Chauhan, M. (2006). Biodiversity and its conservation in the Sundarban Mangrove Ecosystem. Aquatic Sciences, 68(3), 338–354. https://doi.org/10.1007/s00027-006-0868-8

Goward, S. N., Markham, B., Dye, D. G., Dulaney, W., Yang, J. (1991). Normalized difference vegetation index measurements from the advanced very high resolution radiometer. Remote Sensing of Environment, 35(2–3), 257–277.

IFRC (International Federation of Red Cross and Red Crescent Societies). (2024a). Bangladesh: Cyclone Remal. IFRC.Org. https://www.ifrc.org/emergency/bangladesh-cyclone-remal#:~:text=Severe%20cyclonic%20storm%20Remal%20made,feet%20in%20the%20coastal%20districts.

IFRC (International Federation of Red Cross and Red Crescent Societies). (2024b). Operation update: Bangladesh | Cyclone Remal.

Islam, K. M. N., Islam, M.N. (2011). Economics of extraction of products from Sundarbans reserve forest. Bangladesh Journal of Agricultural Economics, 34, 1(2), 29-53. https://doi.org/10.22004/AG.ECON.199332

Lobón-Cerviá, J., Hess, L. L., Melack, J. M., Araujo-Lima, C. A. R. M. (2015). The importance of forest cover for fish richness and abundance on the Amazon floodplain. Hydrobiologia, 750, 245–255. https://doi.org/10.1007/s10750-014-2040-0

Luo, J., Xie, M., Wu, Q., Luo, J., Gao, Q., Shao, X., Zhang, Y. (2024). Early Crop Identification Study Based on Sentinel-1/2 Images with Feature Optimization Strategy. Agriculture, 14(7), 990. https://doi.org/10.3390/agriculture14070990

Mueller-Wilm, U., Devignot, O., Pessiot, L. (2016). Sen2Cor configuration and user manual. Telespazio VEGA Deutschland GmbH: Darmstadt, Germany.

Myeong, S., Nowak, D. J., Duggin, M. J. (2006). A temporal analysis of urban forest carbon storage using remote sensing. Remote Sensing of Environment, 101(2), 277–282. https://doi.org/10.1016/j.rse.2005.12.001

Pal, M. (2005). Random forest classifier for remote sensing classification. International Journal of Remote Sensing, 26(1), 217–222. https://doi.org/10.1080/01431160412331269698

Parmar, A., Katariya, R., Patel, V. (2019). A review on random forest: An ensemble classifier. International Conference on Intelligent Data Communication Technologies and Internet of Things (ICICI) 2018, 758–763.

Pettorelli, N. (2013). The normalized difference vegetation index. Oxford University Press, USA.

Rahman, M. R., Begum, S. (2011). Land cover change analysis around the Sundarbans Mangrove Forest of Bangladesh using remote sensing and GIS application. Journal of Science Foundation, 9(1–2), 95–107. https://doi.org/10.3329/jsf.v9i1-2.14652

Rasquinha, D.N., Mishra, D.R. (2021). Tropical cyclones shape mangrove productivity gradients in the Indian subcontinent. Sci Rep 11, 17355 . https://doi.org/10.1038/s41598-021-96752-3

Somoy National Desk. (2024). Cyclone Remal: Sundarbans under 10-feet water. Somoy Media Limited. (Accessed in June 2024)

Song, T., Xu, H., Sun, N., Jiang, L., Tian, P., Yong, Y., Yang, W., Cai, H., Cui, G. (2017). Metabolomic analysis of alfalfa (Medicago sativa L.) root-symbiotic rhizobia responses under alkali stress. Frontiers in Plant Science, 8, 1208. https://doi.org/10.3389/fpls.2017.01208

You, N., Dong, J., Li, J., Huang, J., Jin, Z. (2023). Rapid early-season maize mapping without crop labels. Remote Sensing of Environment, 290, 113496. https://doi.org/10.1016/j.rse.2023.113496

# Application of High-Resolution Satellite Data for Fisheries Resources Management in South-western Bangladesh: A Case of Rupsha Upazila, Khulna District

Md. Abdur Rahman-Al-Mamun[a], M. Mahmudur Rahman[b*], Mohammad Imrul Islam[c], Zebunnesa Khatoon[d]

[a]*Scientific Officer, Bangladesh Space Research and Remote Sensing Organization (SPARRSO), Agargaon, Sher-e-Bangla Nagar, Dhaka-1207, Bangladesh.*

[b*]*Member, Bangladesh Space Research and Remote Sensing Organization (SPARRSO), Agargaon, Sher-e-Bangla Nagar, Dhaka-1207, Bangladesh.*

[c] *Senior Scientific Officer, Bangladesh Space Research and Remote Sensing Organization (SPARRSO), Agargaon, Sher-e-Bangla Nagar, Dhaka-1207, Bangladesh.*

[d]*Senior Scientific Assistant, Bangladesh Space Research and Remote Sensing Organization (SPARRSO), Agargaon, Sher-e-Bangla Nagar, Dhaka-1207, Bangladesh.*

**Corresponding author: mahmud@sparrso.gov.bd (M. Mahmudur Rahman)*

**Article info**

***Keywords:***
*Water Bodies,*
*Fisheries Resources,*
*Remote Sensing and GIS,*
*Satellite Imagery*

**Article History:**
Received-09 Nov 2025
Revised-22 Feb 2026
Accepted-03 March 2026
Published- 31 March 2026

**DOI:**
https://doi.org/10.66268/jrse.2026.05.180376

**ABSTRACT**

A fishery resource inventory is helpful for planning, management, and development of fisheries resources in any region. Therefore, this study has been conducted to identify different types of waterbodies and to delineate fisheries resources in the south-western part of Bangladesh (Rupsha Upazila, Khulna District), which plays a crucial role in providing the country's fish production. In this study, Very High Spatial Resolution (VHSR) satellite data of WorldView-3 were used to identify different types of water bodies and map the extent of those water bodies, using the on-screen digitization techniques. A total of seven different types of waterbodies (river, canal, beel, low-lying area, fish farm, pond, and others) were identified, grouped into open (1,240 ha) and closed (4,198ha) waterbodies. The open waterbody includes river, canal, beel, and low-lying area, which covers 491 ha, 160 ha, 564 ha, and 24 ha, respectively. On the other hand, the closed waterbodies cover fish farms, ponds, and others, which occupy 3,997 ha, 84 ha, and 118 ha, respectively. After the post-classification, the Kappa coefficient as well as overall accuracy are 0.92 and 95.80%, respectively. Regardless of the digitization techniques employed, this study presents a baseline database of waterbodies in the study area, which will be highly beneficial for planning optimal fisheries resource production and management in the south-western region of Bangladesh and/or in the region of similar interest.

## 1. Introduction

Water coverage on the land surface is a crucial part of the water cycle, and mapping waterbodies using satellite imagery is highly suitable for conducting surveys in remote areas. Surface water on Earth is used for transportation, irrigation, fishing, and other human activities. Human intervention can alter water levels on the Earth's surface (Li et al., 2015). Monitoring waterbodies plays a vital role in the sustainable use of water resources. Remote sensing is a technique that uses scalable data, enables convenient data acquisition, and precisely monitors and maps large-scale surface water features (Ji et al., 2022). For this purpose, remote sensing is an excellent tool for surface water management, as it can identify and map surface waterbodies, and has been used for the identification and mapping of water coverage for several decades (Bijeesh & Narasimhamurthy, 2020; Deoli et al., 2021). Remote sensing techniques are significant for providing real-time data and rapid access to land surface information, making them a reliable method for monitoring surface waterbodies (Chen et al., 2004). To produce thematic maps of land use or highlight waterbodies, various satellite data have been employed to capture spatial, temporal, and spectral variations (Deoli et al., 2021). Remote sensing imagery obtained from satellite or airborne platforms contains valuable information that is highly convenient for mapping preparation through image processing and analysis (Bijeesh & Narasimhamurthy, 2020). Although substantial efforts have been made to identify and delineate water bodies using remote sensing techniques, challenges persist due to the landscape complexity of the study area, data selection, and classification approaches (Deoli et al., 2021).

Additionally, numerous techniques have been applied to extract features from satellite imagery (Masser, 2001; Peng et al., 2018). McFeeters (1996) proposed the Normalized Difference Water Index (NDWI), based on the spectral characteristics of waterbodies, to differentiate surface water from vegetation. Different water indices, including the Water Ration Index (WRI), Normalized Difference Water Index (NDWI), Modified Normalized Difference Water Index (MNDWI), and Automated Water Extraction Index (AWEI), are commonly used for mapping natural waterbodies (Jiang et al., 2014). Different approaches have been widely utilized to delineate water bodies from satellite sensor data. These include semi-automated or automated classification techniques and on-screen digitization. The automated approaches cover different spectral indices, like NDWI, MNDWI, and machine learning classifiers, which are convenient for larger-scale mapping of water resources; however, it is challenging for water area extraction while high-resolution satellite sensor data is used for mixed pixel and complex boundary conditions (McFeeters, 1996; Xu, 2006; Feyisa et al., 2013). Each application method has its own merits and demerits (Subramaniam et al., 2011; Li et al., 2015). In contrast, visual interpretation and on-screen digitization using digital satellite data are considered reliable because they utilize spectral and other contextual information for image interpretation, as well as the accuracy of high-resolution imagery, which is used as a reference tool (Ozesmi & Bauer, 2002). Based on the complexity of the study area, the on-screen digitization method was selected for accurate water coverage area calculation.

Inventorying waterbodies is a challenging task due to their small sizes, irregular shapes, and the limited availability of high-resolution satellite data. Several factors affect the accuracy of waterbody mapping, including low-albedo surfaces, the physical structure of waterbodies, and the chemical composition of water (Jakovljević et al., 2019). In urban areas, it is difficult to identify water coverage in small waterbodies with complex geographical structures. This complexity often results in mixed pixels, which can confuse image interpreters (Lu et al., 2011; Donchyts et al., 2016). Moreover, discrepancies have been observed when comparing remotely sensed data with ground-truth information from the study area (Deoli et al., 2021). Rupsha Upazila under Khulna District is located at the south-western corner of Bangladesh, and it consists of both open-water and closed-water bodies. This area has high potential and contributes a large amount of fish production from both capture and culture fisheries. However, there is no class-wise digital database or map of fisheries resources in this area to support effective management. Therefore, special emphasis was placed on developing a fisheries resource inventory for the study area to facilitate proper management. This study is based on the following hypothesis: remote sensing techniques supplemented by in situ observations can effectively estimate and map water bodies for fisheries resources. Any differences, if exists, between the estimated area and the extent of the water body (measured from remote sensing information supplemented by in-situ measurements) that are significantly greater would have been expected through the sampling errors alone. This study utilized high-resolution satellite data to identify different types of waterbodies, create a digital database of water coverage, and map various waterbodies in the study area.

## 2. Materials and Methods

### 2.1 Study area

Considering the significance of fisheries resources, richness of floral and faunal biodiversity, the Rupsha Upazila of Khulna District, Bangladesh, was selected as the study area, which lies between 22°43′N to 22°52′N and 89°33′E to 89°41′E, covering a total area of 120 square kilometers (Fig. 1). This area, containing both open and closed water resources, plays a vital role in breeding, feeding, and nursery grounds for many freshwaters as well as coastal aquatic species, with the blessing of active tidal action.

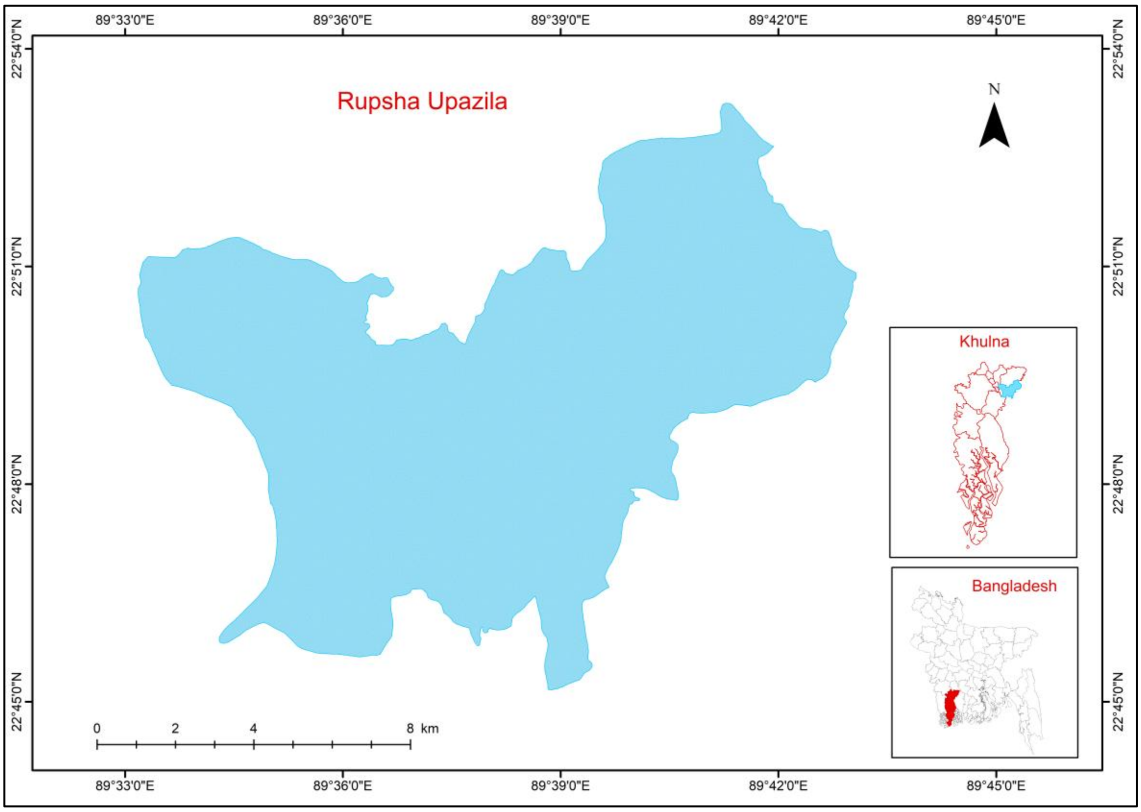


**Fig. 1**. Map of the study area showing the area of interest along with country boundary

### 2.2 Data used

For this study, high-resolution satellite data (WorldView-3 owned by Maxar Technologies, Table 1) acquired on 24$^{th}$ January 2022 and 22$^{nd}$ February 2022, along with field observation data, were used. Multispectral band combinations were used for image interpretation and water body delineation, with bands 6, 5, and 4 selected to enhance visual discrimination.

**Table 1.** The detailed specification of the satellite data used

| Satellite data | Acquisition date | Spectral range | Band name | Spectral band | GSD (Ground Sample Distance) |
|---|---|---|---|---|---|
| WorldView-3 (0.31 m) | 24/01/2022 22/02/2022 | Panchromatic Band (1) | 450 – 800 nm | | Nadir: 0.31 m, 20° off-nadir: 0.34 m |
| | | Multispectral Bands (MS) (8) | Coastal Blue | 400 – 450 nm | Nadir: 1.24 m, 20° off-nadir: 1.38 m |
| | | | Blue | 450 – 510 nm | |
| | | | Green | 510 – 580 nm | |
| | | | Yellow | 585 – 625 nm | |
| | | | Red | 630 – 690 nm | |
| | | | Red Edge | 705 – 745 nm | |
| | | | Near-IR1 | 770 – 895 nm | |
| | | | Near-IR2 | 860 – 1040 nm | |
| Sentinel 2 | 01/11/2022 30/11/2022 (Median composite) | Multispectral Bands (MS) | Blue | 490 nm | 10 m |
| | | | Green | 560 nm | |
| | | | Red | 665 nm | |

### 2.3 Methods

#### 2.3.1 Satellite data processing

Very high-resolution multispectral satellite imagery acquired from WorldView-3 (WV-3) with panchromatic resolution of 0.31 m and multispectral (8 bands) of 1.24 m data at nadir was used. The imagery was preprocessed and orthorectified Level-2A products that were suitable for direct mapping applications. Radiometric and geometric corrections had been performed by the data provider before delivery. Geometric accuracy was checked with other available geo-referenced images and found that it was adequate for further processing and mapping activity. Separate image swaths corresponding to different parts of the study area were integrated through mosaicking to create a unified dataset representing the complete study area. The final mosaic image was subsequently used as the base layer for feature delineation and digitization. Sentinel 2 multispectral imagery of the European Space Agency (ESA) with 10 m spatial resolution and median value was used for better understanding during image interpretation. All imagery was maintained in the Universal Transverse Mercator (UTM 45N) projection referenced to the WGS-84 datum to ensure spatial consistency throughout the analysis. All the analyses were performed using ArcMap 10.8 software.

### 2.3.2 Digitization of different features

The multi-spectral (Bands 6, 5, and 4 in RGB) and panchromatic WV-3 image was displayed on the computer screen one on top of another. Water bodies appeared in dark blue color and dark tone while displayed on multispectral and panchromatic satellite images, respectively. An independent interpreter identified water bodies on the computer screen, and on-screen manual digitization was conducted to delineate different types of water bodies from the processed high-resolution mosaic image. Different features were digitized at a fixed on-screen scale of 1:1000 ratio to establish high positional accuracy and consistency. Water body boundaries were manually traced using polygon geometry in ArcMap 10.8 software. The high spatial resolution (0.31 m) aided easy identification of waterbody edges. Water bodies were identified based on the spectral characteristics (bands 6, 5, and 4 in RGB). Another inspection was done on the digitized Geographic Information System (GIS) layer on top of the multispectral and panchromatic satellite image, corrected digitization errors, and ensured spatial consistency. The finalized vector layers were exported to delineate different water bodies, and statistical geometric calculation was performed to prepare an area coverage database. The details of the methods have been outlined in Fig. 2.

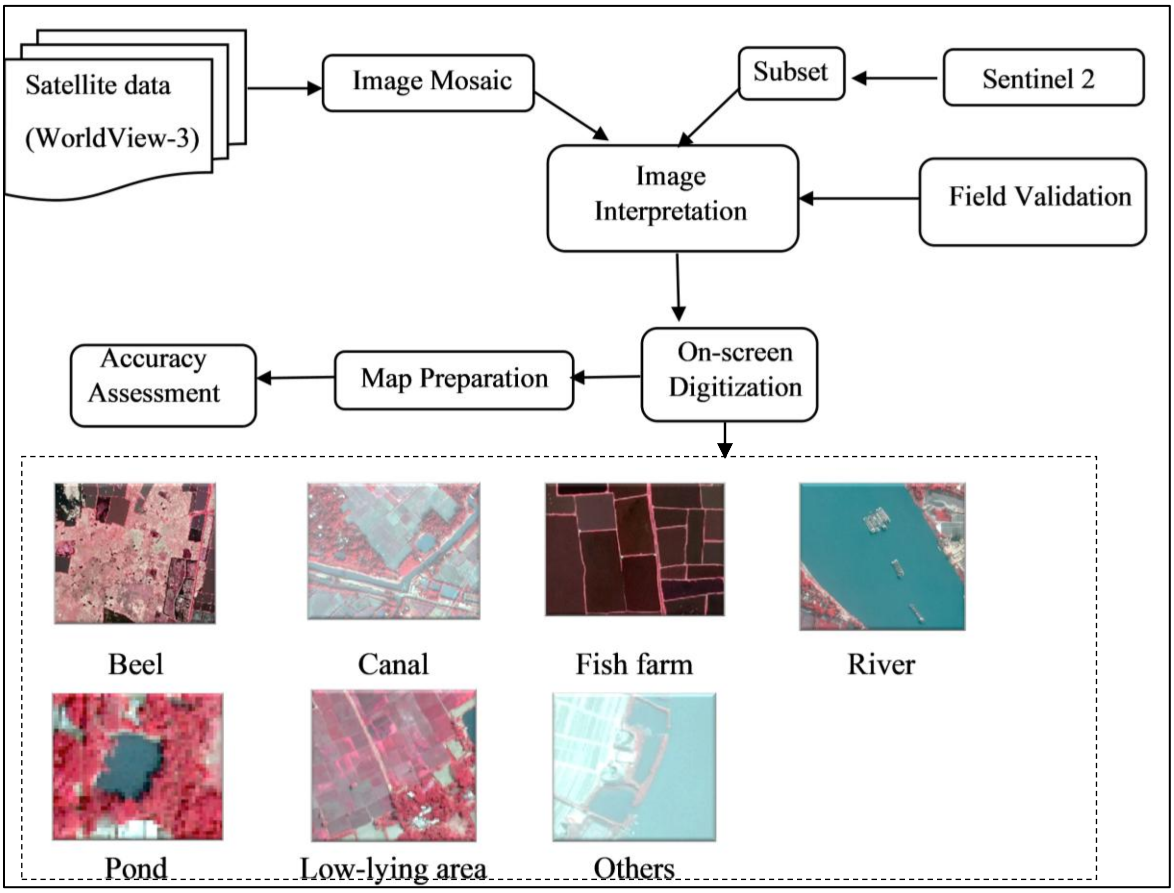


**Fig. 2.** Methodological workflow and different waterbodies during on-screen digitization

### 2.3.3 Accuracy assessment

Stratified random sampling was used for the accuracy assessment. The total area of each stratum (or mapping unit) was calculated, and sampling points were randomly distributed in proportion to their areal extent. Features of those sampling points were validated through Google Earth Explorer and Cohen's Kappa coefficient. The kappa is calculated following the methods of Cohen (1960). The distribution of sampling points across different land cover features is presented in Table 2. Besides, the field validation was conducted through ground-truth visits, where the Global Positioning System-based location information and relevant photographs of different features were collected during the field campaign.

$$P_o = \text{Overall Accuracy}$$

$$P_e = \sum_i \frac{R_i \times C_i}{N^2}$$

$$\kappa = \frac{P_o - P_e}{1 - P_e}$$

**Table 2.** Distribution of sampling points across different land cover features

| Feature name | Area (ha scale) | Points taken |
|---|---|---|
| River | 491 | 25 |
| Canal | 160 | 8 |
| Beel | 564 | 30 |
| Low Lying Area | 24 | 3 |
| Fish farm | 3997 | 200 |
| Pond | 84 | 10 |
| Others | 118 | 10 |

## 3. Results

Considering the objectives of this study, a total of seven water bodies (open and closed) have been identified and described in the following sections. Among them, four types were classified as open waterbodies, while the remaining three were categorized as closed waterbodies.

### 3.1 Open water body

Four types of open water bodies were identified in the study area, including rivers, canals, beels, and low-lying areas, covering 1,240 hectares and accounting for 22.8% of the total fisheries habitats in Rupsha Upazila (Fig. 3). The three major rivers (Bhairab, Rupsha, and Atharobanki) are traversing in this region, which play a crucial role in fisheries resource management in the south-western region of Bangladesh. Besides, numerous canals were observed, covering an area of 160 hectares and accounting for 12.9% of the total open water bodies. These canals are directly or indirectly connected to the rivers and serve multiple functions, including the drainage of household wastewater, rainfall runoff, and the transport of hydro-sediment through active tidal action. This tidal influence enhances the ecological functions of these water bodies by providing feeding, breeding, and nursery grounds for a variety of coastal flora and fauna. The smallest share of open water bodies is occupied by low-lying areas, covering 24 hectares and contributing 2% of the total open water bodies. These areas are relatively depressed and retain water for six to nine months of the year.

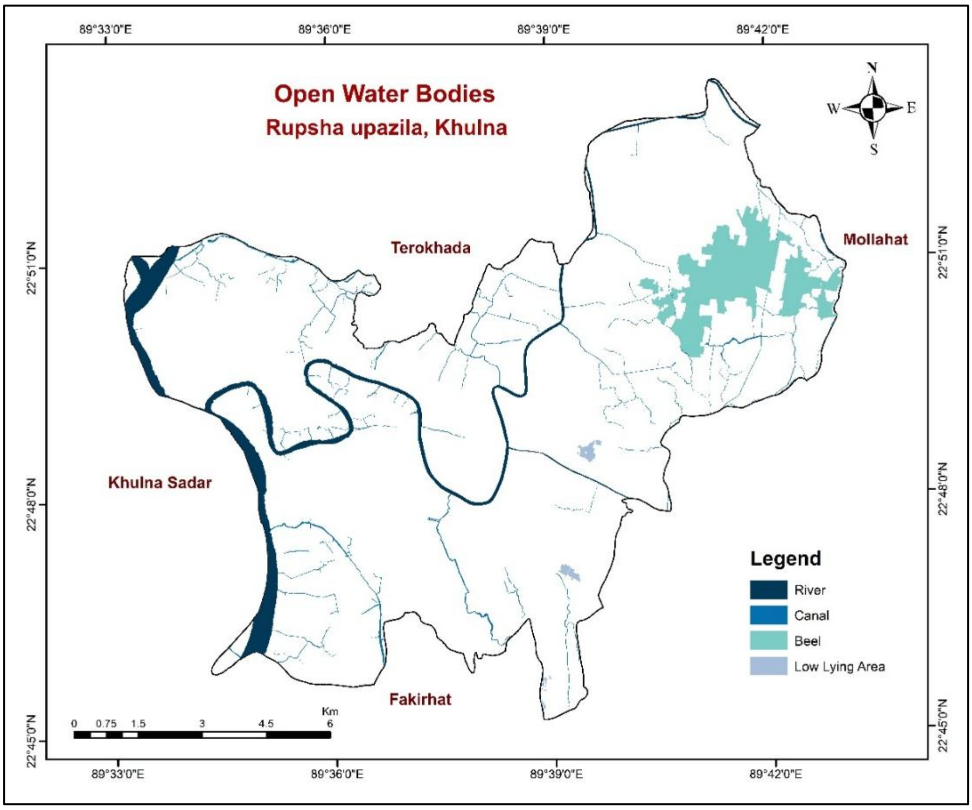


**Fig. 3.** Map of open water fisheries habitats in Rupsha Upazila

### 3.2 Closed water body

In this study, three types of closed water bodies were identified, including fish farms, ponds, and others. These closed water bodies cover a total of 4,198 hectares, accounting for 77.2% of the total fisheries habitats in the study area (Fig. 4). Among them, fish farms occupy the largest area (3,996 ha), contributing 95.2% of the total closed water fisheries habitats. A significant number of ponds were recorded, covering 83.96 hectares (2%). These ponds are mostly located near settlements, where extensive fish culture practices were observed. Another category of closed water bodies, referred to as "others" in this study, was found mostly along riverbanks and near brickfield areas, often connected to nearby rivers. This category covers 118 hectares, representing 2.8% of the closed water fisheries habitats. These water bodies are generally not used for fish production. Instead, they serve as a source of soil for brick manufacturing. Due to tidal action, sediment accumulates in these ponds, and the excavated soil is used as raw material for the brickfields, offering more economic value than aquaculture in those areas. Additionally, a pond-like reservoir was identified through ground truthing, which is actually a Khulna WASA reservoir tank used for water purification through different treatment processes. Both the brickfield-connected ponds and the WASA reservoir have been categorized as "others" fisheries resources during on-screen digitization. Both categories of water bodies (open and closed) constitute the total fisheries resources of Rupsha Upazila in Khulna District, covering an area of 5,438 hectares (Fig. 5). The fisheries resources database generated from this study is presented in Table 3.

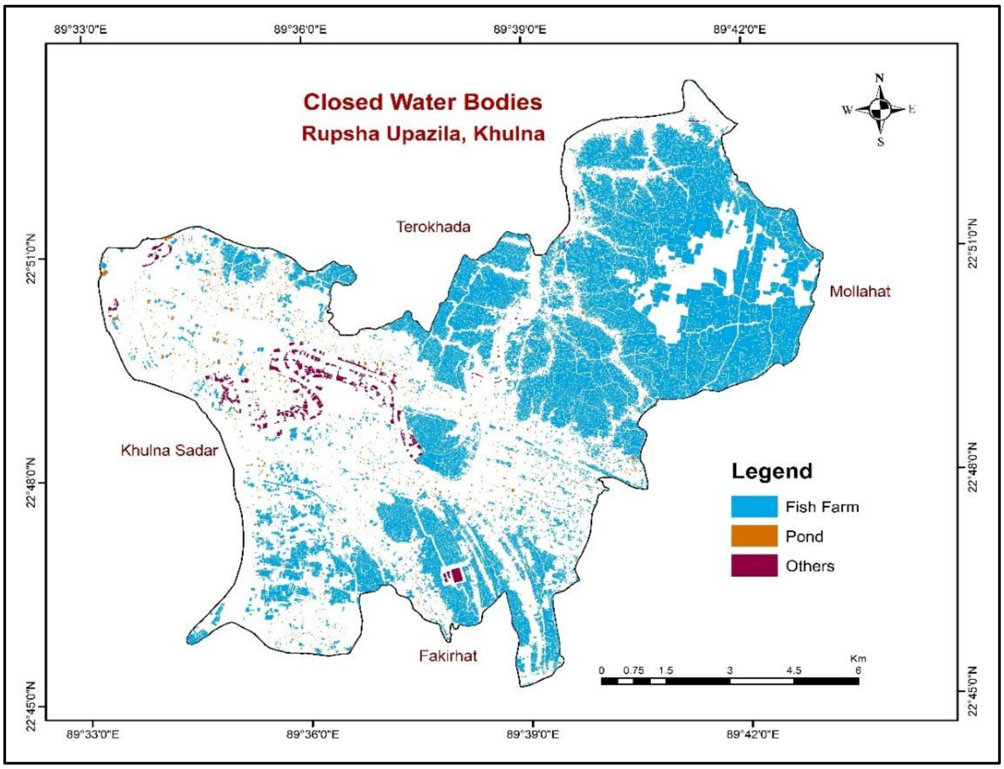


**Fig. 4.** Map of closed water fisheries habitats in Rupsha Upazila

### 3.3 Fisheries resource

A total of seven distinct types of waterbodies, covering an area of 5,438 hectares, were identified within the study area (Table 3). The northeastern region of Rupsha Upazila holds the majority of its fisheries resources, particularly in the form of fish farms and beel areas. Within the study area, the extent of closed water fisheries resources is more than three times greater than that of open water bodies (Fig. 5), which indicates substantial potential for the expansion and development of the aquaculture practices.

**Table 3.** Fisheries resource database obtained from the study

| Category of the waterbody | Name of the waterbody | Area (ha) |
|---|---|---|
| Open water body (1,240 ha) | River | 491 |
| | Canal | 160 |
| | Beel | 564 |
| | Low Lying Area | 24 |
| Closed water body (4,198 ha) | Fish Farm | 3,996 |
| | Pond | 84 |
| | Others | 118 |
| Total | | 5,438 |

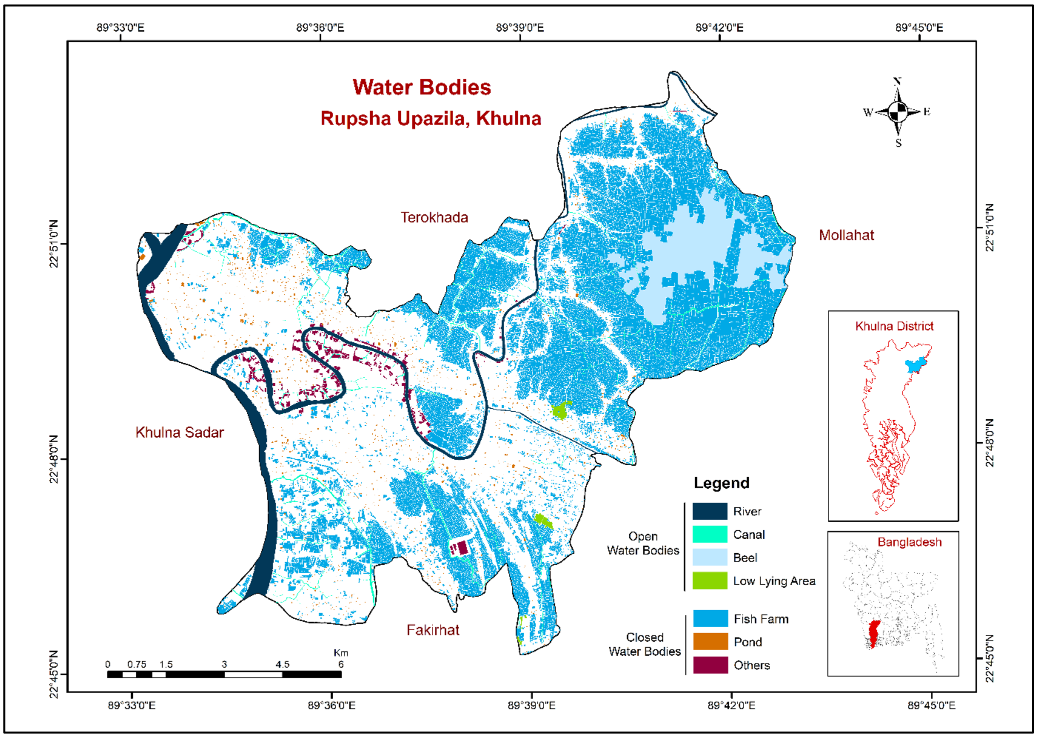


**Fig. 5.** Fisheries habitats map of Rupsha Upazila, Khulna

### 3.4 Accuracy assessment of digitized features

The overall classification accuracy achieved in this study was **95.80%**. Except for *fish farm* and *beel*, all other water body classes attained both producer's and user's accuracies of **100%**. For the *fish farm*, the producer's and user's accuracies were **96.50%** and **83.33%**, respectively, while for *beel*, the corresponding values were **97.47%** and **100%**. The overall reliability of the classification is further supported by a Kappa coefficient of **0.9154**, indicating a strong level of agreement (Table 4). Besides, repeated field investigations (Fig. 6) have been conducted along the study sites during the study period, which makes the study more meaningful, particularly the fisheries resource mapping.

**Table 4.** Accuracy of digitized features

| Classes | Producer Accuracy (Per Class) | User Accuracy (Per Class) |
|---|---|---|
| Canal | 100.00% | 100.00% |
| Fish Farm | 96.50% | 97.47% |
| Low Lying Area | 100.00% | 100.00% |
| Others | 100.00% | 100.00% |
| Pond | 100.00% | 100.00% |
| River | 100.00% | 100.00% |
| Beel | 83.33% | 100.00% |
| Overall Accuracy | 95.80% | |
| Kappa | 0.9154 | |


**Fig. 6**. Field photographs of different features have been collected by the authors during the field campaign on 25 May 2024

## 4. Discussion

The study identified seven different types of water bodies, with fish farms covering a substantial area. In this study, all types of water resources were identified, and a comprehensive digital database of water bodies was prepared. Using this approach, all boundaries were delineated precisely, resulting in higher accuracy compared to different studies. The use of very high-resolution satellite imagery in this study enabled the identification of all categories of water resources of the study sites. The similar study of Jakovljević et. al. (2019) mapped water bodies using different classification techniques and achieved a Kappa coefficient of 0.89, which is comparable to the result of the present study. The overall accuracy and kappa coefficient of the analyses are closely comparable to the other relevant studies (Ji et. al., 2022). Besides, the result is closely consistent with Tymków et. al. (2019), where the Kappa coefficient was 0.91 and water bodies were identified using several approaches, including supervised classification, thresholding, and image transformation. However, the findings of our study for accuracy and kappa coefficient show a moderate deviation (79%) from Hernandez-Suarez et al. (2022). Notably, all types of water body identification for fisheries resources using high-resolution satellite sensor data have not previously been considered for this specific area or elsewhere in Bangladesh.

The study used high-resolution WorldView-3 imagery (0.3 m spatial resolution) and subsequently validated it using updated Google Earth data. Due to the dynamic nature of land-use and land-cover patterns, particularly within beel and fish farm categories in Rupsha Upazila, the changes over three years interval resulted in minor discrepancies. The main constraints of on-screen digitization are that it is time-consuming and labor-intensive, making it difficult to produce frequently updated digital water body databases for the study area. Additionally, this method relies heavily on image quality and acquisition conditions. Another limitation is that wet soil may appear spectrally similar to water in optical imagery, which can create uncertainty in the accuracy of delineating water body boundaries.

Accurate information on the quantity, spatial extent, and distribution of water bodies is essential for effective planning and sustainable management of fisheries resources, which in Bangladesh are administered by the Department of Fisheries (DoF). The developed map and geospatial database provide a robust foundation for precise estimation of water body areas, which is critical for water-body-based planning, assessment of current production, and evaluation of fisheries resource productivity. Furthermore, accurate delineation of water body areas is required for optimal site selection for aquaculture development, demonstration and exhibition plots, open-water stocking programs, and the determination of appropriate culture tenure and technologies. The generated spatial dataset also enables reliable estimation of fisheries production in relation to water body size and spatial extent, thereby enhancing fisheries management efficiency at the regional scale. In addition, the map and database facilitate the identification and quantification of perennial water bodies during the dry season, which is crucial for establishing fish sanctuaries and for assessing sustainability and livelihood support for local fishing communities within the study area.

## 5. Conclusions

This study successfully identified and classified the various types of fisheries habitats in Rupsha Upazila of Khulna District, providing a baseline database that can significantly contribute to effective and sustainable fisheries management. Here, two broad categories of water bodies, namely open and closed water bodies, exist. Four types of open water bodies (rivers, canals, beels, and low-lying areas) and three types of closed water bodies (fish farms, ponds, and others) cover 1,240 hectares (22.8%) and 4,198 hectares (77.2%), respectively, of the total fisheries habitats found in the study area. The total extent of the waterbodies was 5438 ha, which accounted for 45.32% of the total area of the upazila. The findings highlight the considerable potential for improving fish production through informed planning and resource utilization. As no comprehensive database previously existed for this area, the generated dataset fills a critical gap in local fisheries resource management. To maintain accuracy and relevance, it is recommended that the database be updated at five-year intervals to reflect changes in resource distribution and usage.

## Acknowledgments

The authors would like to acknowledge Bangladesh Space Research and Remote Sensing Organization (SPARRSO) for providing funding for this research. The authors express their sincere appreciation to the Copernicus Open Access Hub for Sentinel 2 data that assisted satellite image interpretation. Special gratitude to Upazila Fisheries Office, Rupsha, Khulna, for supporting the research team during field data collection and validation.

## Data availability

The data will be made available upon request to the corresponding author.

## Conflict of interest

The authors declare that there is no conflict of interest regarding the publication of this paper.

## References

Bijeesh, T. V., Narasimhamurthy, K. N. (2020). Surface water detection and delineation using remote sensing images: a review of methods and algorithms, Sustainable Water Resources Management 6 (68). https://doi.org/10.1007/s40899-020-00425-4

Chen, Q. L., Zhang, Y.Z., Ekroos, A., Hallikainen, M. (2004). The role of remote sensing technology in the EU water framework directive (WFD). Environmental Science & Policy 7(4), 267–276. https://doi.org/10.1016/j.envsci.2004.05.002

Cohen, J. (1960). A coefficient of agreement for nominal scales. Educational and Psychological Measurement, 20(1), 37–46. https://doi.org/10.1177/001316446002000104

Deoli, V., Kumar, D., Kumar, M., Kuriqi, A., Elbeltagi, A. (2021). Water spread mapping of multiple lakes using remote sensing and satellite data, Arabian Journal of Geosciences 14, 2213. https://doi.org/10.1007/s12517-021-08597-9

Donchyts, G., Schellekens, J., Winsemius, H., Eisemann, E., & Giesen, N. van de. (2016). A 30 M resolution surface water mask including estimation of positional and thematic differences using Landsat 8, SRTM and Open Street Map: a case study in the Murray-Darling Basin, Australia. Remote Sensing 8(5), 386. https://doi.org/10.3390/rs8050386

Feyisa, G. L., Meilby, H., Fensholt, R., Proud, S. R. (2013). Automated water extraction index: a new technique for surface water mapping using Landsat imagery. Remote Sensing of Environment 140, 23-35. https://doi.org/10.1016/j.rse.2013.08.029

Hernandez-Suarez, J.S., Nejadhashemi, P.A., Ferriby, H., Moore, J.N., Belton, B., Haque, M.M. (2022). Performance of Sentinel-1 and 2 imagery in detecting aquaculture waterbodies in Bangladesh. Environmental Modelling & Software 157, 105534. https://doi.org/10.1016/j.envsoft.2022.105534

Jakovljević, G., Govedarica, M., Álvarez-Taboada, F. (2019). Waterbody mapping: a comparison of remotely sensed and GIS open data sources. International Journal of Remote Sensing 40(8), 2936-2964. https://doi.org/10.1080/01431161.2018.1538584

Ji, Z., Zhu, Y., Pan, Y., Zhu, X., Zheng, X. (2022). Large-scale extraction and mapping of small surface water bodies based on very high-spatial-resolution satellite images: a case study in Beijing, China. Water 14 (18), 2889. https://doi.org/10.3390/w14182889

Jiang, H., Feng, M., Zhu, Y., Lu, N., Huang, J., Xiao, T. (2014). An automated method for extracting rivers and lakes from Landsat imagery. Remote Sensing 6 (6), 5067-5089. https://doi.org/10.3390/rs6065067

Li, L., Xia, H., Li, Z., Zhang, Z. (2015). Temporal-spatial evolution analysis of lake size-distribution in the middle and lower Yangtze River basin using Landsat imagery data. Remote Sensing 7(8):10364-10384. https://doi.org/10.3390/rs70810364

Lu, S., Wu, B., Yan, N., Wang, H. (2011). Water body mapping method with HJ-1A/B satellite imagery. International Journal of Applied Earth Observation and Geoinformatics 13(3), 428–434. https://doi.org/10.1016/j.jag.2010.09.006

Masser, I. (2001). Managing our urban future: the role of remote sensing and geographic information systems. Habitat International 25(4):503–512. https://doi.org/10.1016/S0197-3975(01)00021-2

Mcfeeters, S. K. (1996). The use of the Normalized Difference Water Index (NDWI) in the delineation of open water features, International Journal of Remote Sensing 17(7), 1425–1432. https://doi.org/10.1080/01431169608948714

Ozesmi, S.L., Bauer, M. E. (2002). Satellite remote sensing of wetlands. Wetlands Ecology and Management 10, 381–402. https://doi.org/10.1023/A:1020908432489

Peng, J., Pan, Y., Liu, Y., Zhao, H., Wang, Y. (2018). Linking ecological degradation risk to identify ecological security patterns in a rapidly urbanizing landscape. Habitat International 71,110–124. https://doi.org/10.1016/j.habitatint.2017.11.010

Subramaniam, S., Babu, A.V. S., Roy. P. S. (2011). Automated water spread mapping using ResourceSat-1 AWiFS Data for water bodies information system. IEEE Journal of Selected Topics in Applied Earth Observations and Remote Sensing 4(1), 205–215. DOI:10.1109/JSTARS.2010.2085032

Tymków, P., Jóźków, G., Walicka, A., Karpina, M., Borkowski, A. (2019). Identification of Water body extent based on remote sensing data collected with unmanned aerial vehicle. Water 11(2), 338. https://doi.org/10.3390/w11020338

Xu, H. (2006). Modification of normalised difference water index (NDWI) to enhance open water features in remotely sensed imagery, International Journal of Remote Sensing 27(14), 3025–3033. https://doi.org/10.1080/01431160600589179

# Assessing the Compatibility of Machine Learning Tools for Mapping Impervious Surfaces of Urban Areas: A Geospatial Analysis of the Dhaka Metropolitan Area (DMPA)

Md. Sazedur Rahman*[a], Mahisha Islam Kuasha[a], Amir Fosial[b], Md. Abdul Kadir[c] and Shoeb Ahmad Tanim[d]

[a]*Department of Water Resources Engineering, Bangladesh University of Engineering and Technology, Bangladesh.*

[b]*Department of Civil Engineering, International Islamic University Chittagong, Bangladesh.*

[c]*Department of Mathematics, University of Houston, Texas, USA.*

[d]*Department of Civil Engineering, International Islamic University Chittagong, Bangladesh.*

**Corresponding author:[1716007@wre.buet.ac.bd](mailto:1716007@wre.buet.ac.bd) (Md. Sazedur Rahman)*

**Article info**

***Keywords:***
*Impervious surfaces,*
*Urban growth,*
*GIS-RS,*
*Dhaka,*
*Landsat*

***Article History:***
Received-25 Nov 2025
Revised-15 Jan 2026
Accepted-01 Feb 2026
Published-31 March 2026

**DOI:**
[https://doi.org/10.66268/jrse.2026.05.917341](https://doi.org/10.66268/jrse.2026.05.917341)

**ABSTRACT**

Rapid and unplanned urbanization in the Dhaka city area has significantly accelerated the expansion of impervious surfaces, altering the hydrological balance, intensifying surface runoff, and increasing environmental vulnerability. Therefore, the accurate mapping of impervious surfaces is crucial for evaluating urban growth patterns and designing sustainable, climate-resilient infrastructure. Hence, this study assesses the current impervious-surface landscape and evaluates the performance compatibility of manual digitization and machine-learning-based supervised classification techniques for mapping impervious surfaces across the Dhaka Metropolitan Area (DMPA) using geospatial techniques. Here, the manual digitization estimated the total impervious coverage at 138.08 km² (46.23%), while the machine learning (ML)-based supervised classification produced 155.68 km² (52.12%), revealing a 5.89% overestimation, primarily due to mixed-pixel effects at a 30 m spatial resolution. The classification achieved an overall accuracy of 88.4% and a Kappa coefficient (κ) of 0.84, indicating strong agreement with reference data. The results depict that the most urbanized areas, such as Lalbagh, Sutrapur, Kotwali, and Dhanmondi, exhibited the highest imperviousness. In contrast, planned or peripheral areas, such as Gulshan, Uttara, and Pallabi, retained larger pervious zones due to structured development and better land-use planning. The impervious coverage of Dhaka city far exceeds the ecological sustainability threshold (10%), signifying a critical hydrological imbalance and increased heat risks. The findings affirm that the MLC method is a reliable, scalable tool for urban surface analysis when complemented with high-resolution validation data. This study highlights the urgent need for prioritizing the restoration of green–blue infrastructure, the expansion of pervious surfaces, and the integration of a remote-sensing-based monitoring system to mitigate the escalating environmental pressures of rapid urban growth.

## 1. Introduction

Urbanization represents one of the most profound anthropogenic transformations of the Earth's surface, reshaping land cover, hydrological processes, and ecosystem dynamics at multiple spatial scales (Soufiane et al., 2025; Sonet et al., 2025). Among the various indicators of urban expansion, impervious surfaces, including roads, buildings, pavements, and other sealed structures, serve as a key proxy for understanding the extent and intensity of urban growth (Li et al., 2023). These surfaces inhibit natural infiltration, increase surface runoff, reduce evapotranspiration, and alter both local and regional hydrological balances (Xu et al., 2025; Soufiane et al., 2025). Consequently, mapping impervious surfaces accurately is fundamental for assessing urban hydrology, flood susceptibility, and land-surface thermal behavior, as well as for designing climate-resilient urban infrastructure (Chen et al., 2020; Su et al., 2022). The ecological consequences of increasing imperviousness are well established. Numerous studies have demonstrated that when impervious cover exceeds approximately 10% of a watershed, significant degradation in stream health, water quality, and habitat diversity occurs (Sohn et al., 2020; Zhang et al., 2022). Beyond the 30% threshold, urban watersheds typically experience chronic flooding, thermal stress, and groundwater depletion (Sun et al., 2019; Faisal et al., 2021). In this context, the quantitative and spatial assessment of impervious surfaces provides a diagnostic basis for sustainable drainage planning and for setting local ecological benchmarks (Rentachintala et al., 2022; Sonet et al., 2025).

Over the past two decades, remote sensing has emerged as an indispensable tool for detecting and quantifying impervious surfaces, benefiting from advances in spectral resolution, data accessibility, and computational algorithms (Wu & Pan, 2023; Mondal et al., 2025). Early studies primarily relied on pixel-based classification using medium-resolution sensors such as Landsat MSS, TM, and ETM+ (Stern et al., 2022), while contemporary approaches increasingly employ machine-learning classifiers, object-oriented analysis, and data fusion techniques to enhance classification accuracy and spatial precision (Shao et al., 2022). Among these, the Maximum Likelihood Classifier (MLC) remains a widely used and computationally efficient algorithm for land-cover discrimination, particularly in resource-limited contexts (Li et al., 2024). Although the MLC performance can be constrained by mixed pixels and class overlaps in heterogeneous urban areas, its integration with manual reference data often produces reliable results for metropolitan-scale analysis (Li et al., 2023).

Despite growing global research, South Asian megacities such as Dhaka remain underrepresented in impervious surface studies. Dhaka, one of the world's fastest-growing and most densely populated cities, has undergone rapid urban expansion over the past four decades. The city's built-up area increased from only 11.6 $km^2$ in 1989 to over 118 $km^2$ in 2014, with projections surpassing 170 $km^2$ by 2030 (Faridatul et al., 2019; Kulsum and Moniruzzaman, 2022; Ahmad et al., 2024). This transformation, largely unplanned, has replaced wetlands, floodplains, and agricultural land with concrete-dominated surfaces, leading to severe drainage congestion, elevated surface temperatures, and frequent urban flooding (Faisal et al., 2021). Several studies have been systematically conducted on urban growth and its impact using high-resolution imagery with machine-learning classification from medium-resolution satellite data to evaluate the accuracy, limitations, and spatial implications of Dhaka's highly heterogeneous landscape (Abbasi et al., 2022; Bashar & Uddin, 2025). However, none of them compared those machine learning methods based on satellite images with ground truth, i.e., manually collected real-world data.

Addressing these gaps, the present study compares manual digitization and MLC-based supervised classification using Landsat 8 Operational Land Imager (OLI) imagery to map impervious surfaces across the Dhaka Metropolitan Area (DMPA). By integrating manual high-resolution interpretation with machine-learning-based classification, this research offers a validated methodological framework for urban surface mapping in complex megacities. The findings aim to contribute to data-driven hydrological modeling, urban heat mitigation, and green–blue infrastructure planning in Dhaka and other urban regions in South Asia. The objectives of this study are to quantify the extent of impervious surfaces across the city areas, to evaluate the spatial distribution of imperviousness against ecological thresholds, and to assess the accuracy of the MLC approach relative to manually referenced real data.

## 2. Materials and methods

### 2.1 Study area

The study focuses on the DMPA, which represents the core urban area of Dhaka, the capital and economic center of Bangladesh. Geographically located between 23°40′N–23°54′N and 90°20′E–90°32′E, the DMPA covers approximately 305.47 km² and encompasses 15 administrative thanas, including Ramna, Motijheel, Sutrapur, Sabujbagh, Lalbagh, Kotwali, Uttara, Demra, Cantonment, Gulshan, Tejgaon, Mohammadpur, Dhanmondi, Pallabi, and Mirpur (Fig. 1). The region is bounded by the Turag River to the west, the Balu River to the east, and the Buriganga River to the south, forming a low-lying alluvial floodplain within the lower deltaic basin of the Ganges–Brahmaputra–Meghna system. Dhaka's elevation ranges between 1.5 m and 13 m above mean sea level, making it highly susceptible to monsoon-induced flooding and drainage congestion. Its subtropical monsoon climate is characterized by an average annual rainfall of 2,000 mm, with more than 80% occurring between May and September. Over the past four decades, Dhaka has experienced rapid and unplanned land conversion from agricultural and wetland ecosystems to impervious built-up structures, driven by population growth exceeding 21 million residents (BBS, 2022). The expansion of impervious surfaces, roads, buildings, and paved courtyards has drastically modified the city's natural drainage, elevated urban heat, and reduced green space coverage (Moniruzzaman et al., 2020; Uddin et al., 2022;). These conditions make Dhaka an ideal case for evaluating the effectiveness of remote-sensing techniques in mapping urban impervious surfaces and understanding their spatial variability under rapid megacity expansion (Faisal et al., 2021; Mondal et al., 2025).

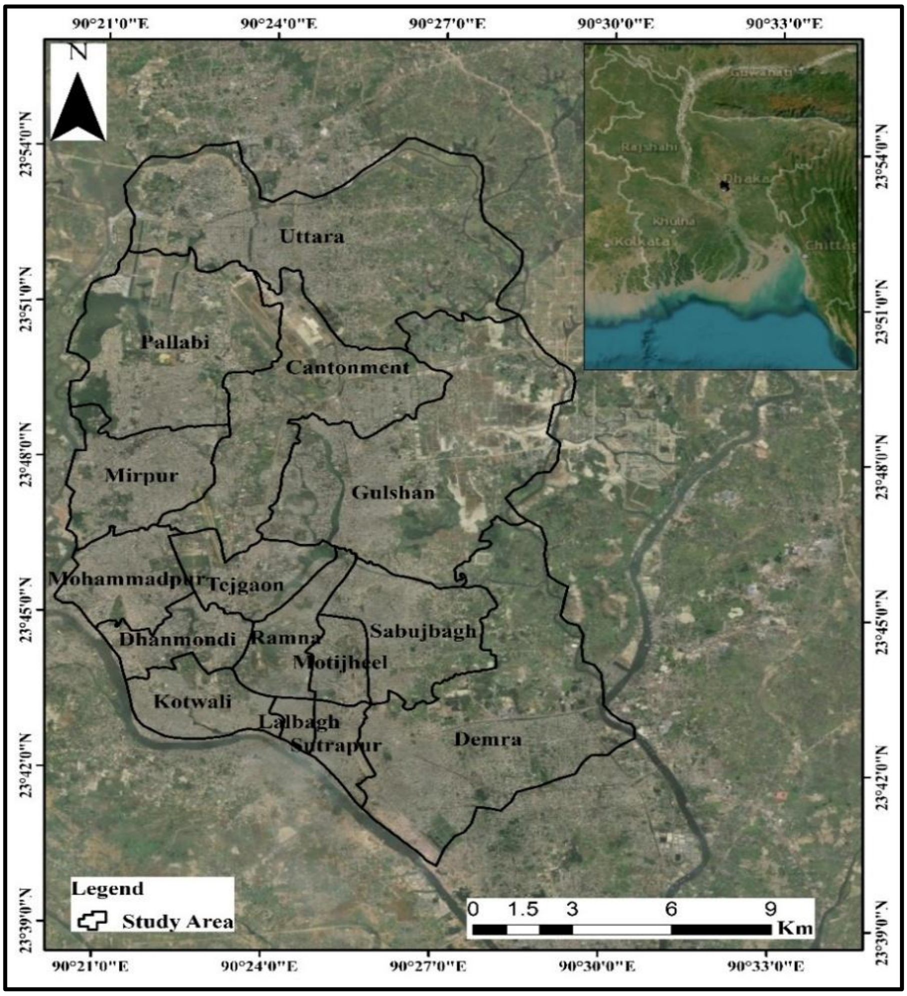


**Fig. 1.** Map of the study area showing the administrative units of the DMA

## 2.2 Data collection

To evaluate impervious surface distribution, this study integrates both high-resolution optical imagery and moderate-resolution multispectral satellite data, complemented by spatial reference datasets for validation and analysis (Table 1). Here, the high-resolution image from Google Earth Pro, collected between May and June 2025 (Table 1), was used to manually digitize impervious features, including buildings, roads, paved areas, and other constructed surfaces. These images provided sub-meter spatial detail and served as the reference dataset for validation and accuracy assessment. The digitized polygons were exported in KMZ format and converted to shp files in ArcGIS 10.8.2 for spatial quantification and comparison. Also, the multispectral data from the Landsat 8 OLI (Level-1) were acquired for the same period via the United States Geological Survey (USGS) EarthExplorer portal (https://earthexplorer.usgs.gov/). The imagery provides 11 spectral bands with a spatial resolution of 30 m for our research purposes, where bands 2–7 were collected with <10% cloud coverage. Additional spatial layers, including administrative boundaries, water bodies, and transportation networks, were obtained from the Bangladesh Bureau of Statistics (BBS) and the Survey of Bangladesh (SoB) as mentioned in Table 1. These datasets provided essential contextual information for enhancing the accuracy of thana-level zonation and mapping.

**Table 1**. Summary of datasets used in this study

| Data Type | Source | Resolution | Acquisition | Purpose |
|---|---|---|---|---|
| Google Earth Pro imagery | Google Earth Pro | < 1 m | May–June 2025 | Manual digitization, accuracy validation |
| Landsat 8 OLI | USGS Earth Explorer | 30 m (Bands 2–7) | 29/06/2025 | Supervised classification of impervious surfaces |
| Administrative boundary | Survey of Bangladesh (SoB) | Vector | 2025 | Thana boundary demarcation |
| Base map/water bodies | Bangladesh Bureau of Statistics (BBS) | Vector | 2025 | Spatial reference and visualization |

## 3. Methodology

The methodological framework of this study integrates manual digitization and machine-learning-based supervised classification to map and assess impervious surfaces within the DMPA. The process involves three major stages: (1) manual delineation of impervious features, (2) satellite image classification, and (3) accuracy assessment and validation (Fig. 2).

### 3.1 Manual delineation of impervious surfaces

High-resolution optical imagery from Google Earth Pro (May–June 2025) was harmonized under a uniform coordinate system and, before classification at a scale of 1:300 for dense areas and 1:500 for the rest of the DMPA boundary. The integration of multi-scale datasets ensured both fine-scale feature precision (via manual digitization) and the establishment of a comprehensive database for impervious surface analysis. The DMPA was subdivided into 15 administrative thanas to ensure spatial detail and comparability. Using polygon tools in Google Earth, impervious features such as rooftops, roads, runways, and paved courtyards were digitized at a 1:500 scale to minimize distortion, as well as the vegetation and water bodies. Each polygon was verified by three trained interpreters to reduce subjectivity and ensure consistency across datasets. The digitized features were exported as KMZ in four files, building and roads as developed area, bare land, vegetation, and waterbody, then converted to shapefiles in ArcGIS 10.8.2 (Fig. 2), and used to calculate the areal extent of impervious surfaces per thana. This manually generated dataset provided the benchmark for evaluating classification results derived from satellite imagery. Although labor-intensive, manual mapping remains one of the most precise techniques for reference data generation in heterogeneous urban environments.

### 3.2 Satellite image preprocessing and supervised classification

The Landsat 8 OLI Level-1 provides geometrically corrected to the World Geodetic System (WGS 84, UTM Zone 46N) as shown in Table 1, but atmospheric correction is still required. Several steps are followed for this in ArcGIS for each band (2-7) separately (Van Nguyen et al., 2025). Firstly, during data collection, all the metadata were collected for each image from bands 2 to 7 with less than 10% cloud cover. Then, cloud and Shadow pixels masking was done by Google Earth Engine using the QA_PIXEL band tool on the raster data and then imported to ArcGIS to remove contaminated pixels (Zhang et al., 2022). Next on ArcGIS, DNs (Digital Numbers) are converted to TOA (Top-of-Atmosphere) radiance using the radiometric rescaling coefficients from the downloaded metadata and the raster calculator. TOA radiance is further converted to TOA reflectance by using a raster calculator to normalize the data with respect to solar irradiance and acquisition geometry. Finally, atmospheric correction was employed to transform TOA reflectance into surface reflectance, applying Dark Object Subtraction (DOS) with the help of raster calculator that removes haze and atmospheric effects (Yan & Roy, 2025).

Following atmospheric correction, the surface reflectance images of Landsat 8 OLI (Bands 2–7) were used for supervised classification in ArcGIS to produce a thematic land use/land cover (LULC) map of the DMPA. In which representative samples are manually selected for each LULC class (built-up areas, vegetation, water bodies, and bare land) based on field knowledge from high-resolution imagery and Google Earth Engine, and the bands (2-7) were stacked to form a multiband composite. Then Maximum Likelihood Classification (MLC) algorithm was applied for supervised classification, which assigned each pixel to the class with the highest probability according to the multivariate normal distribution of spectral signatures (Hu et al., 2024). After the classification, a thematic LULC map was generated for each class, symbolizing them distinctly for visual interpretation. Subsequently, area calculation was performed by converting classified pixels into vector polygons and computing the area for each LULC class using ArcGIS's geometry calculation tools, allowing quantitative assessment of land cover distribution across the DMPA. This workflow ensures that the final map and area statistics accurately reflect spatial patterns and the extent of urban, vegetated, water, and bare land features.

### 3.3 Accuracy assessment and validation

The accuracy assessment and validation procedures were undertaken to ensure the reliability and robustness of the supervised classification results. The process involved generating validation samples, verifying reference data, constructing a confusion matrix, and calculating standard accuracy indices. A total of 750 stratified random validation points were created across the classified image using ArcGIS 10.8.2 for each class, employing a stratified random sampling technique to guarantee that all major land-cover categories, including impervious surfaces, vegetation, bare soil, and water, were proportionally represented according to their spatial extent within the classified output. This method was selected to maintain statistical balance among classes and to minimize potential bias toward dominant surface types. The validation points were spatially distributed throughout the DMPA to capture the inherent heterogeneity of its urban landscape. Each validation point was independently verified using high-resolution Google Earth Pro imagery (May–June 2025) and the manually digitized reference dataset, ensuring that the reference data remained independent of the training samples used in the classification process. For each sampled location, the true land-cover type was assigned through visual interpretation of the reference imagery, identifying the predominant surface feature corresponding to that point. This verification process provided an accurate and reliable reference database for subsequent validation.

Following the establishment of the reference dataset, a confusion matrix (or error matrix) was generated by cross-tabulating the classified image outputs with the verified reference data. The matrix was produced using the Error Matrix and Accuracy Assessment tools in ArcGIS 10.8.2, which automatically compared predicted class labels with actual land-cover categories for each validation point. The confusion matrix served as the basis for computing statistical accuracy measures following Jombo and Adelabu (2023), including Producer's Accuracy (PA), User's Accuracy (UA), Overall Accuracy (OA), and the Kappa coefficient (κ). The OA quantified the ratio of correctly classified samples to the total number of validation points, while PA and UA provided measures of omission and commission errors for each class, respectively. The κ statistic was derived from the confusion matrix to evaluate the degree of agreement between the classified and reference datasets beyond random chance (Kocaman & Ağaçcıoğlu, 2024), where κ values greater than 0.80 denote near-perfect agreement (Li et al., 2024). This systematic approach ensured that the classification accuracy was evaluated using statistically representative and spatially distributed validation samples. By integrating high-resolution reference imagery, independent verification, and matrix-based statistical evaluation, the adopted procedure provided a rigorous, reproducible, and internationally recognized framework for assessing the performance of remotely sensed classifications (Su et al., 2022). The methodology aligns with established accuracy assessment standards and remains consistent with previous urban land-cover classification studies (Li et al., 2023; Sonet et al., 2025).

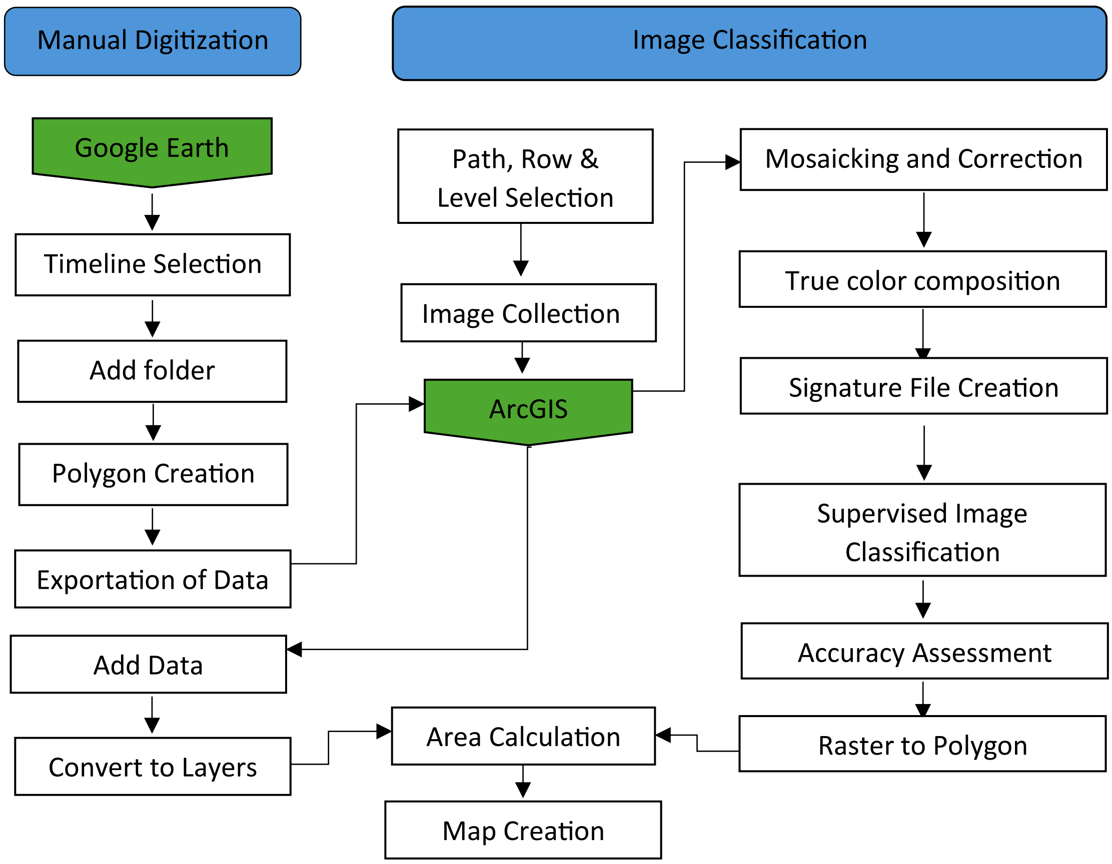


**Fig. 2.** A complete methodological workflow of manual digitization and image classification

# 4. Results

## 4.1 Spatial distribution of imperviousness

The spatial analysis of impervious surface coverage across the fifteen thanas of the DMPA demonstrates a clear core–periphery gradient, reflecting the contrasting morphology between the densely built historical core and the relatively open, planned peripheries. The results from both manual digitization and image classification show similar spatial trends, with variation in magnitude due to the differences in spatial resolution and feature generalization (Fig. 3 and Fig. 4).

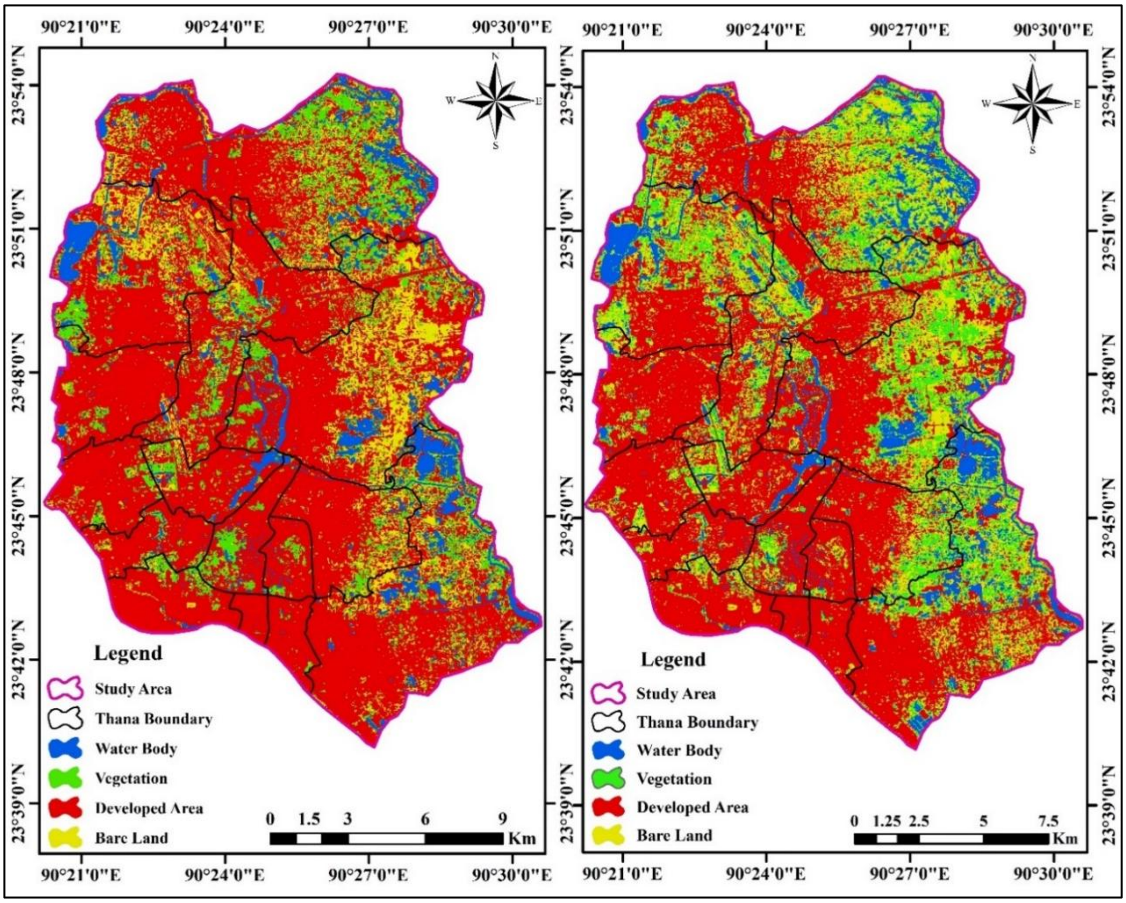


**Fig. 3.** LULC map derived from MLC (left) and manual digitization (right)

The central and southern thanas, Lalbagh (62.33% manual; 70.52% classified), Sutrapur (61.41%; 69.40%), Kotwali (59.50%; 67.14%), and Dhanmondi (59.45%; 67.08%) exhibit the highest impervious coverage within the DMPA (Fig. 3, Fig. 4, Fig. 5, and Fig. 6). These areas represent Dhaka's historical urban cores, characterized by unplanned and vertical growth, limited open space as bare land, and almost no vegetation or water bodies, and dense building footprints. Their impervious extent far exceeds the ecological sustainability threshold of 10%, indicating severely reduced infiltration and increased flood susceptibility (Li et al., 2023).

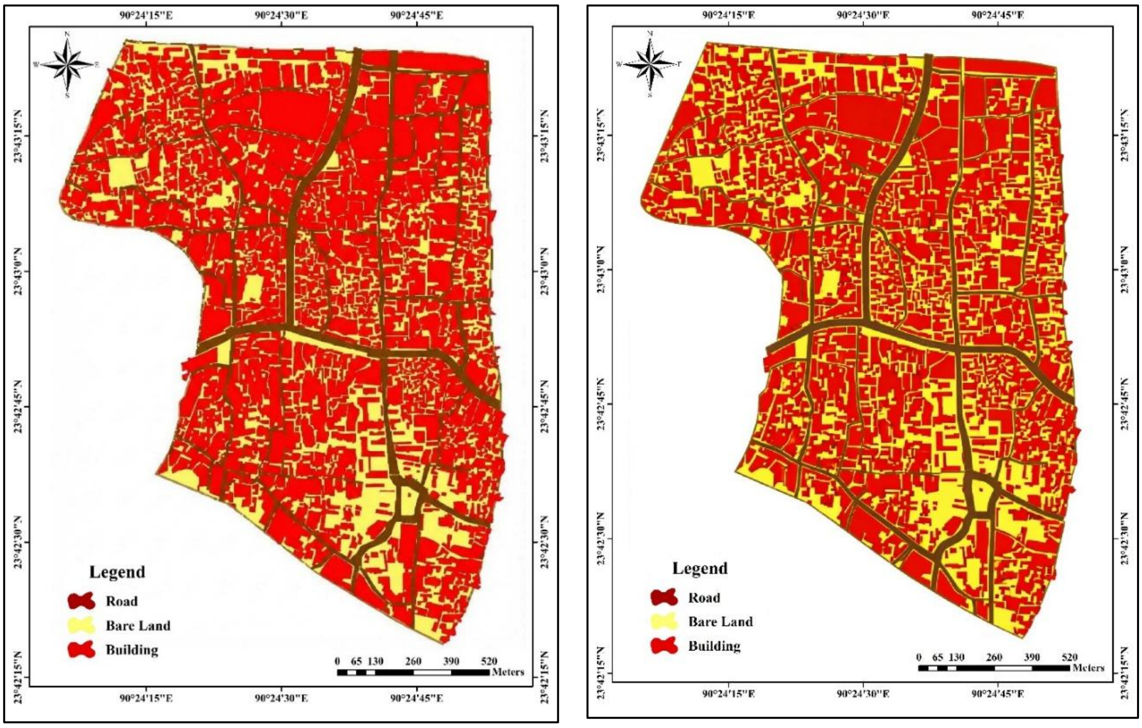


**Fig. 4.** Impervious map of MLC (left) and Manual Digitization (right) for Lalbagh Thana

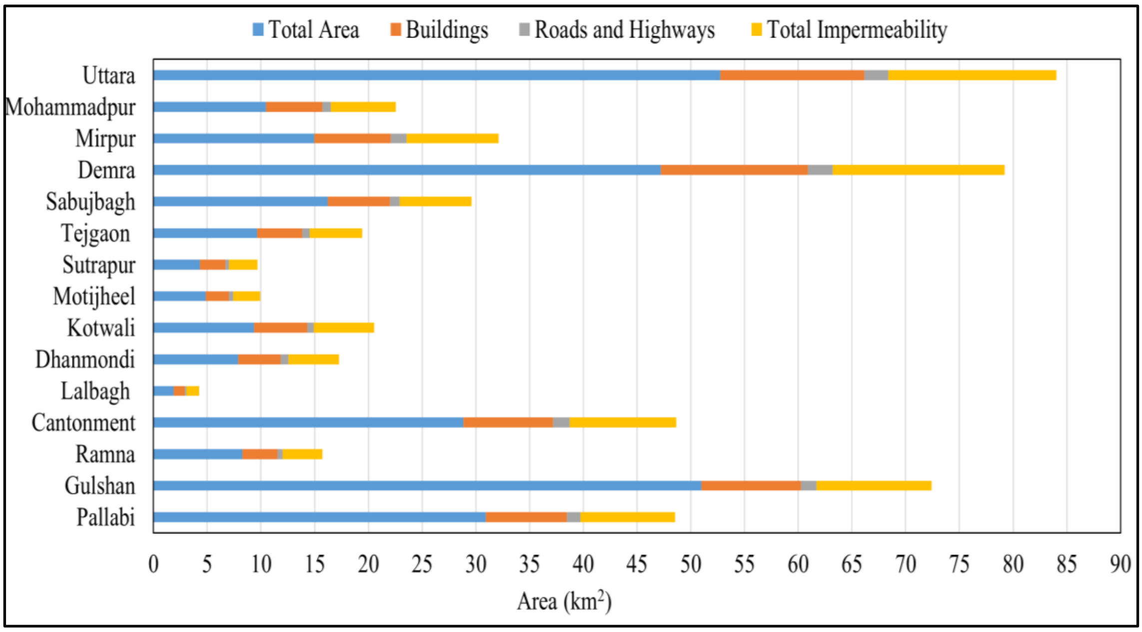


**Fig. 5.** Impervious area from manual digitization in DMPA

Moderately urbanized thanas such as Motijheel (51.78%; 58.13%), Tejgaon (50.81%; 57.02%), Mohammadpur (57.62%; 64.92%), and Mirpur (57.18%; 64.40%) show high but relatively balanced imperviousness. These regions consist of mixed residential, commercial, and industrial land uses, where semi-pervious zones such as courtyards, institutional campuses, and roadside vegetation still exist but are rapidly declining due to infill development and infrastructure. Intermediate and transition zones, including Ramna (44.84%; 50.23%), Sabujbagh (41.22%; 46.17%), Cantonment (34.31%; 38.56%), and Demra (33.88%; 38.09%), show moderate imperviousness, reflecting a blend of residential, governmental, and vegetated land cover. Although these areas retain some open land and tree cover, progressive urban infilling and transportation expansion threaten their permeability.

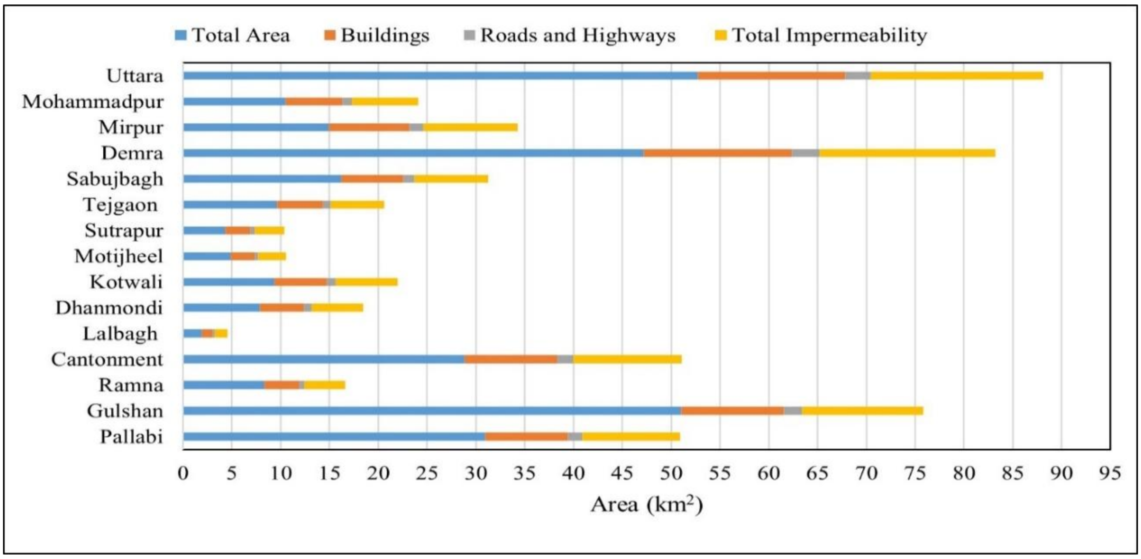


**Fig. 6.** Impervious area from supervised classification in DMPA

In contrast, northern and planned thanas such as Pallabi (28.45%; 32.23%), Uttara (29.66%; 33.53%), and Gulshan (21.00%; 24.36%) exhibit the lowest imperviousness within the metropolitan area. Their planned urban designs, larger residential plots, and maintained green spaces contribute to higher infiltration potential and more efficient stormwater management compared to the congested central zones. Spatial visualization of the classified imagery further reveals that the impervious intensity radiates outward from the historic southern cores, Lalbagh (Fig. 4), Kotwali, and Sutrapur toward newer developments in Tejgaon, Mirpur, and Uttara. This pattern corresponds with Dhaka's chronological growth trajectory, where unplanned densification has gradually expanded northward. Overall, the citywide imperviousness exceeding 50% according to image classification results indicates a critical level of hydrological and ecological stress. The spatial differentiation across thanas underscores the urgent need for zonal planning interventions. Urban authorities should prioritize the restoration of green-blue infrastructure, the adoption of permeable pavement, and the enforcement of open space retention policies, particularly in the most impervious central zones, to mitigate runoff and urban heat effects.

### 4.2 Comparison of impervious surface estimation

The comparative analysis of impervious surface mapping using manual digitization and the MLC revealed consistent but quantitatively distinct results. Within the DMPA, manual digitization of high-resolution Google Earth Pro imagery estimated a total impervious area of 138.08 km², representing 46.23% of the total study area. In contrast, the MLC-based supervised classification using Landsat 8 OLI imagery estimated 155.68 km² (52.12%) of impervious cover, corresponding to a 5.89% overestimation relative to the manually delineated reference. This discrepancy is primarily attributed to the mixed-pixel effect associated with the 30 m spatial resolution of Landsat imagery, where sub-pixel heterogeneity, particularly in compact urban areas, tends to generalize small, vegetated gaps or semi-pervious materials as impervious surfaces (Li et al., 2024; Sonet et al., 2025). Nevertheless, both methods show strong correspondence in the spatial distribution of built-up areas, indicating that MLC effectively captures the dominant impervious patterns within Dhaka's heterogeneous landscape. When compared to other major South and Southeast Asian cities, Dhaka exhibits similar or slightly higher imperviousness. Recent studies reported impervious surface coverage of 47–50% in Kolkata, 45–53% in Jakarta, and 44–49% in Bangkok (Li et al., 2023; Wu & Pan, 2023). These values confirm a regional trend of extensive surface sealing across rapidly urbanizing tropical megacities, driven by unplanned expansion, population pressure, and inadequate green infrastructure planning. Dhaka's impervious coverage surpasses even the upper range observed in these cities, positioning it among the most heavily sealed urban environments in the region.

The observed correlation between manually and automatically derived estimates underscores the operational reliability of the MLC for regional-scale impervious mapping, especially when validated with high-resolution data. The findings align with previous research in comparable metropolitan contexts, reaffirming that the MLC approach can serve as a dependable tool for tracking urban surface dynamics where computational efficiency and reproducibility are critical (Li et al., 2023; Wu & Pan, 2023).

### 4.3 Accuracy assessment and classification reliability

Accuracy assessment confirms the robustness of the MLC-based classification. The confusion matrix derived from 750 stratified random validation points produced an overall accuracy of 88.4% and a Kappa coefficient (κ) of 0.84 (Table 2), denoting almost perfect agreement between classified and reference datasets (Kocaman & Ağaçcıoğlu, 2024). Class-wise evaluation indicated that impervious surfaces achieved Producer's Accuracy (PA) of 89.7% and User's Accuracy (UA) of 86.2%, reflecting strong model sensitivity and reliability in detecting built-up features. Misclassification primarily occurred in transitional zones such as vegetated courtyards or mixed asphalt bare soil areas, where spectral similarity caused confusion between previous and impervious categories (Jombo & Adelabu, 2023). Overall, the high accuracy and spatial consistency between manual and MLC-derived outputs validate the methodology's applicability for continuous monitoring of urban surface dynamics in Dhaka. The framework offers a reproducible approach for integrating multi-resolution datasets to support climate-resilient urban planning and hydrological modeling.

**Table 2.** Accuracy assessment of MLC classification

| Metric | Impervious Surfaces | Vegetation | Bare Soil | Water | Overall |
|---|---|---|---|---|---|
| Producer's Accuracy (%) | 89.7 | 85.2 | 87.1 | 90.6 | — |
| User's Accuracy (%) | 86.2 | 88.9 | 85.4 | 92 | — |
| Overall Accuracy (%) | — | — | — | — | 88.4 |
| Kappa Coefficient (κ) | — | — | — | — | 0.84 |

## 5. Discussion

This study highlights the alarming extent of surface sealing in Dhaka, where impervious surface coverage reached 46.23% through manual delineation and 52.12% using the MLC. These values far exceed the global ecological threshold of 10% and the severe degradation limit of 30% (Li et al., 2023), signifying advanced urban surface sealing and substantial hydrological imbalance. The spatial heterogeneity observed among the 15 thanas reveals a distinct urban core–periphery gradient: Lalbagh, Sutrapur, Kotwali, and Dhanmondi represent the most compact and impervious sectors due to unplanned high-density development, while Gulshan, Uttara, and Pallabi maintain relatively lower imperviousness owing to planned layouts and greater vegetated coverage. The comparative analysis confirms that manual digitization provides high spatial precision and visual interpretability, serving as a benchmark for validation. In contrast, the MLC-based classification achieves efficient and replicable mapping over large spatial and temporal scales. Although the 30 m Landsat resolution introduced a 5.89% overestimation due to mixed-pixel effects, the achieved accuracy (88.4%) and Kappa coefficient (0.84) validate the reliability of the approach. Similar accuracy benchmarks were reported by Wu and Pan (2023) and Sun et al. (2019), underscoring the robustness of supervised classification for regional-scale urban studies.

In comparison to other South and Southeast Asian megacities such as Kolkata (47–50%), Jakarta (45–53%), and Bangkok (44–49%) (Li et al., 2023), Dhaka now ranks among the most impervious urban environments. The hydrological consequences include diminished infiltration, increased surface runoff, frequent pluvial flooding, and reduced groundwater recharge (Xu et al., 2025). Furthermore, vegetation loss and heat absorption by built-up structures intensify urban heat island effects, as evidenced in related studies (Faisal et al., 2021). The findings call for an integrated urban management framework that continuously monitors imperviousness using remote sensing and geospatial tools to guide sustainable land-use planning and flood mitigation strategies. Future research should focus on integrating high-resolution satellite imagery and advanced ensemble classifiers that can enhance the detection of precision. Incorporating temporal data and field validation would also enable dynamic monitoring of impervious surface growth and its hydrological consequences.

## 6. Conclusions

The study provides a comprehensive assessment of manual and machine-learning approaches for impervious surface mapping in the capital city of Bangladesh, Dhaka. Both methods confirm extensive urban sealing, indicating critical ecological stress and hydrological imbalance. The MLC method achieved strong accuracy metrics (OA=88.4%, $\kappa$=0.84), validating its applicability for urban-scale classification, while the 5.89% overestimation relative to manual mapping underscores the limitations of medium-resolution imagery. Dhaka's impervious coverage now surpasses 50% of its metropolitan area, one of the highest in South Asia, highlighting the urgent need for adaptive urban governance. The policymakers can prioritize restoring pervious surfaces through green–blue infrastructure expansion, promoting sustainable drainage systems, and reinforcing planning regulations to counteract urban heat risks. Besides, future investigations should incorporate higher-resolution imagery for image and field data and ensemble other machine learning algorithms for change detection to establish predictive models for urban ecology and planning.

**Acknowledgements**

The authors express their sincere gratitude to the Department of Water Resources Engineering, Bangladesh University of Engineering and Technology (BUET), for continuous academic guidance and institutional support throughout this research. The authors also acknowledge the Survey of Bangladesh (SoB) and the Bangladesh Bureau of Statistics (BBS) for providing essential spatial and administrative datasets that significantly contributed to the geospatial analysis and boundary delineation. Appreciation is further extended to the United States Geological Survey (USGS) for open access to the Landsat satellite imagery, and to Google Earth Pro for high-resolution optical data that facilitated manual digitization and accuracy validation.

**Data availability**

The data will be made available upon request to the corresponding author.

**Conflict of interest**

The authors declare that there is no conflict of interest regarding the publication of this paper.

**References**

Abbasi, M., Popy, S., Yumin, T. (2022). Quantifying spatiotemporal changes of the urban impervious surface of Dhaka District using remote sensing technology. Indonesian Journal of Geography, 54(3). https://doi.org/10.22146/ijg.72506

Ahmad, M. N., Shao, Z., Xiao, X., Fu, P., Javed, A., Ara, I. (2024). A novel ensemble learning approach to extract urban impervious surface based on machine learning algorithms using SAR and optical data. International Journal of Applied Earth Observation and Geoinformation, 132, 104013. https://doi.org/10.1016/j.jag.2024.104013

BBS (Bangladesh Bureau of Statistics). (2022). Statistical yearbook of Bangladesh 2022. Dhaka, Bangladesh.

Bashar, T., Uddin, M. Z. (2025). Effects of land use change on surface runoff and infiltration: The case of Dhaka City. Urban Science, 9(12), 497. https://doi.org/10.3390/urbansci9120497

Chen, L., Zhou, B., Man, W., Liu, M. (2020). Landsat-based monitoring of the heat effects of urbanization directions and types in Hangzhou City from 2000 to 2020. Remote Sensing, 13(21), 4268. https://doi.org/10.3390/rs13214268

Faridatul, M. I., Wu, B., Zhu, X. (2019). Assessing long-term urban surface water changes using multi-year satellite images: A tale of two cities, Dhaka and Hong Kong. Journal of Environmental Management, 243, 287–298. https://doi.org/10.1016/j.jenvman.2019.05.019

Faisal, A., Kafy, A. A., Al Rakib, A., Akter, K. S., Jahir, D. M. A., Sikdar, M. S., Ashrafi, T. J., Mallik, S., Rahman, M. M. (2021). Assessing and predicting land use/land cover, land surface temperature, and urban thermal field variance index using Landsat imagery for the Dhaka Metropolitan area. Environmental Challenges, 4, 100192. https://doi.org/10.1016/j.envc.2021.100192

Hu, Y., Zhan, H., He, Q., Zhan, W. (2024). Assessment of atmospheric correction algorithms for Landsat-8/9 operational land imager over inland and coastal waters. Remote Sensing, 17(17), 3055. https://doi.org/10.3390/rs17173055

Jombo, S., Adelabu, S. (2023). Evaluating Landsat-8, Landsat-9 and Sentinel-2 imageries in land use and land cover (LULC) classification in a heterogeneous urban area. GeoJournal, 88(Suppl 1), 377–399. https://doi.org/10.1007/s10708-023-10982-8

Kocaman, B., Ağaçcıoğlu, H. (2024). Assessment of the impact of land use/land cover changes on carbon emissions using remote sensing and deep learning: A case study of the Kağıthane Basin. Sustainability, 17(23), 10690. https://doi.org/10.3390/su172310690

Kulsum, U., Moniruzzaman, M. (2022). Exploring the relationship of climate change and land-use dynamics with satellite-derived surface indices and temperature in greater Dhaka, Bangladesh. Journal of Earth System Science, 131, 117. https://doi.org/10.1007/s12040-022-01841-0

Li, C., Chen, B., Wang, X., Wu, Z., Lan, G., Azmi Tohiran, K., Amit, B., Lai, H., Wang, G., Yun, T., Kou, W. (2024). Integrating multi-temporal Landsat and Sentinel data for enhanced oil palm plantation mapping and age estimation in Malaysia. Remote Sensing, 17(16), 2908. https://doi.org/10.3390/rs17162908

Li, Y., Yang, X., Wu, B., Zhao, J., Deng, X. (2023). Impervious surface mapping based on remote sensing and an optimized coupled model: The Dianchi basin as an example. Land, 12(6), 1210. https://doi.org/10.3390/land12061210

Mondal, I., Bandyopadhyay, J., Hossain, S. A., et al. (2025). Evaluating the effects of rapid urbanization on the encroachment of the East Kolkata Wetland ecosystem: A remote sensing and hybrid machine learning approach. Environment, Development and Sustainability, 27, 14781–14813. https://doi.org/10.1007/s10668-024-05832-7

Moniruzzaman, M., Thakur, P. K., Kumar, P., Ashraful Alam, M., Garg, V., Rousta, I., Olafsson, H. (2020). Decadal urban land use/land cover changes and its impact on surface runoff potential for the Dhaka City and surroundings using remote sensing. Remote Sensing, 13(1), 83. https://doi.org/10.3390/rs13010083

Rentachintala, L. R. N. P., Reddy, M. G. M., Mohapatra, P. K. (2022). Urban stormwater management for sustainable and resilient measures and practices: A review. Water Science and Technology, 85(4), 1120–1140. https://doi.org/10.2166/wst.2022.017

Shao, Z., Cheng, T., Fu, H., Li, D., Huang, X. (2022). Emerging issues in mapping urban impervious surfaces using high-resolution remote sensing images. Remote Sensing, 15(10), 2562. https://doi.org/10.3390/rs15102562

Sohn, W., Kim, J., Li, M., Brown, R. D., Jaber, F. H. (2020). How does increasing impervious surfaces affect urban flooding in response to climate variability? Ecological Indicators, 118, 106774. https://doi.org/10.1016/j.ecolind.2020.106774

Sonet, M. S., Hasan, M. Y., Kafy, A., Shobnom, N. (2025). Spatiotemporal analysis of urban expansion, land use dynamics, and thermal characteristics in a rapidly growing megacity using remote sensing and machine learning techniques. Theoretical and Applied Climatology, 156, 79. https://doi.org/10.1007/s00704-024-05264-3

Soufiane, I. M., Djaouad, R. D., Farah, B., Djamel, S. (2025). Spatiotemporal impact of urbanization on urban heat island using Landsat imagery in Oran, Algeria: 1984–2024. Urban Science, 9(4), 95. https://doi.org/10.3390/urbansci9040095

Stern, A. J., Daughtry, C. S., Hunt, E. R., Gao, F. (2022). Comparison of five spectral indices and six imagery classification techniques for assessment of crop residue cover using four years of Landsat imagery. Remote Sensing, 15(18), 4596. https://doi.org/10.3390/rs15184596

Su, S., Tian, J., Dong, X., Tian, Q., Wang, N., Xi, Y. (2022). An Impervious Surface Spectral Index on Multispectral Imagery Using Visible and Near-Infrared Bands. Remote Sensing, 14(14), 3391. https://doi.org/10.3390/rs14143391

Sun, C., Chen, H., Fan, F. (2019). Improving accuracy of impervious surface extraction based on a threshold hierarchical method (THM). Applied Sciences, 10(23), 8409. https://doi.org/10.3390/app10238409

Van Nguyen, M., La, O. T., Nguyen, H. T. T., et al. (2025). Landsat 8 OLI atmospheric correction neural network for inland waters in tropical regions. International Journal of Environmental Science and Technology, 22, 6769–6788. https://doi.org/10.1007/s13762-024-06080-y

Wu, Y., Pan, J. (2023). Detecting changes in impervious surfaces using multi-sensor satellite imagery and machine learning methodology in a metropolitan area. Remote Sensing, 15(22), 5387. https://doi.org/10.3390/rs15225387

Xu, L., Sun, G., Zhang, A., Han, Z., Li, Z., Zhao, Y. (2025). Automatic mapping of high-resolution impervious surfaces driven by hierarchical adaptive features. Science of Remote Sensing, 12, 100300. https://doi.org/10.1016/j.srs.2025.100300

Yan, L., Roy, D. (2025). Using Landsat 8 and 9 operational land imager (OLI) data to characterize geometric distortion and improve geometric correction of Landsat multispectral scanner (MSS) imagery. Remote Sensing of Environment, 321, 114679. https://doi.org/10.1016/j.rse.2025.114679

Zhang, J., Du, J., Fang, S., Sheng, Z., Zhang, Y., Sun, B., Mao, J., Li, L. (2022). Dynamic changes, spatiotemporal differences, and ecological effects of impervious surfaces in the Yellow River Basin, 1986–2020. Remote Sensing, 15(1), 268. https://doi.org/10.3390/rs15010268

# Assessment of Land Cover Dynamics in Cox's Bazar, Bangladesh: An Integrated Machine Learning and Remote Sensing Approach

Md Mahfuzur Rahman[a,b]* and Mahazuza Islam[a]

[a]*Undegraduate Student, Department of Environmental Science, Stamford University Bangladesh (SUB)*

[b]*Research Assistant, Department of Environmental Science, Stamford University Bangladesh (SUB)*

**Corresponding author:* *mahfujr199@gmail.com* *(Md Mahfuzur Rahman)*

**Article info**

***Keywords:***

*Rohingya Refugee Crisis,*
*Google Earth Engine,*
*Random Forest,*
*Forest Loss,*
*Protected Area*

**Article History:**
Received-07 Dec 2025
Revised-12 Jan 2026
Accepted-01 Feb 2026
Published- 31 March 2026

**DOI:**
https://doi.org/10.66268/jrse.2026.05.774134

**ABSTRACT**

This study aims to assess the land cover dynamics using machine learning and remote sensing techniques in the Google Earth Engine (GEE) over the period 2016-2024 in Cox's Bazar, Bangladesh, which is hosting a million Rohingya refugees. Here, the Land Use Land Cover (LULC) changes show the decline in forest cover from 66,024 ha (26.46%) in 2016 to 42,865 ha (17.13%) in 2024. The built-up areas expanded dramatically from 3,746 ha (1.5%) to 15,036 ha (6.02%), linked to the rapid growth of Rohingya refugee settlements. Besides, the shrubland and water-bodies showed strong inter-annual fluctuations influenced by both environmental conditions and human activities. Furthermore, the Normalized Difference Vegetation Index (NDVI) analysis reflects the highest vegetation loss in Ukhiya upazila, where the largest refugee camps are located. The analysis of the study showed that the camps are extended to the protected areas. The accuracy of the LULC analysis confirmed accepted classifications with overall accuracy of 76-96% and Kappa values of 0.70-0.95. The rapid LULC changes driven by the refugee influx require the need for continuous monitoring and sustainable land management to prevent the expansion of camps into the protected areas, as evidenced by this study.

## 1. Introduction

Natural and man-made features that physically cover the earth's surface are called land cover, and when humans utilize the land for economic, residential, recreational, or conservation is called land use (Anderson et al., 1976; Babaremu et al., 2024). Changes of LULC have significant effects, such as environmental impacts including global warming, hydrological cycle, rainfall pattern, carbon sequestration, ecosystem impacts including habitat destruction, biodiversity loss, and socio-economic impacts including challenges to water resource management, agricultural productivity (Hassan et al., 2018; Siddeqa et al., 2023). Following the inflow of Rohingya refugees from 1942 has been an observation of the changes in LULC to protect the preserved area, national parks, and sanctuary (Hossain and Moniruzzaman, 2021). The problem of the refugee crisis is growing day by day with an average of 28,300 people forced to flee their homes (Hassan et al., 2018). Among them Rohingya people are one of the most stateless and widely persecuted Muslim minorities, forced by the Buddhist majority in Myanmar (Hassan et al., 2018; Ahmed et al., 2020). Major Influxes of the Rohingya Population occurred in 1942, 1991, 1997, 2016, and 2017 due to military restrictions of the

Myanmar Government, and almost 15.7 lakh Rohingya came to Bangladesh from 1942 to 2017 (ACAPS, 2017). On August 25, 2017, nearly 671,500 Rohingya refugees were forcibly displaced to the Teknaf and Ukhiya sub-districts of Cox's Bazar in Bangladesh from Rakhine State of Myanmar (Sakamoto et al., 2021). In response to the humanitarian crisis at that time, the Bangladesh Government provided land to build temporary settlements by clearing forest trees in the southern hilly region for the Rohingya people (Sarkar et al., 2023).

At present, a total of 34 camps are housed for Rohingya people, and these are located at Teknaf and Ukhiya near protected areas called the Teknaf wildlife game reserve. The protected area is a home for both land and wetland species, including birds, bats, snakes, wild Asian elephants, monkeys, and other wild animals (Hassan et al., 2018). The region also has a vast array of plants supporting carbon storage (Hassan et al., 2018; Hossain and Moniruzzaman, 2021). Geologically, the area belongs to the Eastern Fold Belt formed by the compressional interaction between the Indian Plate and the Myanmar Subduction Zone (Sourav, 2025; Rahim, 2025). Major features like the NNW-SSE trending Inani Anticline and older fault zones are created by this tectonic activity and reflect a long history of subsidence and upliftment. The landscape is fundamentally shaped by neo-tectonic uplift and fault zones, which generate coastal cliffs and a geologically dynamic, fragile environment (Rahim, 2025). The area is situated in a tropical monsoon climate experiencing distinct wet and dry seasons, where heavy monsoon rainfall exacerbates geohazards like landslides and coastal erosion (Sourav, 2025). But the government constructed Rohingya camps in the area of the protected zone in Teknaf and Ukhiya Upazila by cutting forested trees without any planned and baseline study, which hurt the surrounding environment by changing the land use and land cover of that area (Hasan et al., 2020; Siddeqa et al., 2023).

While many studies have assessed the changes of LULC using supervised maximum likelihood classification in ArcMap (Sarkar et al., 2023; Siddeqa et al., 2023). Methodological advancement in the field of GIS and remote sensing shifted toward using cloud-based platforms, Google Earth Engine (GEE), and robust Machine Learning (ML) algorithms for improved accuracy in time-series LULC analysis (Maruf and Ara, 2023; Miah et al., 2024; Das et al., 2025). Keeping all the reasons in view, the study aims to create maps showing LULC changes of Cox's Bazar district from 2016 to 2024 using a machine learning algorithm, random forest classifiers in Google Earth Engine (GEE) for continuous monitoring. In such a context, the objectives of this study are to assess the LULC change over the past decades in Cox's Bazar, Bangladesh, considering the Rohingya influx of 2016 and 2024.

## 2. Materials and Methods

### 2.1 Study area

This study covers Cox's Bazar district, as most Rohingya refugee camps are located here. Cox's Bazar is situated in the southeastern coastal belt of Bangladesh, extending between 91°50′E and 92°23′E in longitude and 20°43′N and 21°56′N in latitude (Rahim, 2025). The district is bounded by Chattogram District to the north, Bandarban District to the east, Myanmar, and the Bay of Bengal to the south and southeast (Fig. 1). Cox's Bazar holds significant geographical, economic, and political importance for the country. The study area is dominated by hills and natural forests along the Bay of Bengal, is a salinity-prone region with limited agricultural potential (Karmakar et al., 2025). The geomorphic features of this coastal plain include wave-cut platforms, benches, paleo-beaches, and alternating tidal and beach deposits formed by past sea-level fluctuations and wave action (Ahsan et al., 2017).

### 2.2. Geospatial data used

In this study, median composites covering a year, January to December, were used to obtain cloud-free and seasonally balanced imagery. Previous studies have shown that annual composites are less noisy to the atmosphere and have stable spectral contributions that can be used to map land-cover accurately (Phan et al., 2020; Zhang et al., 2021). Each study year, a median composite was generated using all available Sentinel-2 imagery from January to December with a cloud-coverage threshold of ≤5%. Due to tile availability and partial scene coverage during the early phase of the mission, the 2016 composite required extending the range to January 10, 2017, and the 2017 composite accordingly began from that date. Sentinel-2 MSI provides 13 spectral bands covering the visible to SWIR regions, which is crucial for detailed environmental monitoring (ESA, 2015; USGS, 2018).

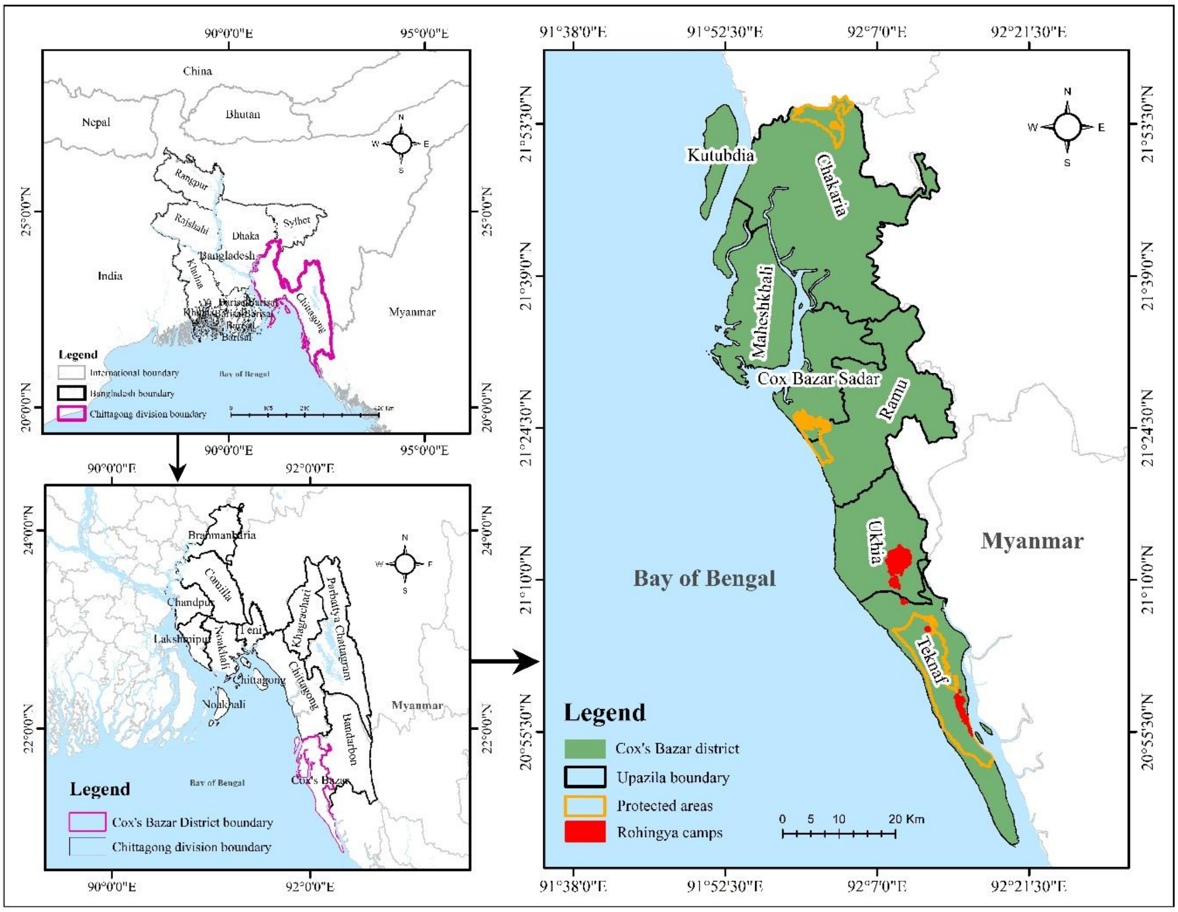


**Fig. 1.** Map of the study area showing the regional and local boundaries and the area of interest

The spatial resolution of Sentinel-2 MSI varies by band: four bands (B2, B3, B4, B8) have a 10 m ground sampling distance, six bands (B5, B6, B7, B8A, B11, B12) have 20 m resolution, and three coarse bands (B1, B9, B10) operate at 60 m that are useful in vegetation, moisture and atmospheric analysis (ESA, 2015) with a 12-bit radiometric resolution and a 290 km swath with wide-area coverage suitable for multi-temporal land assessments (Drusch et al., 2012; ESA, 2015). To understand the spatial patterns of the Rohingya camps in relation to protected areas, a polygon for Cox's Bazar was used. Subsequently, polygons representing Rohingya camps, national administrative boundaries, international boundaries, and national rivers were used, as listed in Table 1.

**Table 1**. Types of data used in this study

| Raster data | | | |
|---|---|---|---|
| Data | Year | | Source |
| | Start and End date | | |
| Sentinel-2A/2B | 2016-01-01 | 2017-01-10 | European Space Agency (ESA) |
| | 2017-01-10 | 2017-12-31 | |
| | 2018-01-01 | 2018-12-31 | |
| | 2019-01-01 | 2019-12-31 | |
| | 2020-01-01 | 2020-12-31 | |
| | 2021-01-01 | 2021-12-31 | |
| | 2022-01-01 | 2022-12-31 | |
| | 2023-01-01 | 2023-12-31 | |
| | 2024-01-01 | 2024-12-31 | |

| Vector data | |
|---|---|
| Data | Source |
| Protected area boundary | UNEP-WCMC and IUCN (2025), www.protectedplanet.net. |
| River boundary and Rohingya camps | Hdx, 2025 (https://data.humdata.org/dataset/outline-of-camps-sites-of-rohingya-refugees-in-cox-s-bazar-bangladesh) |
| Administrative boundary | DIVA-GIS, 2024 (https://diva-gis.org/data.html) |

## 2.3. Methodology

### 2.3.1 Image pre-processing

Fig. 2 shows the overall workflow of this study. The workflow commenced with importing the study area shape file into the GEE platform. Subsequently, the data preparation phase has started with the acquisition of nine Sentinel-2 MSI images for individual years from 2016 to 2024. In this study, we collected the images from the COPERNICUS/S2 collection. Similar to previous studies (Valdivieso-Ros et al., 2021), we selected the COPERNICUS/S2 (TOA) collection in GEE to ensure full spatial coverage. We then performed manual atmospheric correction, as some atmospherically corrected datasets (e.g., SR or harmonized) either lacked full coverage or had gaps due to masking. Images were collected with less than 5% cloud coverage to minimize atmospheric disturbances in the datasets. Radiometric correction was done through the transformation of raw digital values into the top-of-atmosphere (TOA) reflectance. Minimizing residual atmospheric effects, e.g., haze, was then done by atmospheric correcting, i.e., finding the darkest pixel of each spectral band and subtracting it of every pixel in that spectral band (Abdullah et al., 2019).

### 2.3.2. Image classification

Image classification is the process of assigning each pixel in a satellite image to a specific land-cover class based on its spectral characteristics, and it applies to both supervised and unsupervised methods (Corner et al., 2022). In this study, we employed supervised image classification, and for this, we established a detailed land use and land cover classification outline based on the characteristics of the area. As the Cox's Bazar district is usually surrounded by variations in vegetation cover, saltpan, waterbodies, coastal wetland, and cropland, there was a need to come up with a classification scheme. Here, five different categories of LULC have been considered, such as forest cover (natural forest and homestead vegetation), Cropland/fallow land (crop fields, saltpans, grassland, and open fields), Built-up (settlements, roads, and brickfields), Waterbody (rivers, lakes, and ponds), and Shrubland (low to medium vegetation coverage dominated by small to medium-sized bush). In the cropland category, fallow fields, exposed soil, and sandy beaches were included because they share similar spectral characteristics, making them difficult to separate reliably.

Furthermore, the indices like Normalized Difference Vegetation Index (NDVI), Normalized Difference Water Index (NDWI), and Normalized Difference Built-up Index (NDBI) improve the separability of land-cover classes and enhance classification accuracy by highlighting vegetation, water, and built-up areas (Xu, 2006; Arfa and Minaei, 2024). In Google Earth Engine (GEE) classification workflow, the study utilizes five band-composite combinations (true color, standard false-color, urban false-color, agricultural composite, and SWIR composite) and calculated five normalized spectral indices, including NDVI, NDWI, NDBI, NDMI, and SBI from spectral bands to determine features of each land-use/land-cover by analyzing spectral signatures of these band combinations and indices. Normalized Difference Vegetation Index (NDVI) is a metric that is used to assess the vegetation health and density by calculating the differences between the near-infrared and red bands and is formulated by Rouse et al. (1973). The indices widely used to understand different types of vegetation by analyzing the index value, which ranges from -1 to +1 (Xue & Su, 2017). In this study, NDVI is used to determine the dense forest shrubland and cropland by analyzing its spectral signature by calculating NDVI with the following formula Eq. (1). The term NDWI is used to assess water content in open water by calculating the differences between the green and near-infrared bands and is formulated (McFeeters, 1996). Spectral signature of these indices is analyzed to distinguish saltpans, which frequently resemble waterbodies in satellite imagery, using the following formula Eq. (2). Also, the spectral signature of Normalized Difference Built-up Index (NDBI) is analyzed to built-up areas due to high SWIR reflectance by using the following formula Eq. (3) (Zha et al., 2003). Normalized Difference Moisture Index (NDMI)/NDWI estimates vegetation or soil moisture content (Gao, 1996). Soil Brightness Index (SBI) quantifies soil brightness and organic matter based on multi-band reflectance and helps to distinguish bare soil surfaces (Kauth and Thomas, 1976).

**Table 2**. The different indices used in the LULC classification

| Equations | | Reference |
|---|---|---|
| $NDVI=\frac{NIR-Red}{NIR+Red}$ | ……………………………(1) | Rouse et al., 1973 |
| $NDWI=\frac{Green-NIR}{Green+NIR}$ | …………………………... (2) | McFeeters, 1996 |
| $NDBI=\frac{SWIR-NIR}{SWIR+NIR}$ | …....................…………(3) | Zha et al., 2003 |
| $NDMI=\frac{NIR-SWIR}{NIR+SWIR}$ | ………………………………(4) | Gao, 1996 |
| $SBI=\sqrt{(Red^2+Green^2+Blue^2)}$ | ……………………………(5) | Kauth and Thomas, 1976 |

By integrating these five indices with six spectral composites, we took training samples (pixel-based) by analyzing their spectral signature. NDVI is especially useful for delineating dense forest and shrubland. NDWI and NDMI help to discriminate between waterbodies and saltpans containing water, NDBI and SBI enhance detection and reduce confusion between barren land and tin shed settlements of Rohingya refugees, as they reflect the similar wavelength of barren land.

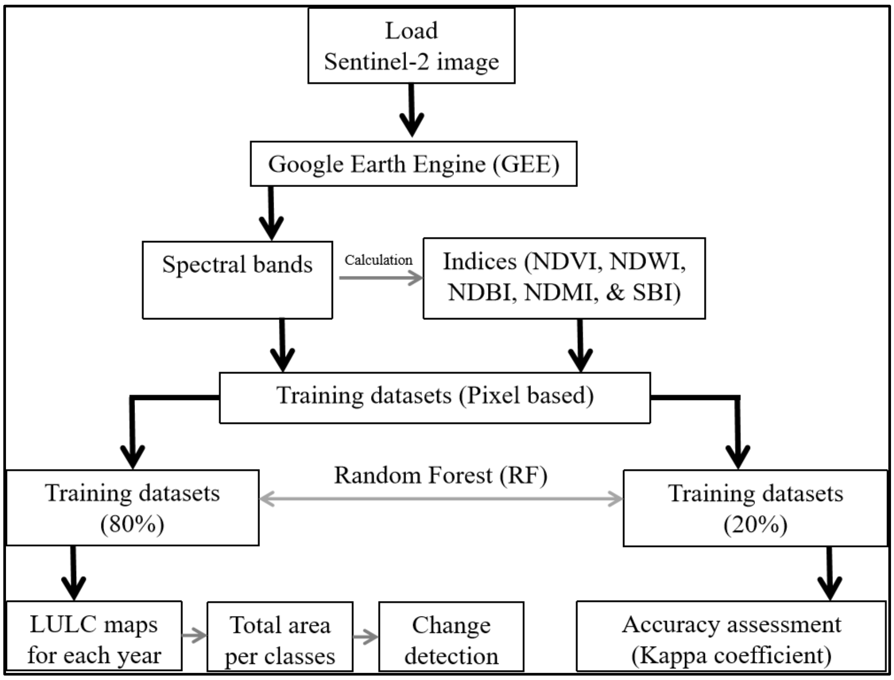


**Fig. 2.** A detailed workflow of the study

### 2.3.3 Machine learning algorithm in LULC classification

Machine Learning (ML) techniques have become central in LULC classification as they handle non-linear spectral variability and high-dimensional data as compared to classical parametric techniques (Talukdar et al., 2020). The K-Nearest Neighbors (KNN) is an instance-based non-parametric technique that generalizes samples of data according to the most frequently occurring class of the nearest neighbors, although it can fail in high-dimensional spectral data and noisy data (Altman, 1992; Pal and Mather, 2003). Artificial Neural Networks (ANN) can approximate non-linear relationships and have already been successfully applied to LULC mapping, but they can be very sensitive to large datasets used in training and tuning the network to prevent the risk of overfitting (Qian et al., 2015; Haykin, 1999). Gradient Boosting Machines (GBM) have demonstrated high predictive power due to the successive combination of weak learners to reduce the effects of bias, which is highly accurate when working with multispectral and hyperspectral data, but GBM is computationally expensive and highly sensitive to hyperparameter optimization (Friedman, 2001; Qian et al., 2015). Support Vector machine (SVM) is popular because of its high capacity of generalization, it can build an explicit decision boundary with a margin, and can also be effective when dealing with non-linear separability through kernel functions, and is capable of producing high classification accuracy with relatively few training samples (Huang et al., 2002; Pal and Mather, 2005; Camps-Valls et al., 2013). Random Forest (RF) is a non-parametric, ensemble-based algorithm that constructs multiple decision trees and averages their predictions, which helps to be resistant to noise, multicollinearity of spectral indices, and overfitting, and also allows a measure of variable importance to interpret the LULC separability (Breiman, 2001; Belgiu & Drăguţ, 2016; Sun & Ongsomwang, 2023). Convolutional Neural Networks (CNNs), a deep-learning approach, excel at capturing both spectral and spatial patterns in very-high-resolution imagery, yielding high accuracy, but they require substantial labeled data, computational resources, and careful network tuning to avoid overfitting.

### 2.3.4. Accuracy assessment

To fulfill the objectives of the study, a machine learning algorithm was adopted after assessing the accuracy matrix of the chosen ML algorithm, following a clear literature review (2.3.3). Three ML were adopted for evaluation for further analysis, these are RF, SVM, and KNN. Evaluation was performed for the year 2016 LULC classification. LULC Classification and its accuracy assessment were performed by splitting the training samples into 80%/20% as training and validation points, applying a stratified random sampling approach in Google Earth Engine (Gorelick et al., 2017; Roy, 2021). A confusion matrix between predicted classes and actual ground-truth was obtained by using the validation dataset. The counts of the true positives (TP), true negatives (TN), false positives (FP), and false negatives (FN) in each cell of the matrix measure the accurate and inaccurate predictions of each classification (Belgiu and Drăguţ, 2016). The study has calculated four accuracy matrices (Producer's accuracy, User's accuracy, Overall training accuracy, and Kappa coefficient) by producing a confusion matrix for each year, these are:

$$\text{Producer accuracy} = \frac{\text{Total number of correct pixel in a class}}{\text{Total number of reference pixel in that class (column total)}} \ldots\ldots\ldots(6)$$

$$\text{User accuracy} = \frac{\text{Total number of correct pixel in a class (Diagonal element)}}{\text{Total number of pixel classified into that class (raw total)}} \ldots\ldots\ldots\ldots(7)$$

$$\text{Overall accuracy} = \frac{\text{Total number of correctly classified pixels (sum of diagonal)}}{\text{Total number of reference pixels}} \qquad (8)$$

$$\text{Kappa coefficient}, \kappa = \frac{P_o - P_e}{1 - P_e} \qquad (9)$$

In 2016, the overall accuracy of the Random Forest was 85.48% and the κ of 0.81 (almost perfect agreement), compared to SVM (77%, κ = 0.70) and KNN (89%, κ = 0.79) (Table 3). Based on the analysis of the accuracy assessment of the RF, SVM, and KNN, this research applied the Random Forest algorithm since it has high precision due to the combination of several decision trees, moderate training samples, low sensitivity to multicollinearity between spectral indices, and inbuilt variable importance metrics, which assist in interpreting LULC separability (Mutale et al., 2024). The study then used Random Forest to classify the land use/land cover of Cox's Bazar for the years (i.e., 2016, 2017, 2018, 2019, 2020, 2021, 2022, 2023, and 2024).

**Table 3.** Comparative accuracy assessment of ML classifiers of 2016

| Classifiers | Overall accuracy (OA) (%) | Kappa Coefficient |
|---|---|---|
| Random forest (RF) | 85.48 | 0.81 |
| Support Vector Machine (SVM) | 77 | 0.70 |
| K-Nearest Neighbors (KNN) | 89 | 0.79 |

## 3. Results and Discussion

### 3.1. Assessment of LULC change and NDVI-based vegetation coverage

The study observed a consistent decline in forest cover, dropping from 66,024 ha (26.46%) in 2016 to 42,865 ha (17.13%) in 2024, about 9.33%. Shrubland also declined substantially, losing 23,856.3 ha (9.54%) from 2016-2024 (Table 5). Results of the classification are similar to several studies that have examined the changes in forest cover. The study of Dampha et al. (2022) showed that the forest/grassland decreased by nearly 20% (2017-2020). Besides, the study of Sarker et al. (2022) showed that the forest cover of Teknaf and Ukhiya Upazila decreased by 9%. In contrast to the declining forest cover and shrubland, cropland/fallow land expanded steadily throughout the study period. Built-up areas increased significantly from 1.5% to 6.02%, and it is mostly associated with refugee settlements (Fig. 4). Shrub-land and water-bodies showed strong inter-annual fluctuations influenced by environmental conditions, seasonal changes, and anthropogenic activities. Year-to-year trends showed clear transitions across land cover classes. The built-up area increased for 1.5% to 4% from 2016 to 2017, this drastic change was mainly due to the Rohingya influx (Hassan et al., 2018) (Fig. 4). After the dramatic jump in 2016-2017 built-up area continued to grow steadily from 2017-2024, with a moderate rise in 2018, 2019, and 2020. The growth remained consistent before showing a slightly higher increase again in 2023–2024, indicating continuous but mostly gradual urban expansion. Cropland and fallow land increased steadily from 2016 onward. The total area of cropland and fallow land was 129,876 ha (52.05 %) in 2024, compared to 90,653 ha (36.31%) in 2016, which represented the largest spatial extent. Shrubland was decreasing in the early years, reaching its lowest point in 2018, which was 35,702 ha (14.3%). After that, shrubland slowly increased and became more stable from 2020. By 2024, shrubland covered a bit more area, 53,178 ha (21.3%), showing a slow recovery after the big early decline. Waterbody area changed a lot over the years, with a clear rise in 2018 (23,882 ha) followed by lower levels in most other years. After 2019, it showed only small changes and stayed mostly low until 2024 by 3.5%.

The mean NDVI value of the district reflects overall vegetation cover that declined by nearly 14% from 2016 to 2024. In the present, Teknaf and Ukhiya Upazila, where refugee camps are located, were covered by green space or forest cover within and around the official refugee camp boundary in 2016, that clearly observed by this study’s LULC classification and the NDVI results (Fig. 3, 4, and 5). Teknaf and Ukhiya upazila mean NDVI value is decreased by 0.18 and 0.22, reflect the clear impact of the Rohingya refugee. Among these, Ukhiya Upazila has experienced the highest decline in vegetation cover, where the largest camp is located in the Kutupalong area (UNHCR, 2025). Mean NDVI of Chakaria, Cox’s Bazar Sadar, Kutubdia, and Maheshkhali shows a steady decline in relation to Ramu, Ukhiya, and Teknaf Upazila. Ramu Upazila had the highest forest decline in 2024 (8,184 ha; 30.83%), as it originally contained the largest forest area among all upazilas. Also, a large forest loss was observed in Teknaf (4,637 ha; 17.47%) and Ukhiya (4,565 ha; 17.20%), where all the refugee camps are located.

### 3.2. Accuracy assessment of LULC classification

The accuracy assessment for the LULC maps from 2016-2024 was done using confusion matrices to compare classified pixels with reference data. User’s Accuracy (UA) and Producer’s Accuracy (PA) were calculated for each land-cover class to see how correctly each class was identified and where mistakes happened. The Overall Accuracy (OA) values ranged from moderate to very high (76%-96%) (Table 4), indicating generally dependable classification results across the years. The kappa coefficients (0.70-0.95) indicate that the classifications were substantial to almost perfect agreement.

**Table 4**. Accuracy assessment of LULC from 2016 to 2024

| Year | Overall accuracy (%) | Kappa |
|---|---|---|
| 2016 | 85.48 | 0.81 |
| 2017 | 89.29 | 0.84 |
| 2018 | 89.80 | 0.87 |
| 2019 | 78.33 | 0.72 |
| 2020 | 96.00 | 0.95 |
| 2021 | 88.00 | 0.84 |
| 2022 | 90.57 | 0.88 |
| 2023 | 76.36 | 0.70 |
| 2024 | 81.03 | 0.75 |

### 3.3. Impacts of the Rohingya influx on the LULC change

The year 2017 marked an immediate influx, during which Cox’s Bazar experienced dramatic land-cover transformations that resulted in significant negative impacts on the surrounding environment (Hassan et al., 2018). Built-up area had increased 1.5% to 4% from 2016-2017 at the immediate influx of Rohingya refugees to accommodate them and provide related facilities. Cropland or open land expanded steadily, indicating increased land conversion for agricultural use to meet food demand as well as the availability of Rohingya refugees as cheap labor for agricultural work (Sakamoto et al., 2021; RRRC, 2025). Mean NDVI value of the district declined by nearly 0.14 from 2016-2024, and the highest decline was 0.22 in Ukhiya Upazila and a moderate decline of 0.18 in Teknaf Upazila, where all refugee camps are located near the reserved forest and wildlife sanctuary (RRRC, 2025) (Fig. 4, Fig. 5). Refugee population hosts more than one-third of the district's total population, and its density is approximately 40 times higher than the rest of Cox's Bazar, as is clearly evident by this study showing a massive decline in forest cover to give shelters to the refugees (HRRC, 2025). At a 3.77% growth rate, the refugee population could reach about 1.30 million in 2032, four times higher than the population projected for Teknaf in 2032. This indicates an increase in built-up areas to fulfill the demand of refugee camps in the near future.

The red area indicates refugee camps near the protected area, which is delineated by orange boundaries (Fig. 1). If the population growth rate of Rohingya refugees continues to increase rapidly, these settlements may expand into the protected area. Previous studies have shown that refugee settlements were built in 2017 by cutting down the trees of dense forest areas situated adjacent to the protected area. The area was a home for both land and wetland species, including birds, bats, snakes, wild Asian elephants, monkeys, and other wild animals, and had a vast array of plants supporting carbon storage (Hassan et al., 2018). To prevent the expansion of the refugee camp into the protected area, proper LULC planning is required. For that this study has analyzed the changes of LULC from 2016-2024 for each year and found that the camp area is expanded towards the protected area (Fig. 3). This study was done by Google Earth Engine for continuous monitoring to understand the dynamics of Refugee camps.

**Table 5.** Descriptive statistics of LULC change in hectare (ha) and percentage (%)

| LULC class | 2016 | 2017 | 2018 | 2019 | 2020 | 2021 | 2022 | 2023 | 2024 |
|---|---|---|---|---|---|---|---|---|---|
| Forest cover | 66,024 (26.46 %) | 61,689 (24.7 %) | 57,858 (23.16 %) | 54,664 (21.88 %) | 50,530 (20.23 %) | 50,201 (20.13 %) | 47,242 (18.9 %) | 45,046 (18.03 %) | 42,865 (17.13 %) |
| Cropland/ fallow land | 90,653 (36.31%) | 111,997 (44.88 %) | 121,252 (48.54 %) | 122,608 (49.13 %) | 124,150 (49.76 %) | 126,062 (50.55 %) | 128,886 (51.6 %) | 127,627 (51.16 %) | 129,876 (52.05 %) |
| Built-up | 3,746 (1.5 %) | 9,990 (4%) | 11,063 (4.43%) | 12,246 (4.91%) | 12,747 (5.11%) | 13,265 (5.31%) | 13,688 (5.48%) | 13,947 (5.59%) | 15,036 (6.02%) |
| Waterbody | 12,216 (4.89%) | 8,259 (3.31%) | 23,882 (9.57%) | 9,763 (3.91%) | 15,108 (6.05%) | 11,486 (4.6%) | 11,486 (4.6%) | 9,858 (3.95%) | 8,741 (3.5%) |
| Shrubland | 77,034 (30.84%) | 57,721 (23.11%) | 35,702 (14.3%) | 50,382 (20.17%) | 47,101 (18.85%) | 48,471 (19.41%) | 48,500 (19.42%) | 53,065 (21.27%) | 53,178 (21.3%) |

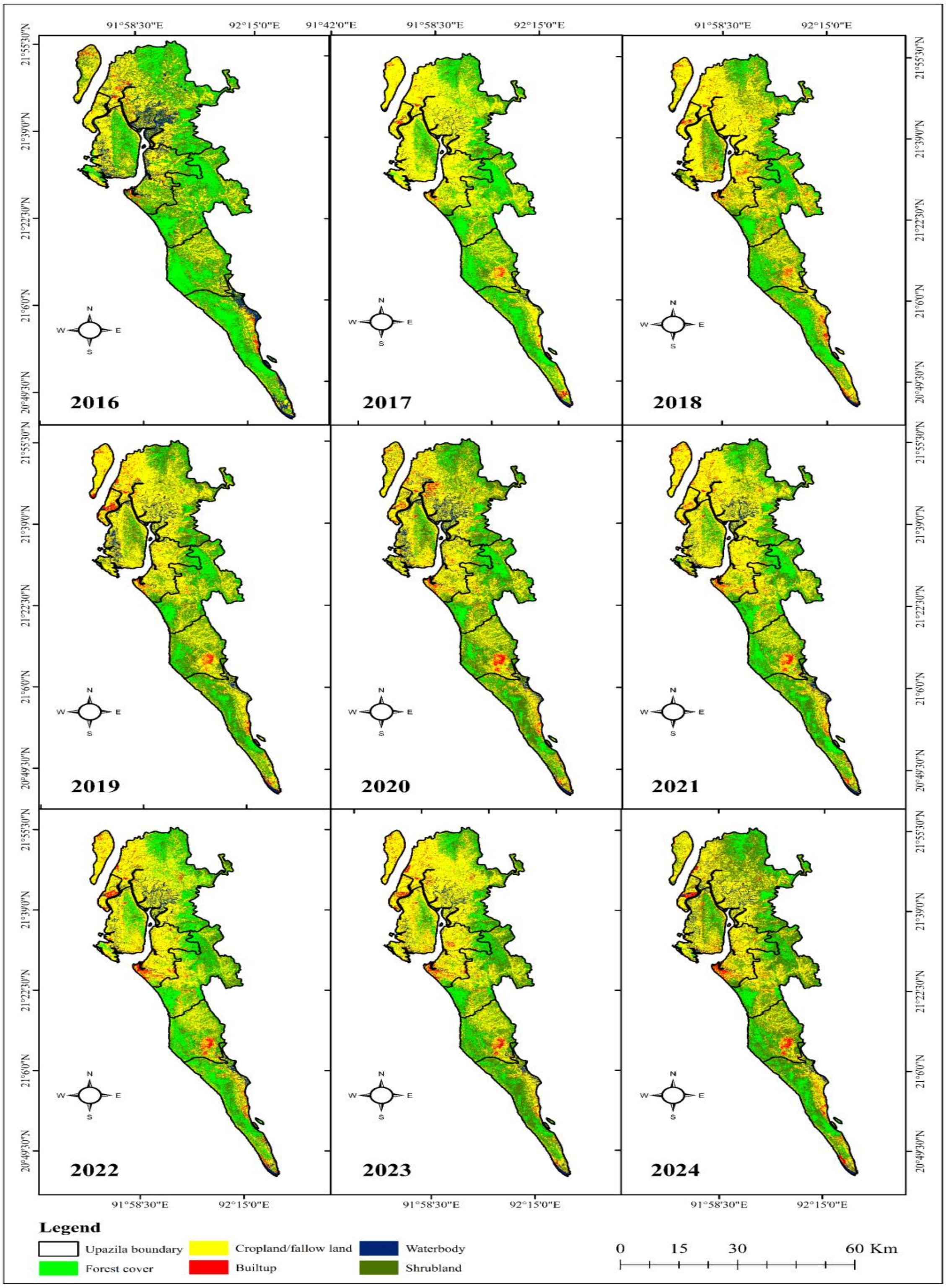


**Fig. 3**. LULC maps of the study area over the period (2016-2024)

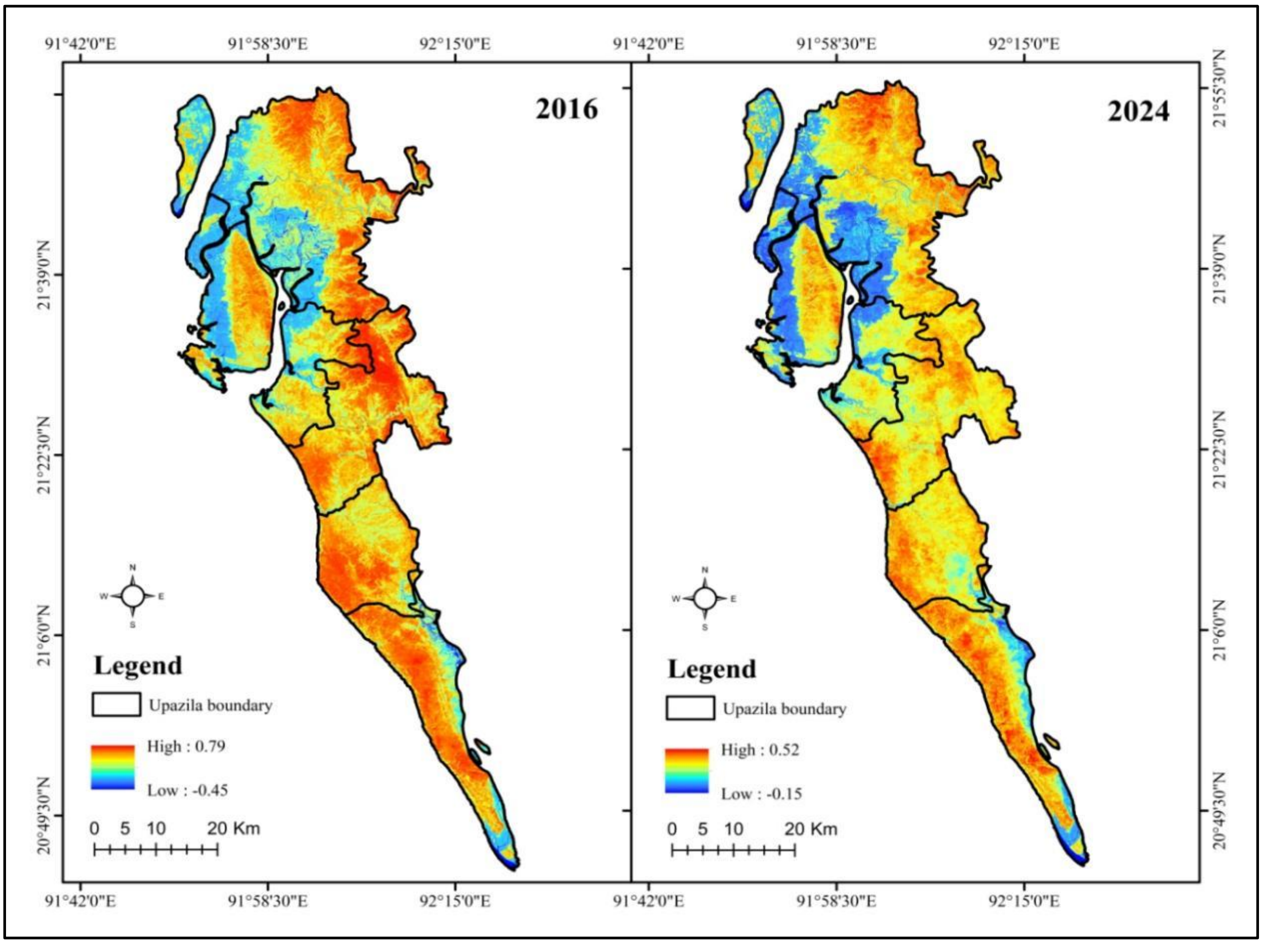


**Fig. 4.** Spatial distribution of mean NDVI in 2016 (left) and 2024 (right)

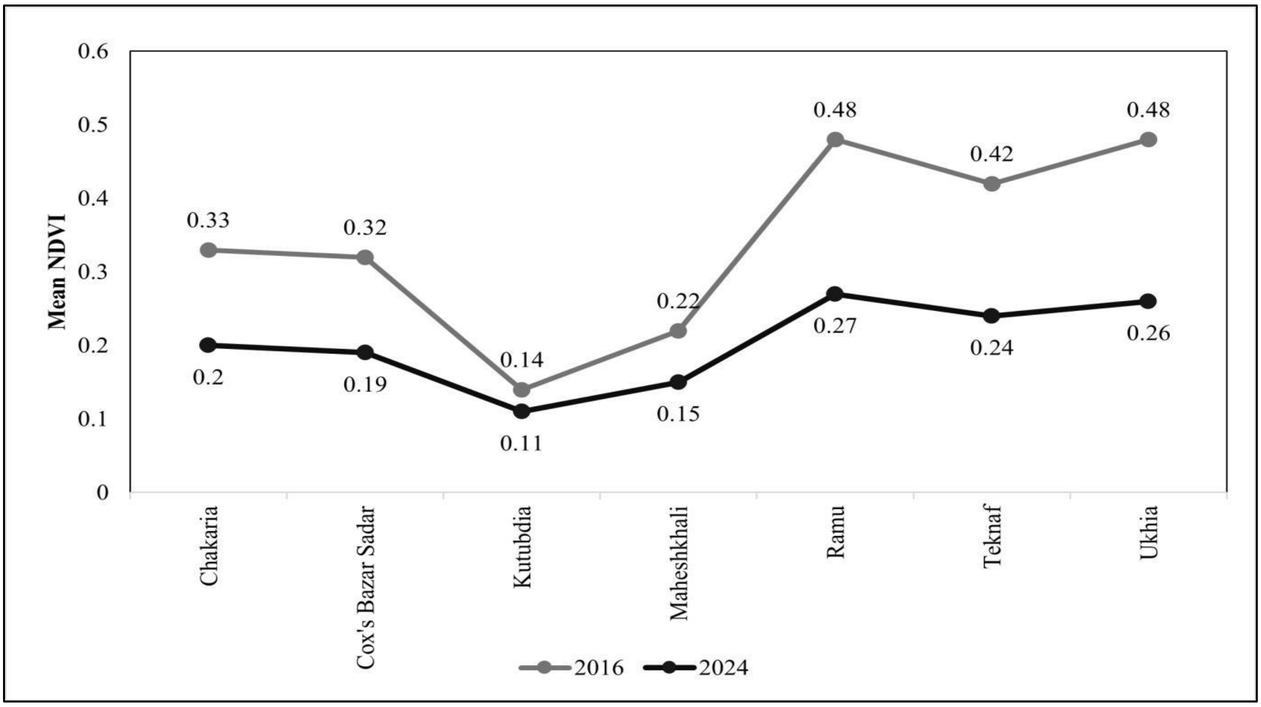


**Fig. 5.** Upazila-wise mean NDVI values of Cox’s Bazar district in 2016 and 2024

## 4. Conclusions

Findings of this study demonstrated that Cox's Bazar has undergone rapid and substantial LULC transformations, with the most dramatic changes occurring in 2017 during the immediate Rohingya influx. The findings give a clear picture of the rapid and extensive landscape change of Cox's Bazar due to the massive influx of Rohingya refugees. The loss of forest cover was around 9.5%, and the areas under built and agricultural land were growing significantly, which means that the pressure on natural ecosystems is high. The patterns of NDVI also verify that there was severe vegetation degradation in and around Teknaf and Ukhiya, the places where the refugee camp areas are located. The RF classifier produced reliable outputs, supporting its suitability for long-term monitoring. The effectiveness of cloud-based platforms for continuous, year-to-year monitoring by applying a random forest classifier in GEE. It enables real-time assessment of how refugee camps are expanding spatially and their encroachment on protected areas. These insights are vital for government agencies, conservation authorities, and NGOs to develop informed restoration strategies and sustainable land-use planning to protect the preserved forest and the Teknaf wildlife sanctuary.

**Acknowledgments**

The authors would like to thank the satellite data providers, particularly the European Space Agency (ESA). Also, we want to thank two anonymous reviewers and the editor for their critical but constructive comments to improve the manuscript.

**Data availability**

The data will be made available upon request to the corresponding author.

**Conflict of interest**

The authors declare that there is no conflict of interest regarding the publication of this paper.

**References**

Abdullah, A. Y. M., Masrur, A., Adnan, M. S. G., Baky, M. A. A., Hassan, Q. K., Dewan, A. (2019). Spatio-temporal patterns of land use/land cover change in the heterogeneous coastal region of Bangladesh between 1990 and 2017. Remote Sensing, 11(7), 790. https://doi.org/10.3390/rs11070790

ACAPS. (2017). Review Rohingya influx since 1978: Thematic report. ACAPS NPM Analysis Hub.

Ahmed, B., Rahman, M. S., Sammonds, P., Islam, R., Uddin, K. (2020). Application of geospatial technologies in developing a dynamic landslide early warning system in a humanitarian context: the Rohingya refugee crisis in Cox's Bazar, Bangladesh. Geomatics, Natural Hazards and Risk, 11(1), 446–468. https://doi.org/10.1080/19475705.2020.1730988

Ahsan, K., Habib, M. A., Alam, M. F., Talukder, A. (2017). Geological report on Cox's Bazar-Teknaf Coastal Area, Bangladesh (Records of the Geological Survey of Bangladesh, Vol. 14, Part 4). Geological Survey of Bangladesh.

Altman, N. S. (1992). An introduction to kernel and nearest-neighbor nonparametric regression. The American Statistician, 46(3), 175–185. https://doi.org/10.2307/2685209

Anderson, J. R., Hardy, E. E., Roach, J. T., Witmer, R. E. (1976). A land use and land cover classification system for use with remote sensor data (U.S. Geological Survey Professional Paper 964) [Report]. U.S. Geological Survey. https://pubs.usgs.gov/pp/0964/report.pdf

Arfa, A., Minaei, M. (2024). Utilizing multitemporal indices and spectral bands of Sentinel-2 to enhance land use and land cover classification with random forest and support vector machine. Advances in Space Research, 74, 5580–5590. https://doi.org/10.1016/j.asr.2024.08.062

Babaremu, K., Taiwo, O., Ajayi, D. (2024). Impacts of land use and land cover changes on hydrological response: a review of current understanding and implications for watershed and water resources management. TWIST, 19(1), 256–267. https://doi.org/10.5281/zenodo.10049652#89

Belgiu, M., Drăguţ, L. (2016). Random forest in remote sensing: A review of applications and future directions. ISPRS Journal of Photogrammetry and Remote Sensing, 114, 24–31. https://doi.org/10.1016/j.isprsjprs.2016.01.017

Breiman, L. (2001). Random forests. Machine Learning, 45(1), 5–32.

Camps-Valls, G., Tuia, D., Bruzzone, L., & Benediktsson, J. A. (2013). Advances in hyperspectral image classification: Earth monitoring with statistical learning methods. ArXiv. https://doi.org/10.1109/MSP.2013.2279179

Corner, R. J., Dewan, A. M., Chakma, S. (2022). Monitoring and prediction of land-use and land-cover (LULC) change. In S. K. Sarkar, S. S. Roy, & K. K. Mondal (Eds.), Remote Sensing, Environmental Management and Education (pp. 95–119). Springer.

Dampha, N. K., Salemi, C., Polasky, S. (2022). Rohingya refugee camps and forest loss in Cox's Bazar, Bangladesh: An inquiry using remote sensing and econometric approaches (Policy Research Working Paper No. 9948). World Bank Group.

Das, D., Prodhan, F. A., Hoque, M. Z., Haque, M. E., Kabir, M. H. (2025). Monitoring and future prediction of land use land cover dynamics in northern Bangladesh using remote sensing and CA-ANN model. Earth, 6(3), 73. https://doi.org/10.3390/earth6030073

DIVA-GIS. (2024). Global spatial data (administrative boundaries, roads, land cover, etc.) [Data set]. https://diva-gis.org/data.html

Drusch, M., Del Bello, U., Carlier, S., Colin, O., Fernandez, V., Gascon, F., Hoersch, B., Isola, C., Laberinti, P., Martimort, P., Meygret, A., Spoto, F., Sy, O., Marchese, F., Bargellini,

P. (2012). Sentinel-2: ESA's optical high-resolution mission for GMES operational services. Remote Sensing of Environment, 120, 25–36. https://doi.org/10.1016/j.rse.2011.11.026

European Space Agency. (2015). Sentinel-2 User Handbook (Issue 1, Rev. 2, 24 July 2015). https://sentinels.copernicus.eu/documents/247904/685211/Sentinel-User_Handbook

Friedman, J. H. (2001). Greedy function approximation: a gradient boosting machine. The Annals of Statistics, 29(5), 1189–1232. https://doi.org/10.1214/aos/1013203451

Gao, B. (1996). NDWI—A normalized difference water index for remote sensing of vegetation liquid water from space. Remote Sensing of Environment, 58(3), 257-266. https://doi.org/10.1016/S0034-4257(96)00067-3

Gorelick, N., Hancher, M., Dixon, M., Ilyushchenko, S., Thau, D., Moore, R. (2017). Google Earth Engine: planetary-scale geospatial analysis for everyone. Remote Sensing of Environment, 202, 18–27. https://doi.org/10.1016/j.rse.2017.06.031

Hasan, M. E., Mahmood, R., Zhang, L., Dewan, A. (2020). Spatiotemporal pattern of forest degradation and loss of ecosystem function associated with Rohingya influx: A geospatial approach. Land Degradation & Development, 32(3), 1184–1195. https://doi.org/10.1002/ldr.3821

Hassan, M. M., Smith, A. C., Walker, K., Rahman, M. K., Southworth, J. (2018). Rohingya refugee crisis and forest cover change in Teknaf, Bangladesh. Remote Sensing, 10(5), 667. https://doi.org/10.3390/rs10050667

Haykin, S. (1999) Neural Networks: A Comprehensive Foundation. 2nd Edition, Prentice- Hall, Englewood Cliffs, NJ.

Hossain, F., Moniruzzaman, M. (2021). Environmental change detection through remote sensing technique: A study of Rohingya refugee camp area (Ukhia and Teknaf sub-district), Cox's Bazar, Bangladesh. Environmental Challenges, 2, 100024. https://doi.org/10.1016/j.envc.2021.100024

Huang, C., Davis, L. S., Townshend, J. R. G. (2002). An assessment of support vector machines for land cover classification. International Journal of Remote Sensing, 23(4), 725–749. https://doi.org/10.1080/01431160110040323

HRRC (Human Rights Research Center). (2025, July 23). Crisis within a crisis: Environmental degradation in the Rohingya refugee settlement in Bangladesh. Human Rights Research Center.https://www.humanrightsresearch.org/post/crisis-within-a-crisis-environmental-degradation-in-the-rohingya-refugee-settlement-in-bangladesh#:~:text=Environmental%20Impacts,De%20La%20Portilla%2C%202021).

Humanitarian Data Exchange. (2025). Bangladesh water courses [Data set]. OCHA. https://data.humdata.org/dataset/bangladesh-water-courses

Humanitarian Data Exchange. (2025). Outline of camps/sites of Rohingya refugees in Cox’s Bazar, Bangladesh [Data set]. OCHA. https://data.humdata.org/dataset/outline-of-camps-sites-of-rohingya-refugees-in-cox-s-bazar-bangladesh

Karmakar, S., Rahman, M., Meng, L. (2025). Land Cover Changes and Land Surface Temperature Dynamics in the Rohingya Refugee Area, Cox Bazar, Bangladesh: An Analysis from 2013 to 2024. Atmosphere, 16(3), 250. https://doi.org/10.3390/atmos16030250

Kauth, R. J., & Thomas, G. S. (1976). The Tasselled Cap—A graphic description of the spectral-temporal development of agricultural crops as seen by LANDSAT. In Symposium on Machine Processing of Remotely Sensed Data (pp. 4B-4B). The Laboratory for Applications of Remote Sensing, Purdue University.

Maruf, J. K., Ara, S. (2023). Examining the Spatio-temporal changes of Ecosystem Service Value Due to LULC changes: A Case Study on Cox's Bazar, Bangladesh. Research Square. https://doi.org/10.21203/rs.3.rs-2500133/v1

McFeeters, S. K. (1996). The use of the Normalized Difference Water Index (NDWI) in the delineation of open water features. International Journal of Remote Sensing, 17(7), 1425–1432. https://doi.org/10.1080/01431169608948714

Miah, M. D., Hossain, M. A., Ali, Y. (2024). Assessment of the degradation of Teknaf Wildlife Sanctuary, Bangladesh: Use of Remote Sensing and Geographic Information System Techniques. Forestist, 74(3), 354–364. https://doi.org/10.5152/forestist.2024.24002

Mutale, B., Withanage, N. C., Mishra, P. K., Shen, J., Abdelrahman, K., Fnais, M. S. (2024). A performance evaluation of random forest, artificial neural network, and support vector machine learning algorithms to predict spatio-temporal land use–land cover dynamics: a case from lusaka and colombo. Frontiers in Environmental Science, 12, 1431645. https://doi.org/10.3389/fenvs.2024.1431645

RRRC (Relief and Repatriation Commissioner). Office of the Refugee, Government of Bangladesh (GOB). (2025). Rohingya refugee population factsheet (February 28, 2025)

Pal, M., Mather, P. M. (2003). An assessment of the effectiveness of decision tree methods for land cover classification. Remote Sensing of Environment, 86(4), 554–565. https://doi.org/10.1016/S0034-4257(03)00132-1

Pal, M., Mather, P. M. (2005). Support vector machines for classification in remote sensing. International Journal of Remote Sensing, 26(5), 1007–1011. https://doi.org/10.1080/01431160412331291837

Phan, T. N., Kuch, V., Lehnert, L. W. (2020). Land Cover Classification using Google Earth Engine and Random Forest Classifier—The Role of Image Composition. Remote Sensing, 12(15), 2411.

Qian, Y., Zhou, W., Yan, J., Li, W., Han, L. (2015). Comparing machine learning classifiers for object-based land cover classification using very high-resolution imagery. Remote Sensing, 7(1), 153–168. https://doi.org/10.3390/rs70100153

Rahim, M. A. (2025). Geological field report on Cox's Bazar town and surrounding areas focusing on geomorphology, geology, georesources and geohazards (Technical Report). Department of Geology, University of Dhaka.

Rouse, J. W., Jr., Haas, R. H., Schell, J. A., Deering, D. W. (1973). Monitoring Vegetation Systems in the Great Plains with ERTS. In Symposium on Significant Results Obtained from the Earth Resources Technology Satellite-1 (ERTS-1) (NASA SP-327) (Vol. 1, pp. 309–317). National Aeronautics and Space Administration

Roy, B. (2021). A machine learning approach to monitoring and forecasting spatio-temporal dynamics of land cover in Cox's Bazar district, Bangladesh from 2001 to 2019. Environmental Challenges, 5, 100237. https://doi.org/10.1016/j.envc.2021.100237

Sakamoto, M., Ullah, S. M. A., Tani, M. (2021). Land cover changes after the massive Rohingya refugee influx in Bangladesh: Neo-classic unsupervised approach. Remote Sensing, 13(24), 5056. https://doi.org/10.3390/rs13245056

Sarkar, S. K., Saroar, M. M., Chakraborty, T. (2022). Cost of ecosystem service value due to Rohingya refugee influx in Bangladesh. Disaster Medicine and Public Health Preparedness. https://doi.org/10.1017/dmp.2022.125

Siddeqa, M., Islam, M. T., Hasan, M. F., Islam, R., Rasheduzzaman, M. (2023). Land use and land cover change detection of Teknaf Upazila due to Rohingya crisis by using GIS, and RS techniques. Asian Journal of Social Sciences and Legal Studies, 5(6), 246–252. https://doi.org/10.34104/ajssls.023.02460252

Sourav, A. P. (2025). Geological field report on the geology and coastal dynamics of Cox's Bazar (Technical Report). Department of Geology and Mining, University of Barishal.

Sun, J., Ongsomwang, S. (2023). Optimal parameters of random forest for land cover classification with suitable data type and dataset on Google Earth Engine. Frontiers in Earth Science, 11, 1188093. https://doi.org/10.3389/feart.2023.1188093

Talukdar, S., Singha, P., Mahato, S., Shahfahad, Pal, S., Liou, Y. A., Rahman, A. (2020). Land-use land-cover classification by machine learning classifiers for satellite observations-A review. Remote Sensing, 12(7), 1135. https://doi.org/10.3390/rs12071135

UNHCR Population Map. (2025). UNHCR, Bangladesh, Cox’s Bazar. UNHCR. Retrieved 16 August, 2025, from https://data2.unhcr.org/en/documents/details/70839

UNEP-WCMC, & IUCN. (2025). Protected Planet: The World Database on Protected Areas (WDPA) and the World Database on Other Effective Area-based Conservation Measures (WD-OECM) (December 2025 release). UNEP-WCMC and IUCN. https://www.protectedplanet.net

USGS (United States Geological Survey). (2018, July 16). USGS EROS archive – Sentinel-2: Mission overview and band specifications. https://www.usgs.gov/centers/eros/science/usgs-eros-archive-sentinel-2

Valdivieso-Ros, C., Alonso-Sarria, F., Gomariz-Castillo, F. (2021). Effect of different atmospheric correction algorithms on Sentinel-2 imagery classification accuracy in a semiarid Mediterranean area. Remote Sensing, 13(9), 1770. https://doi.org/10.3390/rs13091770

Xu, H. (2006). Modification of normalised difference water index (NDWI) to enhance open water features in remotely sensed imagery. International Journal of Remote Sensing, 27(14), 3025–3033. https://doi.org/10.1080/01431160600589179

Xue, J., Su, B. (2017). Significant remote sensing vegetation indices: A review of developments and applications. Journal of Sensors, 2017, 1353691. https://doi.org/10.1155/2017/1353691

Zha, Y., Gao, J., Ni, S. (2003). Use of normalized difference built-up index in automatically mapping urban areas from TM imagery. International Journal of Remote Sensing, 24(3), 583–594. https://doi.org/10.1080/01431160304987

Zhang, Z., Wei, M., Pu, D., He, G., Wang, G., Long, T. (2021). Assessment of annual composite images obtained by google earth engine for urban areas mapping using random forest. Remote Sensing, 13(4), 748. https://doi.org/10.3390/rs13040748

# Comparative Seasonality Assessment of Sentinel-1 SAR and Sentinel-2 MSI Satellite Data for Water Extent Area Mapping: A Case Study on Hakaluki Haor, Bangladesh

Sadid Khondokar Saykot[a], Md. Jahidul Ashik[b*], S. M. Ahsan Habib[b], Md. Nur Hossain Sharifee[b], Ahad Kanak Prottay[c], Abrar Jahin Ornob[c]

[a]*Research Fellow, Bangladesh Space Research and Remote Sensing Organization (SPARRSO), Agargaon, Sher-e-Bangla Nagar, Dhaka-1207, Bangladesh.*

[b]*Bangladesh Space Research and Remote Sensing Organization (SPARRSO), Agargaon, Sher-e-Bangla Nagar, Dhaka-1207, Bangladesh.*

[c]*Graduate Student, Urban and Rural Planning Discipline, Khulna University, Khulna.*

**Corresponding author: jahidul.ashik@sparrso.gov.bd (*Md. Jahidul Ashik*)*

**Article info**

***Keywords:***
*Synthetic Aperture Radar (SAR),*
*Multispectral Instrument (MSI),*
*Normalized Difference Water Index (NDWI),*
*Seasonal Variation*

**Article History:**
Received-07 Dec 2025
Revised-23 Jan 2026
Accepted-09 Feb 2026
Published- 31 March 2026

**DOI:**
https://doi.org/10.66268/jrse.2026.05.206008

**ABSTRACT**

Publicly available satellite imagery supports reliable waterbody extraction, which is crucial for hydrological studies, environmental monitoring, resource management, disaster management, urban heat reduction planning, etc. This study focuses on the extraction of inland waterbodies of Hakaluki Haor using Sentinel-1 and Sentinel-2 imagery and compares their results during the pre-monsoon (March) and post-monsoon (November) seasons from 2019 to 2024. The waterbodies were delineated using a threshold-based approach for Sentinel-1 and the Normalized Difference Water Index (NDWI) for Sentinel-2. The results reveal seasonal and inter-annual variability, with minimal pre-monsoon water observed in 2021–2022 and exceptionally high post-monsoon inundation in 2020, when Sentinel-2 detected approximately 122.4 km² compared to 95 km² of water extent from Sentinel-1. The analysis further shows that during the pre-monsoon season, waterbody extraction overlapping area between these two sensors varies from 63-91% due to scattered and fragmented waterbodies, whereas during post-monsoon, this variation is significantly reduced to 81-95%. It indicates that during post-monsoon, due to continuous waterbodies, the sensor choice has less effect on waterbody extraction in a similar context.

## 1. Introduction

Wetlands play a vital role in maintaining ecosystem services by regulating carbon dynamics as well as water and energy cycles (Tootchi et al., 2018). Understanding ecosystem processes in wetlands depends largely on the accurate measurement of surface water extent (Huang et al., 2018). Surveillance of inland water bodies represents a critically important area of study, as it supports the analysis of both natural and anthropogenic processes, especially those related to sustainability and risk mitigation (Valdiviezo-Navarro et al., 2019). For effective measurement and monitoring of waterbody dynamics, remote sensing is a modern and effective tool (Jiang et al., 2021). Now, different publicly available satellite images have made it easier and more cost-effective to monitor water bodies over the years using images with varying pixel sizes

(Buma et al., 2018). There are three primary ways available to observe the earth through satellite images-reflected solar radiation, active & passive microwave emission, and emitted thermal radiation (Mishra & Pant, 2020). Continuous monitoring of the Earth's surface is enabled by active remote sensors, such as synthetic aperture radar (SAR) systems, regardless of weather conditions, making them suitable for flood risk prediction and natural resource management (Valdiviezo-Navarro et al., 2019). Sentinel satellites offer reliable SAR and optical imagery, which are frequently used for the mapping of waterbodies (Jiang et al., 2021). Therefore, the accurate delineation of water areas can be conducted using publicly available satellite imagery. The Sentinel-1 provides datasets from a dual polarization C-band SAR instrument, which operates using active microwave sensors (Chen et al., 2021). Its advantages are that images can be acquired in all weather conditions, both day and night, by SAR sensors. This enables them to be used effectively for flood monitoring, mapping, and damage assessment (Pech-May et al., 2023).

Monitoring surface water is a significant focus within remote sensing, where waterbody extraction can be performed using three methods for SAR data: backscatter thresholding, random forest (RF) classification, and deep learning-based classification (Saghafi et al., 2021). An automated classification tree approach can be used to delineate surface water extent from Sentinel-1 SAR imagery, using training datasets generated from previously developed water-class masks (Huang et al., 2018). Also, an unsupervised method combining the local Moran index and morphological closing on Sentinel-1 data can be used to accurately extract inland waterbodies (Valdiviezo-Navarro et al., 2019). For this thresholding method is required, which is the most widely used approach for distinguishing water and non-water areas in SAR images (Liang & Liu, 2020). This method uses the principle where waterbodies exhibit low backscatter values while the surrounding terrain shows higher backscatter. The effectiveness of these detection algorithms depends on the land cover types and the topography of the area (Bioresita et al., 2019). On the other hand, high-resolution multispectral optical images like Sentinel-2 often have the presence of clouds, which can disrupt the observation of water bodies, by acquiring cloud-free images is quite impossible to acquire cloud-free images, especially in monsoon seasons (Pech-May et al., 2023). The use of water body indices, such as Normalized Difference Water Index (NDWI), Modified Normalized Difference Water Index (MNDWI), shows that Sentinel-2 imagery provides higher accuracy for water extraction than Landsat-8, particularly for delineating river features (Li et al., 2021). Also, the NDWI-based method enhances water features by exploiting differences in reflected green and near-infrared radiation, while minimizing the influence of soil and land vegetation (McFeeters, 1996). A key limitation of this approach is that, although non-water features are diminished, they are not eliminated from the image (McFeeters, 1996). Although Sentinel-2 provides blue, green, red, and near-infrared bands at a 10 m spatial resolution, the two short-wave infrared bands frequently used for water index generation are available at 20 m resolution, which partially constrains the precision of water extraction outcomes. Using only the green and near-infrared bands at 10 m resolution, the NDWI has been demonstrated to produce significant misclassification errors (Fisher et al., 2016; Li et al., 2021). In this study, the NDWI method was applied to Sentinel-2 imagery to delineate waterbodies of Hakaluki Haor.

Bangladesh boasts numerous rivers, lakes, wetlands, Haors, baors, jheels, and beels, with 373 Haors spanning districts like Sunamganj, Habiganj, Netrakona, Kishoreganj, Sylhet, Moulvibazar, and Brahmanbaria (Ullah, 2017). Wetlands cover about half the country's land, roughly 7-8 million hectares-with 7% permanently underwater, 21% facing deep flooding over 90 cm, and 35% experiencing shallow inundation; Hakaluki Haor stands out as one of the largest (Islam et al., 2018). Thus, continuous monitoring for the sustainability of this Haor is essential in obtaining the optimal value of it. But seasonality plays a crucial role in determining the extent of the water body, which also affects the biodiversity of this Haor. So, the extraction of water extent considering the seasonality for different satellite sensors in these bio-diversified Haor region can play a vital role in research and monitoring of natural resources. Local geography, diversity of seasonality, and weather factors might affect the different sensors' derived output for water body extraction. The objective of this study is to compare the active sensor of Sentinel-1 and the optical sensor of Sentinel-2 for water extent area delineation in Hakaluki Haor, emphasizing the seasonality patterns.

## 2. Materials and Methods

### 2.1 Study Area

Hakaluki Haor is the largest marsh wetland in Bangladesh and among the most significant wetland ecosystems in South-East Asia. The areas surrounding Hakaluki Haor are inhabited by approximately 190,000 people (Hossain, 2013; Ahmed et al., 2015). Hakaluki Haor is situated in the northeastern region of Bangladesh, extending between latitudes 24°35′N to 24°45′N and longitudes 92°00′E to 92°08′E (Fig. 1). Bangladesh's tropical monsoon climate shows seasonal variations in temperature and precipitation, which divide the year into four main seasons: pre-monsoon, monsoon, post-monsoon, and winter (Dastour et al., 2025; Islam et al., 2025; Small, 2011). The pre-monsoon season, occurring from March to May, is defined as the transitional period leading up to the onset of the summer monsoon. It is generally the hottest time of the year in Bangladesh, when temperatures commonly range between 30 °C to 40 °C and are frequently accompanied by intense thunderstorms (Dastour et al., 2025; Islam et al., 2025). The post-monsoon period, spanning October to November, is defined as the transitional phase that occurs after the withdrawal of the monsoon rains. This season is typically drier than the preceding months. It is then followed by the winter season from December to February, which brings comparatively cooler conditions, with temperatures generally ranging between 15 °C to 25 °C (Islam et al., 2025). Recognizing that the hottest and driest months play a crucial role in shaping agricultural activities, managing water resources, and informing climate adaptation measures, this study selects March to represent the pre-monsoon season and November to represent the post-monsoon season. These two months exhibit the greatest variation in waterbodies within Hakaluki Haor, making them ideal for focused study in the Bangladesh context. They were specifically selected because Sentinel-2 satellite imagery for these months provides clear images with significantly lower cloud coverage, allowing for more accurate analysis.

Protection and improvement of water quality, provision of safe habitats for fish and wildlife, storage of floodwaters, and maintenance of surface water flow during dry periods are considered the major functions of this wetland (Islam et al., 2018). All the characteristics and functions of a typical wetland are exhibited by Hakaluki Haor, and for this reason, nationwide recognition has been achieved as an Ecologically Critical Area (ECA) and recognized as one of the Ramsar sites of international importance for the conservation and sustainable utilization of wetlands ( Hossain, 2013; Ahmed et al., 2015). Due to its socio-economic importance and environmental significance, it has been selected as the study area.

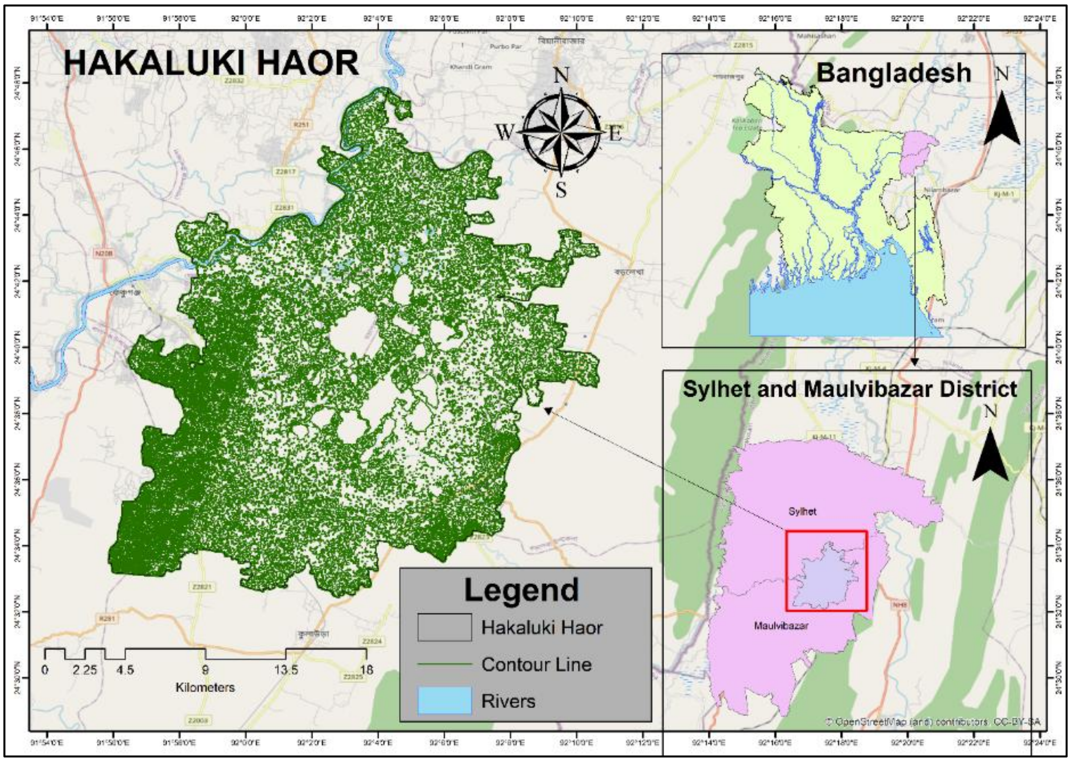


**Fig. 1:** Map of the study area showing the regional settings and the area of interest

## 2.2 Satellite data acquisition

Sentinel-1 Synthetic Aperture Radar (SAR) and Sentinel-2 Multispectral Instrument (MSI) imagery were collected to ensure accurate and seasonally consistent waterbody delineation for the period 2019–2024. Table 1 summarizes the characteristics and acquisition details of the satellite datasets used in this study. Sentinel-1 C-band SAR data, with a spatial resolution of 10 m, were acquired from the COPERNICUS/S1_GRD collection and processed using the cloud-based remote sensing platform GEE. Image compositing is performed by assembling a time series of images acquired within a user-defined period during the pre- and post-monsoon seasons and deriving per-pixel mean values from the aggregated dataset for waterbody extraction (Howe et al., 2022). The study utilizes data from both Sentinel-1A and Sentinel-1B satellites, which operate in the Interferometric Wide Swath (IW) mode to ensure broad area coverage. The images were captured in dual-polarization (VV & VH), enhancing the ability to distinguish between water bodies and other land cover types. With a spatial resolution of 10 m, the dataset provides detailed insights into water extent variations over time. To capture representative seasonal hydrological conditions, imagery was specifically selected for March and November, corresponding to the pre-monsoon and post-monsoon period, respectively. For each year, all Sentinel-1 acquisitions within the periods 1-31 March and 1-30 November were aggregated in GEE to produce monthly mean backscatter composites representing pre- and post-monsoon water conditions. This compositing approach reduces the influence of short-term anomalies, speckle noise, and scene-specific acquisition effects, while preserving stable water signatures at the monthly scale. Sentinel-2A surface reflectance data is obtained from the "COPERNICUS/S2_SR" collection, provides 10-meter multispectral observations and was filtered using a cloud-cover threshold of less than 5%. March was used to characterize the pre-monsoon condition due to typically clear skies, while November was selected for the post-monsoon period. In this study, an image compositing approach was implemented within the cloud-based remote sensing platform GEE to efficiently process multi-temporal Sentinel imagery and generate monthly mean composites for consistent waterbody delineation. For each year, all available Sentinel-2 acquisitions within the periods 1-31 March and 1-30 November were aggregated in GEE to generate monthly mean composites, providing consistent and seasonally representative imagery for pre- and post-monsoon waterbody delineation.

**Table 1.** Summary of satellite datasets used

| Satellite & sensor | Data acquisition (2019-2024) | Data type | Cloud cover (%) | Resolution (m) |
|---|---|---|---|---|
| Sentinel-1 (C-band SAR) | 1-30 November | Mean composite of SAR backscatter (VV/VH) | Not applicable | 10 |
| Sentinel-2A (MSI) | 1-31 March | Mean composite (optical reflectance) | <5 | 10 |

### 2.3 Data processing

For each study year, mean composite images were generated after several preprocessing steps to ensure accurate extraction of water extent. In Sentinel-1 imagery, at first, radiometric calibration is applied to convert raw SAR backscatter values into sigma nought ($\sigma^0$), making the measurements physically meaningful and comparable across different acquisition dates (Small, 2011). Since SAR images are inherently affected by speckle noise due to the coherent radar signal, speckle filtering is performed using adaptive filters such as the Lee filter, which reduces noise while preserving important spatial features for flood detection (Lee, 1980). Next, geometric correction, including terrain correction, is conducted to align the SAR imagery with a standardized coordinate system and remove distortions caused by terrain variations (Small, 2011). Considering the distinctive backscatter characteristics of water surfaces, a dual-polarization approach was adopted by integrating both VV (vertical–vertical) and VH (vertical–horizontal) polarization bands to enhance the accuracy of water body detection. The use of dual-polarization data allowed for better differentiation between water areas and other low-backscatter features such as wet soil or vegetation. A mean composite approach was applied to the Sentinel-2 imagery to remove high outlier pixels caused by clouds and cloud shadows. Cloud masking was performed as an essential pre-processing step to ensure accurate waterbody extraction using remote sensing images. In Sentinel-2 imagery, waterbodies were classified using NDWI values, where pixels with NDWI greater than 0 were considered waterbodies and those with NDWI less than or equal to 0 were classified as non-waterbodies. In this study, surface reflectance images from Sentinel-2 MSI Level-2A (SR) were used to extract the Green band (B3) and Near-Infrared band (B8) for NDWI calculation, enabling accurate identification of water bodies.

## 2.4 Methodology

For this study, Sentinel-1 SAR and Sentinel-2 MSI datasets were used to delineate water extent in Hakaluki Haor and to evaluate the comparative performance of active and optical sensors. Waterbody extraction was conducted separately for both sensors. Waterbody extraction was carried out using a threshold-based classification approach, where pixels exhibiting VV backscatter values lower than -17 dB were classified as water. This threshold was determined through trial-and-error specifically for the study area with image histograms analysis, which are often visually examined to determine threshold values and might vary (Martinis et al., 2015) Current research provides scarce methodological solutions for deriving water-related thresholds through statistical analysis of images (Martinis et al., 2015). Water surfaces typically produce low backscatter values in SAR imagery due to specular reflection, making thresholding techniques particularly effective for water detection. Owing to their methodological simplicity and computational efficiency, such approaches are widely used for SAR-based water extraction. To automate the classification process and determine an optimal threshold, Otsu's thresholding method was applied, which minimizes intra-class variance between water and non-water pixels based on the distinctive backscatter characteristics of water surfaces (Fig. 2).

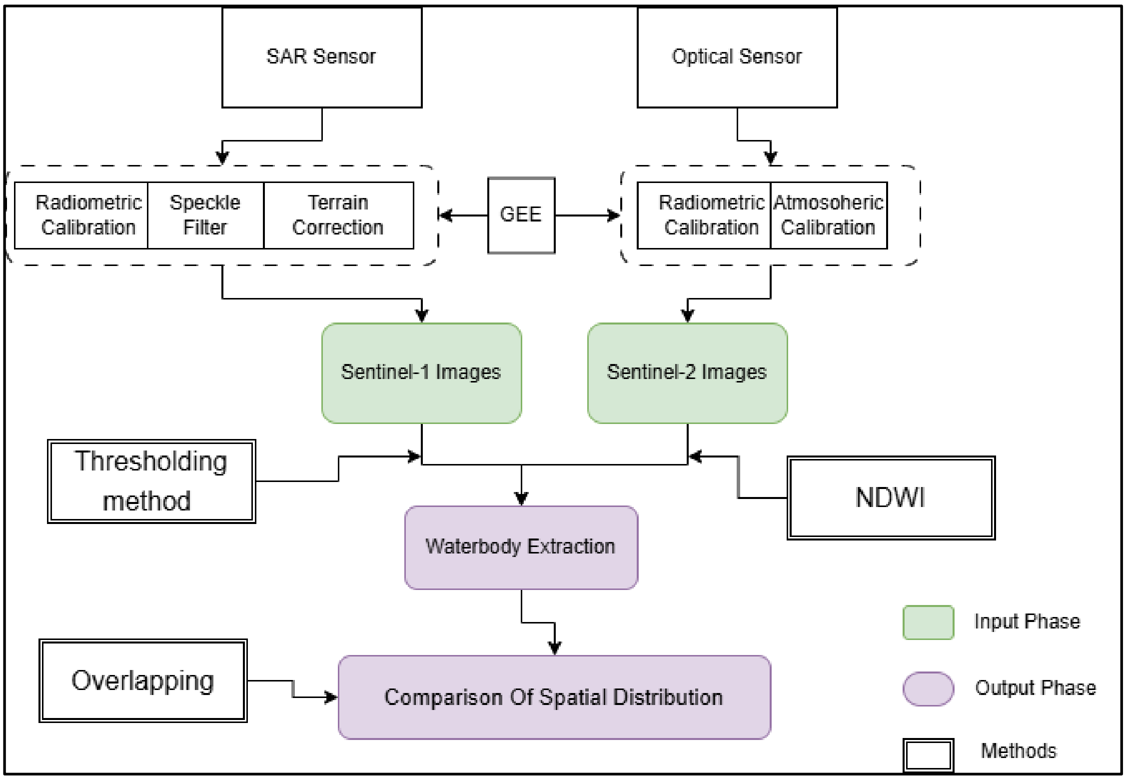


**Fig. 2:** Methodological workflow of the study

In parallel, waterbodies were extracted from Sentinel-2 imagery using the NDWI, calculated according to Equation (1). Pixels with positive NDWI values (NDWI > 0) were classified as water, as these values indicate a higher reflectance in the green band relative to the near-infrared band, a characteristic feature of open water surfaces. Finally, a spatial comparison was performed using the Intersect tool in ArcGIS 10.7.1 to identify overlapping waterbodies detected by both SAR and optical datasets. This analysis facilitated the evaluation of differences in water detection capability, seasonal sensitivity, and the overall suitability of SAR and optical sensors for waterbody mapping in the study area. Furthermore, it enabled an assessment of the degree of spatial agreement between the two sensors, thereby supporting the fulfilment of the study's final objective.

$$\text{NDWI}=\frac{(\text{Green} - \text{NIR})}{(\text{Green} + \text{NIR})} \ldots\ldots\ldots \; (1)$$

## 3. Results

### 3.1 Delineation of waterbody

The analysis of water dynamics during the period 2019-2024 shows clear variations in the seasons and inter-annual changes as obtained by both Sentinel-1 and Sentinel-2 images. The Sentinel-1 SAR and Sentinel-2 optical satellite data show the low water levels in March (Fig. a3 and Fig. c3) with permanent water features remaining despite drier conditions. The lower extent for 2021-2022 and greater extent for 2019-2024 matches Fig. 4, where the Sentinel-1 data indicates low levels of water below 60 km² in 2021-2022 and higher levels of approximately 110 km² in 2019 and 2024, as indicated by Sentinel-2 data. This is because SAR data can penetrate clouds and vegetation to indicate low water levels, while optical satellite data indicates clear conditions using NDWI indices.

The satellite images of November in Fig. 3(b) and Fig. 3(d) from both Sentinel-1 and Sentinel-2 sensors show maximum inundation with extensive water coverage much larger than that of the pre-monsoon season. The smaller extent in 2021-2022 is maintained in both, indicating drier conditions during the post-monsoon periods, while in other years, the area is larger; 2022 is the lowest point of the year for both. SAR backscatter can differentiate even the smooth water areas under vegetation, matching optical reflectance. A study shows that in 2022, global temperatures continued to rise, following the planet's long-term warming trend. Global temperatures that year were 1.6 °F (0.89 °C) above the 1951–1980 baseline (NASA, 2022) . The NASA further indicated that 2022 was one of the sixth-warmest years on record since 1880, reflecting unusually high global surface temperatures (NASA, 2022). The unusually high temperatures likely accelerated evaporation and might have reduced surface water retention, explaining the observed minimum low water coverage in 2022. These changes reflect inter-annual variability in post-monsoon inundation, with some years having extensive surface water in the Haor, while others have relatively less. However, the post-monsoon period always marks the peak phase of inundation for all years, with extensive water accumulation in the low-lying areas of the Haor.

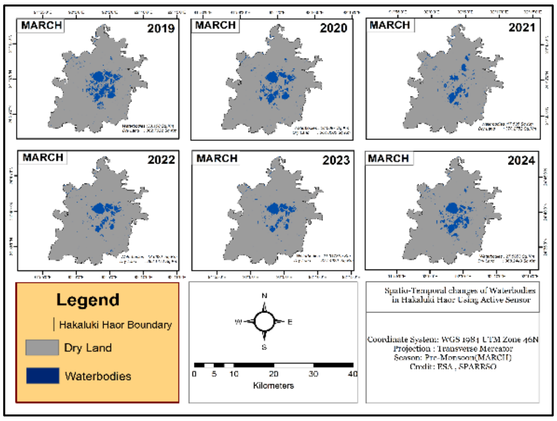


a) Pre-Monsoon (Sentinel-1)

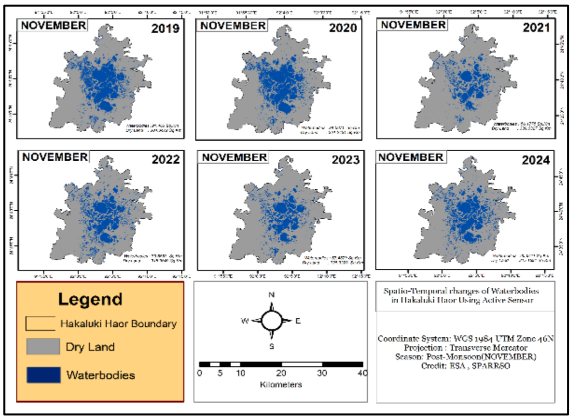


b) Post-Monsoon (Sentinel-1)

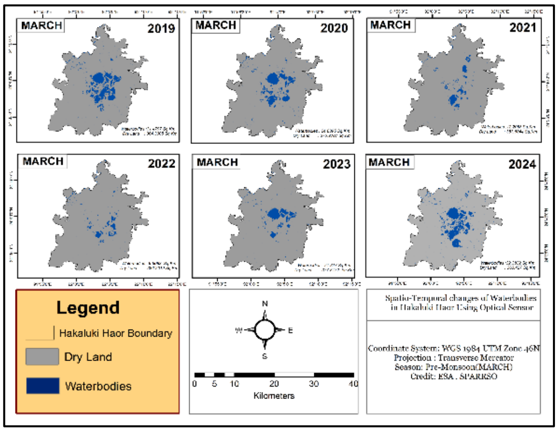


c) Pre-Monsoon (Sentinel-2)

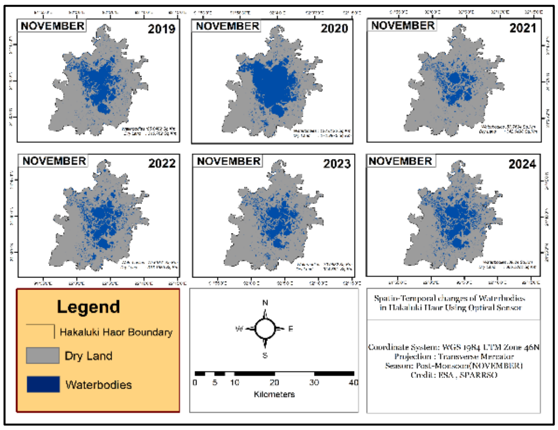


d) Post-Monsoon (Sentinel-2)

**Fig. 3.** Pre- and post-monsoon waterbody extraction from Sentinel-1 and Sentinel-2

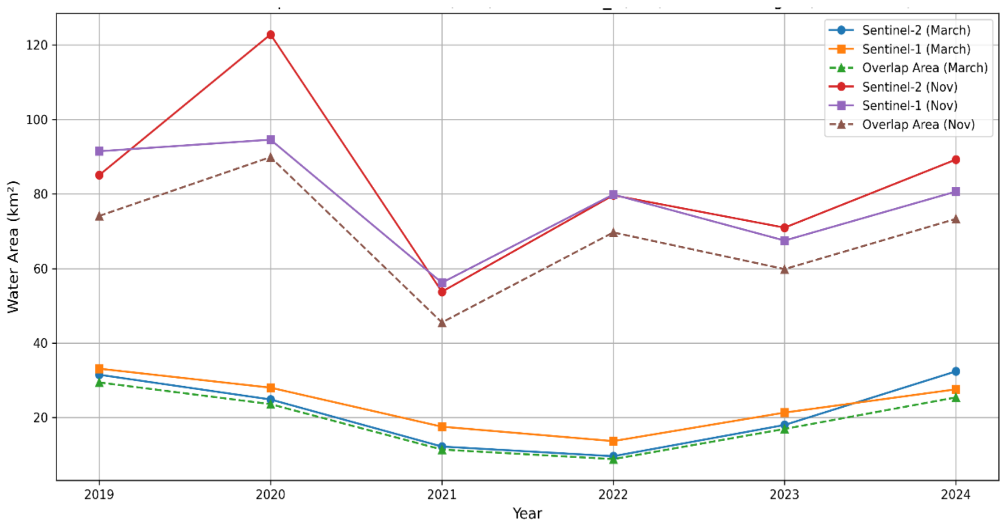


**Fig. 4**. Sensor-driven water extent area comparison of Sentinel 1 and Sentinel 2 (2019-2024)

### 3.2 Comparative assessment of delineated water area

Table 2 shows the overlapping of water extent between Sentinel-1 and Sentinel-2 images during the pre-monsoon (March) and post-monsoon (November) seasons from 2019 to 2024. It is lowest in 2021 and 2022, which is 64.45% and 63.87%, respectively. In contrast, the remaining years show consistently high overlap values, exceeding 78–91%, which shows a stronger level of consistency between the optical and SAR datasets. During the post-monsoon season, the overlap shows higher values across all years, ranging from 80.98% to 95.03% within 2019-2024, which can be observed as a result of extensive and unified water coverage after monsoon flooding. On the other hand, during the pre-monsoon period, the overall area detected by Sentinel-1 and Sentinel-2 is similar, but the overlapping is 63-91%, which is less than the post-monsoon period. The observed reason is that in the post-monsoon (November) period, when the water bodies are more continuous, whereas in the case of pre-monsoon (March), it is less continuous.

**Table 2.** Overlapping area assessment of Sentinel-2 with respect to Sentinel-1

| Year | Overlapping area of water extent (%) | |
|---|---|---|
| | Pre-monsoon (March) | Post-monsoon (November) |
| 2019 | 88.60 | 80.97 |
| 2020 | 83.80 | 95.03 |
| 2021 | 64.45 | 81.05 |
| 2022 | 63.86 | 87.41 |
| 2023 | 78.82 | 88.69 |
| 2024 | 91.73 | 91.03 |

## 4. Discussion

Analysis of water dynamics in Hakaluki Haor from 2019 to 2024 shows significant seasonal and inter-annual variations. Water extent reaches its minimum in March and peaks in November, showing the natural hydrological cycle of Haor, where monsoon precipitation and runoff drive maximum inundation. Sentinel-1 SAR and Sentinel-2 optical imagery exhibit strong concordance, with overlap ranging from 63–91% in pre-monsoon periods and 81–95% in post-monsoon periods. The reduced overlap in 2021 and 2022 (approximately 64%) aligns with the smaller water extent area during that time period, which suggests that drier conditions can be attributed to the diversified overall results. This type of seasonal variability highlights the importance of considering temporal dynamics when selecting a sensor for assessing wetland water availability and planning for resource management.

However, the waterbody extraction from Sentinel-1 SAR relied on a thresholding approach determined through trial and error, which is quite simplistic, and the results might be impacted by the selected images' noise, backscatter variations, and seasonal changes in surface conditions. Therefore, selecting an appropriate threshold requires subjective adjustment for each image, which can introduce inconsistencies across time and reduce reproducibility. Consequently, extreme water levels or mixed land-water pixels may be misclassified, affecting the accuracy of the derived water extent. Hence, in-depth pixel-based analysis before the selection of the threshold is recommended for the mapping of water extent with rigorous field-based approaches. Besides, this study is limited by the field validation, which might affect the estimation of the water body extent from the selected threshold. Nevertheless, despite these limitations, comparing SAR and optical datasets enhances waterbody mapping accuracy, as SAR penetrates vegetation and cloud cover, while optical imagery excels under clear-sky conditions. This multi-sensor fusion enables robust, seasonally resolved monitoring of wetland dynamics. The findings emphasize the necessity of accounting for both seasonal timing and inter-annual fluctuations to reliably quantify water extent, with implications for wetland conservation and hydrological modeling. Seasonal timing, sensor complementarity, and inter-annual variability must be considered to ensure accurate representation of water dynamics and support informed decision-making in wetland management and climate adaptation strategies.

## 5. Conclusions

The difference in consistency of overlapping and total water area extent indicates that the selection of sensors between these two satellites will not affect the result much for the post-monsoon season, while it might affect the pre-monsoon period, as waterbodies remain highly scattered and fragmented. Conversely, in the post-monsoon season, the influence of monsoonal rainfall leads to widespread inundation and the expansion of continuous water surfaces. Under these conditions, both Sentinel-2 and Sentinel-1 capture the extended waterbodies more accurately. For seasonal variation, the results are highly impacted by the amount of rainfall or seasonal anomaly. The current study used conventional threshold backscatter for Sentinel-1 and NDWI for Sentinel-2 from the expert judgement, which might affect the accuracy of waterbody extraction. Future studies are recommended to incorporate advanced techniques to improve waterbody delineation for seasonal variations of Haor wetlands. These types of time series seasonal monitoring might be effective for understanding these effects on local climate and water storage pattern analysis. Also, the selection of sensors depending on the seasonality can affect the analysis, which is portrayed in this study.

## Acknowledgments

No funding for this study was available. We want to thank the Bangladesh Space Research and Remote Sensing Organization (SPARRSO) for providing guidance and lab facilities.

## Data availability

The data will be made available upon request to the corresponding author.

## Conflict of interest

The authors declare that there is no conflict of interest regarding the publication of this paper.

## References

Ahmed, Z., Alam, M., Rahman, S., Ahmed, S., Hoque, M., Meem, R. (2015). An integrated environmental assessment of Hakaluki Haor ecosystem using DPSIR framework: A case study on Moulovibazar District of Bangladesh. American Research Thoughts, 1, 1631-1650. https://doi.org/10.6084/M9.FIGSHARE.1399082

Bioresita, F., Puissant, A., Stumpf, A., Malet, J. P. (2019). Fusion of Sentinel-1 and Sentinel-2 image time series for permanent and temporary surface water mapping. International Journal of Remote Sensing. https://doi.org/10.1080/01431161.2019.1624869

Buma, W. G., Lee, S.-I., Seo, J. Y. (2018). Recent Surface Water Extent of Lake Chad from Multispectral Sensors and GRACE. Sensors, 18(7), 2082. https://www.mdpi.com/1424-8220/18/7/2082

Chen, S., Huang, W., Chen, Y., Feng, M. (2021). An adaptive thresholding approach toward rapid flood coverage extraction from Sentinel-1 SAR imagery. Remote Sensing, 13(23), 4899. https://www.mdpi.com/2072-4292/13/23/4899

Dastour, H., Alam, M. M., Dewan, A., Hassan, Q. K. (2025). Evaluating climatic warming and the modulating effects of surface water and regional variables in western Bangladesh. Results in Engineering, 25, 103864. https://doi.org/https://doi.org/10.1016/j.rineng.2024.103864

Fisher, A., Flood, N., Danaher, T. (2016). Comparing Landsat water index methods for automated water classification in eastern Australia. Remote sensing of environment, 175, 167-182. https://doi.org/https://doi.org/10.1016/j.rse.2015.12.055

Hossain, M. S. (2013). Climate change affects wetland resources in Bangladesh: A case study on Hakaluki Haor. Scientific Research Journal, 10(1), 37-63. https://doi.org/10.24191/srj.v10i1.5406

Howe, A. A., Parks, S. A., Harvey, B. J., Saberi, S. J., Lutz, J. A., Yocom, L. L. (2022). Comparing Sentinel-2 and Landsat 8 for burn severity mapping in western North America. Remote Sensing, 14(20), 5249. https://www.mdpi.com/2072-4292/14/20/5249

Huang, W., DeVries, B., Huang, C., Lang, M. W., Jones, J. W., Creed, I. F., Carroll, M. L. (2018). Automated extraction of surface water extent from Sentinel-1 data. Remote Sensing, 10(5), 797. https://www.mdpi.com/2072-4292/10/5/797

Islam, M. N., Rakib, M., Sufian, M., Sharif, A. (2018). Detection of climate change impacts on the Hakaluki Haor wetland in Bangladesh by use of remote sensing and GIS. In (pp. 195-214). https://doi.org/10.1007/978-3-319-26357-1_8

Islam, M. T., Das, N., Islam, M. D., Joy, M., Khatun, M. R., Jahan, N., Islam, N., Islam, M. M., Roy, S., Adham, A. K. M. (2025). Integrated GIS, statistical modeling, and CMIP6-based assessment of groundwater irrigation quality in north-central Bangladesh for sustainable management. Results in Engineering, 27, 106496. https://doi.org/10.1016/j.rineng.2025.106496

Jiang, H., Wang, M., Hu, H., Xu, J. (2021). Evaluating the performance of Sentinel-1A and Sentinel-2 in small waterbody mapping over urban and mountainous regions. Water, 13(7), 945. https://www.mdpi.com/2073-4441/13/7/945

Lee, J. S. (1980). Digital image enhancement and noise filtering by use of local statistics. IEEE Transactions on Pattern Analysis and Machine Intelligence, PAMI-2(2), 165-168. https://doi.org/10.1109/TPAMI.1980.4766994

Li, J., Peng, B., Wei, Y., Ye, H. (2021). Accurate extraction of surface water in complex environment based on Google Earth Engine and Sentinel-2. PloS one, 16(6), e0253209. https://doi.org/10.1371/journal.pone.0253209

Liang, J., Liu, D. (2020). A local thresholding approach to flood water delineation using Sentinel-1 SAR imagery. ISPRS journal of photogrammetry and remote sensing, 159, 53-62. https://doi.org/10.1016/j.isprsjprs.2019.10.017

Martinis, S., Kersten, J., Twele, A. (2015). A fully automated TerraSAR-X based flood service. ISPRS journal of photogrammetry and remote sensing, 104, 203-212. https://doi.org/https://doi.org/10.1016/j.isprsjprs.2014.07.014

McFeeters, S. K. (1996). The use of the Normalized Difference Water Index (NDWI) in the delineation of open water features. International Journal of Remote Sensing, 17(7), 1425-1432. https://doi.org/10.1080/01431169608948714

Mishra, V., Pant, T. (2020). Open surface water index: a novel approach for surface water mapping and extraction using multispectral and multisensory data. Remote Sensing Letters, 11, 973-982. https://doi.org/10.1080/2150704X.2020.1804085

NASA. (2022). A look back: 2022's temperature record [Video] YouTube. https://www.youtube.com/watch?v=gxxmigcffn4

Pech-May, F., Aquino-Santos, R., Delgadillo-Partida, J. (2023). Sentinel-1 SAR images and deep learning for water body mapping. Remote Sensing, 15(12), 3009. https://www.mdpi.com/2072-4292/15/12/3009

Saghafi, M., Ahmadi, A., Bigdeli, B. (2021). Sentinel-1 and Sentinel-2 data fusion system for surface water extraction. Journal of Applied Remote Sensing, 15. https://doi.org/10.1117/1.JRS.15.014521

Small, D. (2011). Flattening gamma: Radiometric terrain correction for SAR imagery. IEEE Transactions on Geoscience and Remote Sensing, 49(8), 3081-3093. https://doi.org/10.1109/TGRS.2011.2120616

Tootchi, A., Jost, A., Ducharne, A. (2018). Multi-source global wetland maps combining surface water imagery and groundwater constraints PANGAEA. https://doi.org/10.1594/PANGAEA.892657

Ullah, M. (2017). Water bodies delineation and change detection using GIS and remote sensing with multitemporal Landsat imagery: A case study of Tanguar Haor. 59, 2017.

Valdiviezo-Navarro, J. C., Salazar-Garibay, A., Téllez-Quiñones, A., Orozco-del-Castillo, M., López-Caloca, A. A. (2019). Inland water body extraction in complex reliefs from Sentinel-1 satellite data. Journal of Applied Remote Sensing, 13, 016524. https://doi.org/10.1117/1.Jrs.13.016524

# Evaluating Urban Expansion and Population Growth Efficiency Using Sustainable Development Goal Indicators in the Lower Turag River Basin, Bangladesh

Maria Binta Malek[a], Md. Mahmudul Hasan Shahed[a], Khaled Jubair Shabab[a], Rezaul Roni[b], Md Shahedur Rashid[b]

[a*]*Graduate student, Department of Geography and Environment, Faculty of Social Sciences, Jahangirnagar University, Savar, Dhaka-1342, Bangladesh.*

[b*]*Department of Geography and Environment, Faculty of Social Sciences, Jahangirnagar University, Savar, Dhaka-1342, Bangladesh.*

**Corresponding author:* maria.ju.aldc@gmail.com *(Maria Binta Malek)*

**Article info**

***Keywords:***
*Land Use Land Cover,*
*Urban Expansion,*
*Land Consumption Rate,*
*Population Growth Rate,*
*Urban Sustainability*

**Article History:**
Received-18 Dec 2025
Revised-06 March 2026
Accepted-24 March 2026
Published-31 March 2026

**DOI:**
https://doi.org/10.66268/jrse.2026.05.442627

**ABSTRACT**

Understanding the spatiotemporal dynamics of Land Use and Land Cover (LULC), caused by rapid urbanization, is crucial to mitigating the negative impacts of urban growth, threatening agricultural sustainability and ecological balance. This research was conducted on the Lower Turag River Basin in the northwestern region of Dhaka, Bangladesh and aims to quantify the built-up area changes along with population changes from 2001 to 2021, evaluating the nature of urban expansion by calculating the ratio between Land Consumption Rate and Population Growth Rate (LCRPGR) following the Sustainable Development Goal (SDG) metadata used for the indicator 11.3.1. Here, satellite imagery, including Landsat 5, Landsat 8, and Shuttle Radar Topography Mission (SRTM) data, was used in the Google Earth Engine (GEE) platform, where the Random Forest algorithm was incorporated to classify LULC into five distinct categories. The high kappa values (>0.87) ensured the accuracy and the reliability of the classification. The results show that built-up areas increased by 139.39%, while the total population grew by 163.71% between 2001 and 2021, largely replacing agricultural land and natural vegetation. The urban expansion outpaced population growth, with a land consumption to population growth ratio of 1.775 for the period of 2001 to 2011 and 0.513 for the period of 2011 to 2021, indicating critical urban expansion. Besides, the LULC patterns found that the expansion occurred towards the north of the Turag basin with high growth of population, which increased the land consumption. Furthermore, the findings of this study will help policymakers and researchers to understand the spatio-temporal changes of urban expansion, population growth, and land consumption with a sustainable policy framework.

## 1. Introduction

The urban footprint development is a complex phenomenon that occurs due to the interplay of demographic, economic, social, and political factors, and it is an important aspect of determining the changes in the Land Use and Land Cover (LULC) on a global scale (Mosammam et al., 2017). As demographics predict, by the year 2050, almost seven out of ten people will be living in cities (United Nations, 2019), which as shown will cause rapid urbanization, mainly in the developing world (Melchiorri et al., 2018). Urbanization processes are influenced by the natural increase of population and migration of people towards urban incorporation and transformation of rural areas into urban ones, that are more rapid in the developing countries than the developed ones, which is alarming for sustainable urbanization (Rahman et al., 2023).

Dhaka is one of the fastest-growing cities, where the constant transformation of farmland, wetlands, and water bodies into urban locations has reduced green and blue areas and made the city prone to flooding, waterlogging, and overall ecological collapse (Moniruzzaman et al., 2020; Mortoja & Yigitcanlar, 2020; Abbasi et al., 2022). The Lower Turag Basin, located on the peri-urban boundary of Dhaka, has undergone a rapid increase in population, expansion of settlements and an intensification of industrialization, which has resulted in the degradation of the freshwater ecosystem and environmental stress (Ghazaryan et al., 2021). It is important to understand the scale, trend, and effectiveness of the urban growth in this basin that can help in determining whether it is sustainable in the long run. In many countries, urban land use has historically outpaced population growth multiple times (three to five), and it is often called inefficient and unsustainable (Wiatkowska et al., 2021). This difference highlights the value of Sustainable Development Goal (SDG) Indicator 11.3.1, which assesses the efficiency of urban land-use by the ratio of the Land Consumption Rate to the Population Growth Rate (LCRPGR) (Melchiorri et al., 2019; Teklemariam, 2022). Geographic Information Systems (GIS) and remote sensing offer a powerful method of tracking these dynamics along with multi-temporal LULC changing patterns and correlating them with demographic data (Aghlmand & Kaplan, 2021; Kelly-Fair et al., 2022). This has been enhanced with the creation of Google Earth Engine (GEE), which enables scalable cloud-based processing of large datasets of satellites through which the transformation of landscapes through land can be rapidly and reproducibly analyzed (Huq & Rahman, 2022). The use of GEE in analyzing urban changes in specific areas of study makes it easier to identify the change in the land cover because of the growth of urbanization, hence its effect on the environment, like water shortage and pollution. For example, the urbanization process in Dhaka has created strong links with changes in land cover that have led to reduced green spaces and increased runoff that worsens the overall water management problem (Mundi, 2019).

The theoretical basis of this research relies on the connection among population growth, consumption of land, and LULC transition. As the growth of the population increases, the demand for housing, industry, transport, and services also increases, thus built-up areas expand, which often replaces the croplands, vegetation, and natural surfaces. SDG Indicator 11.3.1 offers an internationally accepted and uniform measure to determine whether the amount of land consumed is increasing at a faster rate than population growth, and thus it can be directly used to measure urban sustainability. Despite extensive work on Dhaka's urbanization, flooding, environmental degradation, and general land cover change, the Lower Turag Basin remains understudied as a socio-ecological system. Limited or no prior research has quantified land-use efficiency in this basin with respect to SDG 11.3.1. Existing studies do not integrate grid-based population disaggregation with multi-temporal built-up mapping, nor do they employ GEE-based LULC analysis aligned with UN-Habitat methodologies for SDG monitoring. This creates a crucial research gap about the rate at which the Lower Turag Basin's fertile land is being consumed in comparison with its population strains; such understanding is vital in sustainable planning and control.

Considering these research gaps, the current research combines multi-decadal LULC mapping with population disaggregation and SDG-consistent LCRPGR evaluation to analyze the efficiency of land-use in the Lower Turag Basin. In particular, the study will (a) quantify spatio-temporal LULC changes from 2001 to 2021 using satellite imagery and Random Forest classification in GEE and (b) assess the land consumption to population growth ratio (LCRPGR) to assess the sustainability of urban expansion in accordance with SDG Indicator 11.3.1. In such a comprehensive way, the research will offer an in-depth evaluation of the interaction between land and population dynamics within one of the fastest-developing peri-urban basins in Dhaka, Bangladesh.

## 2. Materials and Methods

### 2.1 Description of the study area

The study area is the lower part of the Turag Basin, most of which falls into the Northwestern part of Dhaka city, and a small portion of it also falls into the Gazipur district. Both districts are part of the Dhaka division, the central part as well as the capital of the country of Bangladesh, and their absolute location extends from 24°0'20.51"N to 23°45'38.20"N latitude and 90°14'48.72"E to 90°24'48.65"E longitude (Fig. 1). The Bangshi River is the upper tributary of the Turag River (Alam, 2003) and forms at the foot of the Madhupur tract. It is a tide-influenced river that passes through the north-west and north of Dhaka City (Choudhury & Choudhury, 2004). After passing through the west of Gazipur City Corporation (GCC) and Dhaka North City Corporation (DNCC), the Turag River falls into the Buriganga River (Alam, 2003). It joins the Buriganga at Mirpur in Dhaka district. The Turag River connects with the Balu River through the Tongi Khal (Uddin, 2005). The entire basin of the Turag represents a semi-funnel shape, and the catchment is situated in the central and southern region of the Madhupur tract, and the river flows from north to south throughout the basin (Pour and Oja, 2021).

The SRTM Digital Elevation Model (DEM) of the study area reveals the basin's highest elevation, which is at about 55 meters and is located significantly in the southwestern and northern regions (Fig. 1). On the contrary, the lowest elevation is predominantly concentrated in the central part encompassing the main river channel. The total area of the Turag River is about 631 sq.km (Uddin, 2005). Here, the Lower Turag River basin is considered from the Kodda Bridge in Tangail to the confluence of the Turag and Buriganga rivers. This portion covers roughly a total area of 252 sq.km, which includes 11 Unions having 88 Mauzas and 42 Wards comprising 199 Mauzas.

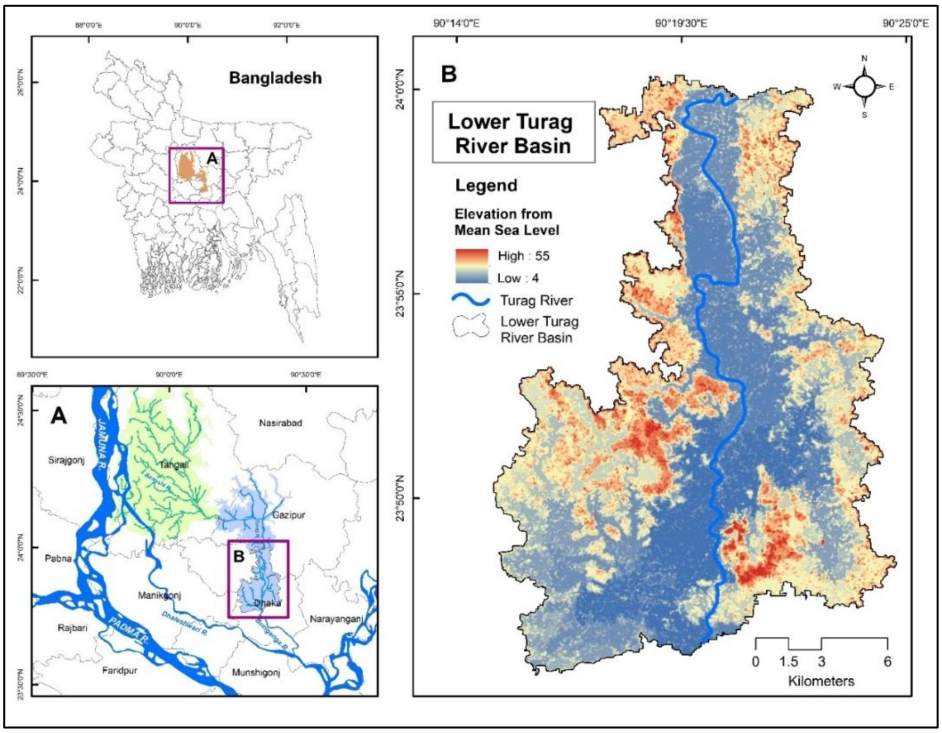


**Fig. 1.** Map of the study area showing the topographic information derived from SRTM DEM

## 2.2 Data acquisition

Remote sensing can effectively capture spatial and temporal dynamics of urban expansion, providing detailed insights into land consumption patterns (Jahan et al., 2021; Cuypers et al., 2023). Landsat imagery, generally having 30 m resolution and freely available data over a large period of time, is efficient to track urban growth, demonstrating how LULC modeling can forecast future urbanization scenarios, which is vital for sustainable land management (Amani et al., 2020). The GEE facilitates the processing of large datasets, such as those from Landsat and Sentinel satellites, making it an ideal environment for remote sensing applications, including LULC classification (Mutanga & Kumar, 2019; Tabunshchik et al., 2023). The study was purposely commenced from 2001 to 2021, as it aligns with the population data from the census survey, namely 'Population and Housing Census', held under the Bangladesh Bureau of Statistics (BBS) at an interval of 10 years. The first census after the Liberation War was in 1974 instead of 1971 due to the War, followed by 1981, 1991, 2001, 2011, and 2022 (scheduled for 2021, but delayed one year due to Covid 19) (Census, 2023).

For this study, we extensively used population data from the Census 2001, 2011 and 2022. Alongside, multispectral satellite imagery was imported into the GEE platform from the archives to analyze LULC changes in the study area over 20 years. Hence, both the Landsat 5 Thematic Mapper (TM) and Landsat 8 Operational Land Imager (OLI), Collection 2 Tier 1 calibrated top-of-atmosphere (TOA) reflectance data from USGS/GEE archive were used to produce the LULC map. Landsat 5 TM imagery was used for the earlier period, while Landsat 8 OLI imagery was used for the later period. To minimize the influence of seasonal variation and cloud contamination, images from the dry season (November–December) were selected. For each reference year (2001, 2011, and 2021), a temporal composite was generated in GEE using cloud-masked scenes within the selected date range. Cloud and shadow pixels were removed using the Landsat quality assessment (QA) band, and a median composite was produced to generate a representative cloud-free image for classification. All images have a spatial resolution of 30 m and were processed within the GEE platform for further analysis. The post-monsoon period in Bangladesh is characterized by reduced cloud cover, lower atmospheric moisture, and stabilized land surface conditions following monsoon recession. Selecting a uniform seasonal window enhances spectral separability of land cover classes and ensures reliable multi-temporal comparison of LULC dynamics. The SRTM DEM data is used to delineate the basin area of the Lower Turag River (Table 1), which proves its validity and reliability for hydrological applications. The drainage networks and watershed boundaries are extracted using hydrological tools in the GIS (Mishina et al., 2015; Rastogi et al., 2018).

**Table 1.** Datasets used in this study

| Data type and source | Dataset/product | Years | Spatial resolution/unit |
|---|---|---|---|
| Satellite imagery (https://earthexplorer.usgs.gov/) | Landsat 5 TM; Landsat 8 OLI (Collection 2 Tier 1 TOA Reflectance) | 2001, 2011, 2021 | 30 m |
| Elevation data (https://earthexplorer.usgs.gov/) | Shuttle Radar Topography Mission (SRTM) | Base DEM | 30 m |
| Hydrographic data (Lehner et al., 2008) | HydroSHEDS (HydroRIVERS) | Base map stage | Vector river network (line features) |
| Population data (BBS, 2003; 2015; 2023) (https://bbs.gov.bd/) | Population and Housing Census 2001, 2011 and 2022 | 2001, 2011, 2022 | Census administrative unit / mauza-level tabulation |
| Ancillary / reference data | Google Earth Pro, Field-based data | reference years | Point observations |

### 2.3 Supervised image classification

Images having cloud cover, which is less than 5%, have been accepted firstly and the outer boundary of the image was set based on the produced shape file of the Lower Turag basin from SRTM DEM data. Supervised image classification was employed using the Random Forest (RF) machine learning algorithm, which can handle high-dimensional data, and it is considered a robust classifier for image classification (Lai et al., 2022). Moreover, RF can accommodate both continuous and categorical variables, which is essential for LULC classification where various land cover types must be distinguished (Akumu et al., 2021). In terms of Random Forest's application to satellite imagery, studies have revealed that it performs better than other machine learning classifiers, such as Support Vector Machine (SVM) (Stehman, 2009; Prayogo, 2021). Therefore, using Random Forest (RF) classifier, LULC maps have been generated for the years 2001, 2011, and 2021. The LULC classes that were identified are built-up areas, seasonal cropland, natural vegetation, open space, and waterbodies (Table 2).

**Table 2**. Thematic description of the LULC classes

| LULC class | Thematic descriptions |
|---|---|
| Built-up | Impervious areas, occupied by residential houses and other buildings. |
| Seasonal cropland | Areas of land ploughed/prepared for growing crops, including fallow plots. |
| Natural vegetation | Land covered with a tree canopy or dominated by grass, bushes that were not primarily under cultivation |
| Open space | Bare landscape dominated by soil and outcrops, with very few plants and no trees |
| Water bodies | Areas of land covered with water (ponds, lakes, and rivers, etc.) |

### 2.4 Accuracy assessment

We took a total of 500 ground truth points, which were selected based on extensive field survey, consulting with local people, and extracting points from Google Earth Pro. The samples were selected using a stratified random sampling approach across the five LULC classes to ensure adequate representation of each category. Among the total samples, 70% were used as training data for the RF classifier, and the remaining 30% were used for validation. Confusion among land types, such as vegetation, exposed soil, fallow cropland, and built-up surfaces, is usually a problem with moderate-resolution Landsat images. To reduce this confusion, key spectral indices, including Normalized Difference Vegetation Index (NDVI), Normalized Difference Built-up Index (NDBI), Modified Normalized Difference Water Index (MNDWI), and Soil Adjusted Vegetation Index (SAVI), were incorporated. To reduce cloud cover and seasonal variability, dry-season median composites (November–February) were taken. Water pixels within the MNDWI thresholds were used to isolate water pixels, whereas the SWIR and NDBI were used to enhance the discrimination between the impervious surfaces and the bare soil. The Random Forest classifier was trained using 100 decision trees. Across the reference years 2001, 2011, and 2021, the overall classification accuracy was 96%, 91%, and 90%, respectively, while the kappa coefficients were 0.95, 0.89, and 0.87. These results indicate a strong agreement between the classified maps and reference data, confirming the reliability of the LULC classification.

### 2.5 Detection of land use and land cover changes

Using the remap function, recategorization of the land cover maps has been done for the years 2001, 2011, and 2021. This allows one to compare across time within the five original classes (C0, C1, C2, C3, C4) consistently with five new codes equivalent to (1, 2, 3, 4, 5). After that, two reclassified images are combined to identify the land cover transitions from 2001 to 2011 and from 2011 to 2021. To differentiate between each change pattern, a "Transition" code is then generated using the multiply(100).add() operation for the respective years. Subsequently, the transition matrix is used, which defines the frequency of each transition type active within the specified geometry region. This matrix gives an aggregate of all associated movement within the study area. To calculate the area of the space that would correspond to each transition, the code generates an image layer, and the pixel area is calculated, which then calculates the total area for each transition type by summing pixel areas within each unique transition category. Then, a summary of transition areas (in square kilometers) for each change type is produced using a grouped-sum reducer in GEE.

**2.6 Population raster validation and allocation**

For distributing population to each region, mauza-level population is distributed to the built-up area of each mauza, as residents are mainly concentrated in residential and mixed-use built-up zones rather than other land types (i.e., waterbody, cropland, or bare land). This reduces the spatial errors which are common in the uniform areal-weighting approaches. Using fishnet, 1 $km^2$ grid cells are created and overlaid on the study area. Based on the percentage of built-up areas in each grid, the proportional distribution of population is calculated and distributed among those grids across the study area. The gridded data were checked by comparing the aggregated grid level sums with the official mauza census data, and the results indicated a disparity of less than 0.5%. This reaffirms the fact that the proportional allocation method gives adequate estimates when calculating LCRPGR.

**2.7 Land consumption rate to population growth rate (LCRPGR) calculation**

The Land Consumption Rate (LCR) and Population Growth Rate (PGR) across the Turag River basin were calculated from 2001 to 2011 and 2011-2021, following the methodology recommended for SDG Indicator 11.3.1 by UN-Habitat and the United Nations Statistics Division (UN-Habitat, 2018; UNSD, 2021). The formulation of LCR and PGR follows the standard SDG 11.3.1 framework and is consistent with our previous study, where a similar ratio was applied to assess agricultural land consumption relative to population growth (Malek et al., 2024). As the metadata suggests decennial interval for the estimation, that is why 2001, 2011, and 2021, having a 10-year interval, have been taken here for detecting the temporal changes of LULC. However, the population data is available from the Population and Housing Census survey for the years 2001, 2011 and 2022. There is a one-year mismatch between the 2021 built-up dataset and the 2022 population data, which is acceptable within a decadal interval and does not affect annualized LCR or PGR computations. Moreover, SDG 11.3.1 allows using the closest available years. Based on the Land Use Efficiency calculation, we classified the entire area into urban center, urban cluster, and rural grids following the UN-Habitat-provided definition.

$$\text{Land Consumption Rate (LCR)} = \frac{\text{Vpresent} - \text{Vpast}}{\text{Vpast}} \times \frac{1}{(\text{t})} \ldots\ldots.(1)$$

Where, $V_{present}$ is the total built-up area in the current year; $V_{past}t$ is total built-up area in the past year; t is the number of years between $V_{present}$ and $V_{past}$ (or length in years of the period considered)

$$\text{Population Growth Rate (PGR)} = \frac{\text{LN}(\text{Pop}_{\text{t+n}}/\text{Pop}_{\text{t}})}{(\text{y})} \ldots\ldots\ldots (2)$$

Where, *LN* is the natural logarithm value; $Pop_t$ is the total population within the urban area/city in the past/initial year; $Pop_{t+n}$ is the total population within the urban area/city in the current/final year; *y* is the number of years between the two measurement periods

$$\text{LCRPGR/LUE} = \left(\frac{\text{Land Consumption rate}}{\text{Population growth rate}}\right)\ldots\ldots\ldots\ldots(3)$$

The overall formula is based on EUC (2020) and can be summarized as:

$$\text{LCRPGR} = \left(\frac{\text{Vpresent}-\text{Vpast}}{\text{Vpast}} * \frac{1}{\text{T}}\right) \Bigg/ \left(\frac{\text{LN}\left(\frac{\text{Pop}_{t+n}}{\text{Pop}_{t}}\right)}{\text{y}}\right)\ldots\ldots(4)$$

### 2.8 Grid classification method

Based on the definition of the degree of urbanization provided by UN-Habitat, the following three types of grid cells have been acknowledged. An urban center (high-density cluster) consists of contiguous grid cells with a population density of at least 1,500 people per sq.km and a total population of at least 50,000. In terms of an urban cluster, it is defined as contiguous grid cells with a population density of at least 300 people per sq.km and a minimum population of 5,000. Grid cells that do not meet these criteria are classified as rural cells, generally characterized by population densities below 300 people per sq.km (Karakuş et al., 2017).

**Table. 3** Urban–rural classification based on population and built-up criteria

| Grid Type | Logic (Degree of Urbanization) |
|---|---|
| Urban Center | 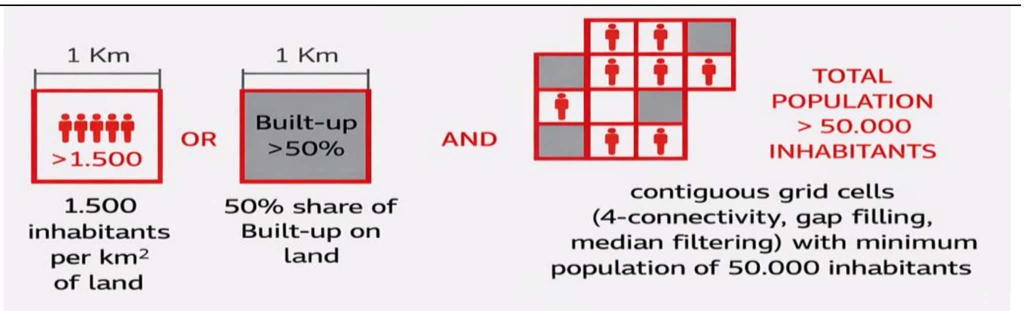  |
| Urban Cluster | 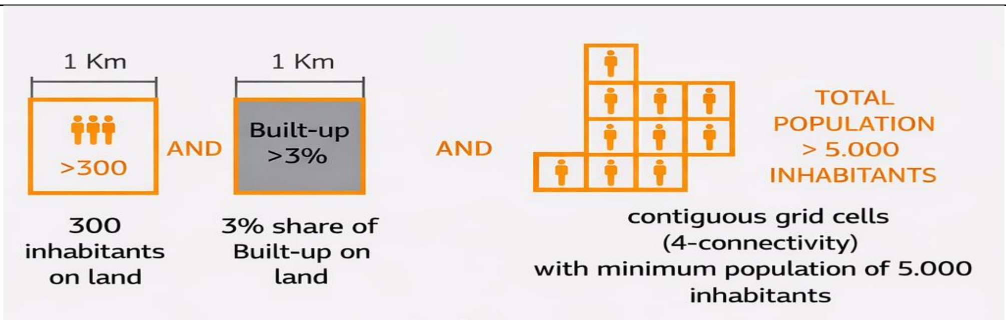  |
| Rural |   |

Source: European Commission, Joint Research Centre (JRC), GHSL, 2024.

## 3. Results

### 3.1 Land cover dynamics over two decades (2001-2021)

The substantial temporal dynamics in LULC for two decades are discussed in Fig. 2. Analysis of land use in 2001 revealed that the study area is predominantly agricultural land, which covers 131 sq.km (51%), while built-up area was only 41.8 sq.km (16%). Waterbodies comprised at least 17 sq.km, or as 7% of the area. Essentially, the amount of open space and natural vegetation was larger than the water body area and covered about 25 sq.km (10%) and 38 sq.km (15%), respectively. The status in 2011 revealed that agricultural land has significantly reduced, while the built-up areas have grown significantly. Agricultural land was reduced to 99 sq.km, representing 39% of the area and the built-up areas increased to 82 sq.km or 33%. Other types of land and vegetation also registered small expansion, with waterbodies occupying 18 sq.km, while open spaces occupied 30 sq.km. But then they noted that natural vegetation shrank to 22 sq.km during the same period of time. Finally, in 2021, the built-up area continued to expand and covered 40% of the lower Turag Basin, having an area of 100 sq.km, while the reduction of agricultural land to 82 sq.km was seen. Over the years, water bodies and open space also decreased, while the vegetation cover has expanded. Along with other notable transformations, 17 sq.km of agricultural land from the year 2011 has transformed into natural vegetation in 2021.

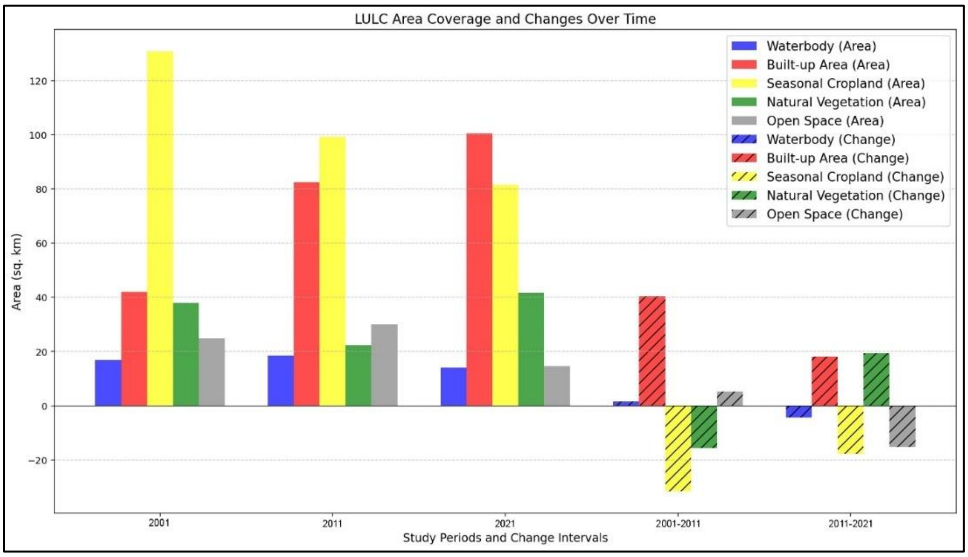


**Fig. 2.** The LULC area coverage and changes over the period (2001-2021). The positive changes suggest an increase/gain and the negative values indicate a decrease/loss in the status of land use types.

### 3.2 Accuracy assessment of LULC

The accuracy assessment result of the overall categorization for the years 2001, 2011, and 2021 is between 87 to 95%. Kappa values above 0.8 are often interpreted as indicating "almost perfect" agreement, while values between 0.6 and 0.8 suggest substantial agreement. Moreover, a Kappa coefficient above 0.8 signifies a robust classification (Fernández & Morales, 2019). Here, all the classified images have shown a kappa coefficient above 0.80. The Kappa accuracy for the maps of 2001, 2011, and 2021 is 0.95, 0.89, and 0.87, respectively. Here, the overall accuracy is also high, having 0.96, 0.91, and 0.90 for the maps of 2001, 2011, and 2021. A limited field validation was conducted in Savar Upazila to verify selected land use classes. Though extensive field surveys across the entire basin were not possible due to logistical constraints; therefore, additional validation points were derived from high-resolution Google Earth imagery and local knowledge. However, it is assumed that there is a strong relationship between the classified image and the field-based observation.

### 3.3 Population and built-up area distribution

The population density gradients and spatial concentration patterns are interpreted to explain high-growth hotspots and low-density zones (Fig. 3). Here, based on the range of population point density values, population is distributed into 10 classes with an interval of 20,000. In the year 2001, the level of overall population densification was relatively low, and most of them were concentrated in the southeast part of the study area. However, by 2011, signs of an increase were clearly visible, especially in the southern parts of the basin, representing Dhaka North City Corporation (DNCC) and a very small portion of Gazipur City Corporation (GCC). In the map of the 2022 population density distribution, a sharp increase in population all over the surrounding area and especially the southwestern portion was observed.

The gradual intensification of the process of urbanization was shown in Fig. 4. The built-up density was quite low in the year 2001, still the area with high density, 0.9 to 1.2 units, was observed only in the north-eastern part of the DNCC within the study area. However, from 2011, there are signs of urbanization towards the north from the existing high-density urban area in 2001, creating a built-up area belt which became extremely dense by the end of the latter decade. With urbanization expected to increase by 2021, most of the southern part of Savar Upazila has been transformed into an urban fabric as a result of industrial growth and real estate development alongside population growth.

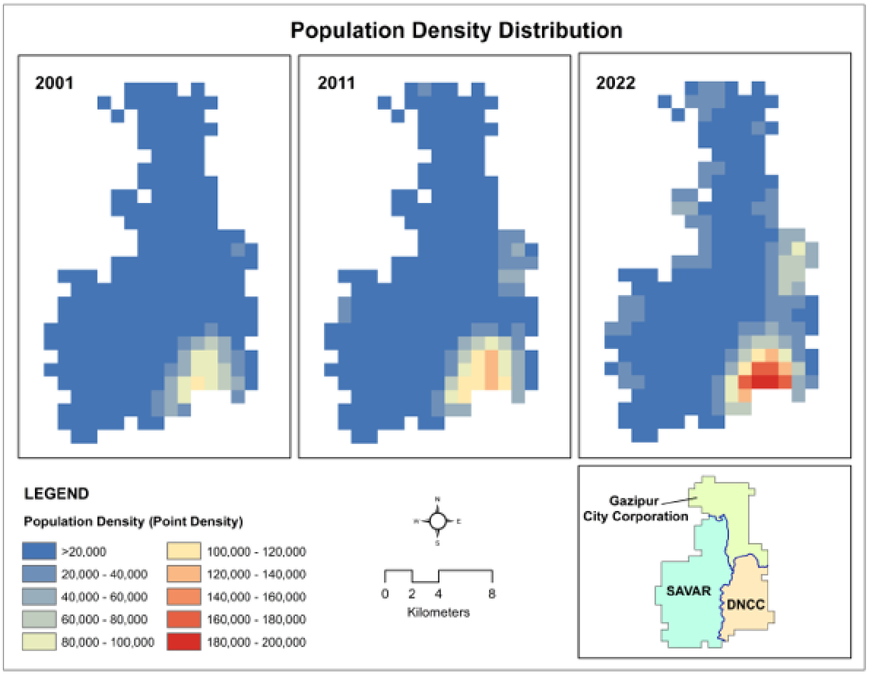


**Fig. 3.** Map of population density distribution

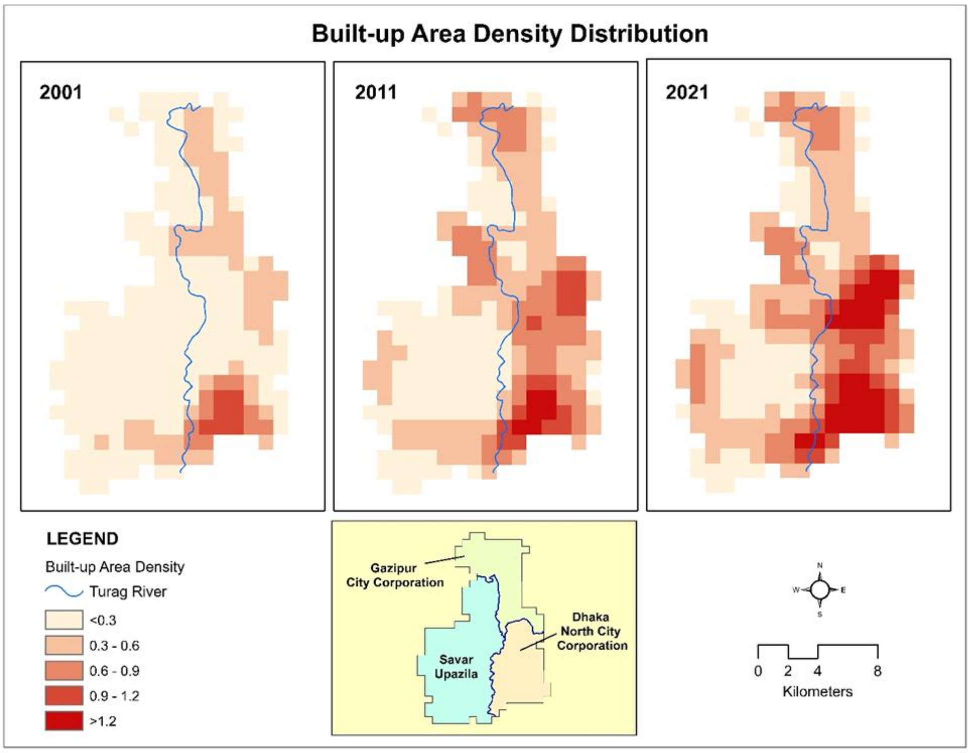


**Fig. 4.** Built-up area density distribution over time

### 3.4 Grid classification and transformation

The identification of grid cell transformations, presented in Table 4, in the study area over a period of twenty years reflects an extremely dynamic urbanization process due to escalating population density and rapid increase of infrastructure. The information shows that the portion of Rural grids has decreased from 39% in 2001 to only 15% in 2021, while that of the Urban increased from 36% to up to 76% in the same year showed in Table 4. This shift is more evidenced by the changing spatial proportions of urban growth and the consequent reduction of rural territory. During the period from 2001 to 2011, most of the transformations occurred in the central rural grids of the study area, where the population increased rapidly, leading to a rise in built-up areas. Between 2011 and 2021, this entire area transformed into a city, with each grid now appearing as part of the urban landscape. (Fig. 5). The grid classification was derived by overlaying the built-up density layer (Fig. 4) with population thresholds defined under the degree of urbanization framework. The full methodology to assess the degree of urbanization and classify each cell as Urban Center, Urban Cluster, and Rural in Fig. 5 is described in the supplementary document.

**Table 4.** Different types of grid count in percentage within the study area

| Grid type (%) | 2001 | 2011 | 2021 |
|---|---|---|---|
| Rural | 39 | 27 | 15 |
| Urban Center | 36 | 67 | 76 |
| Urban Cluster | 25 | 6 | 9 |

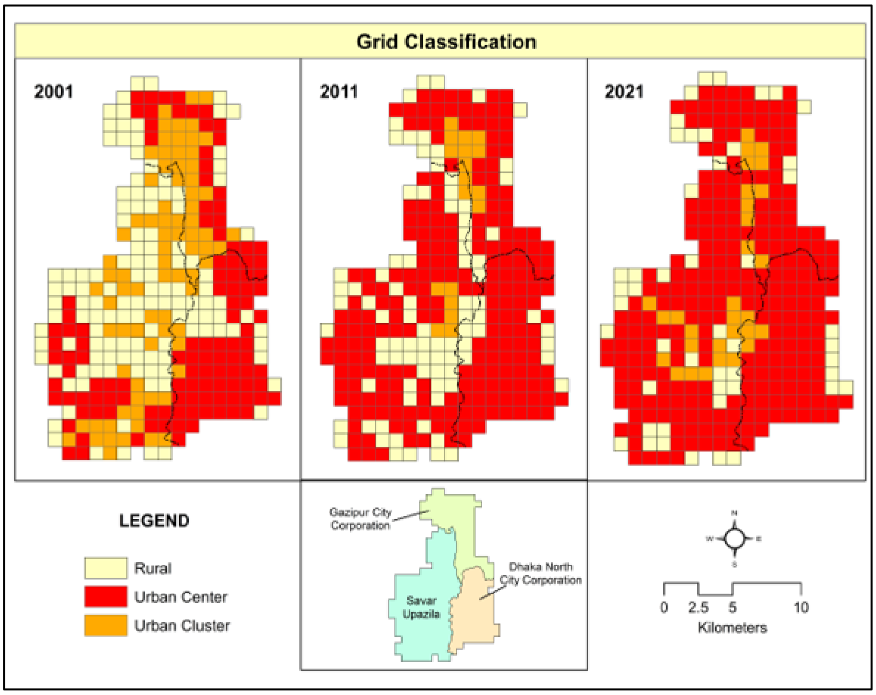


**Fig. 5.** Grid classification map of lower Turag Basin

The changes in the intensity and dynamism of the land grid cells in the study area over two decades, based on the degree of urbanization has been presented in Fig. 6. It employs forms and color codes to present some of the transformations. The red grids depict regions that were rural in 2001, though have urban regions in 2021. Fig. 6 presents the spatial stability and transformation of 1 sq.km grid cells classified according to the Degree of Urbanization framework provided by UN-Habitat. The small inset map (top-left) summarizes the overall grid dynamics into two broad categories: Stable grids (yellow), which retained the same classification between 2001 and 2021 (i.e., rural remained rural, urban cluster remained cluster, and urban center remained center), and Dynamic grids (pink), which experienced at least one category change during the study period. This inset provides a simplified overview of spatial stability versus change. The larger map expands this classification into six detailed transformation types. Stable grids are subdivided into three subclasses representing grids that consistently remained (i) rural, (ii) urban cluster, or (iii) urban center over the entire period. Dynamic grids are also divided into three subclasses based on the direction of transition: (i) rural to urban center (shown in red), indicating rapid urban intensification; (ii) urban cluster to urban center (orange), representing progressive densification and outward expansion from existing cores; and (iii) mixed or reverse transitions (yellow), reflecting haphazard or non-linear development patterns. These mixed transitions occur due to the redistribution of population within built-up areas during proportional grid-based population allocation. Since population is strategically disaggregated according to built-up density within each grid, some cells exhibit apparent shifts (e.g., center to cluster or cluster to rural) driven by internal demographic redistribution rather than physical land reversion. Therefore, the small and large maps present the same dataset at different levels of aggregation: the inset shows overall stability versus change, while the main map details the specific transformation trajectories and intensity of urban restructuring across the Lower Turag Basin.

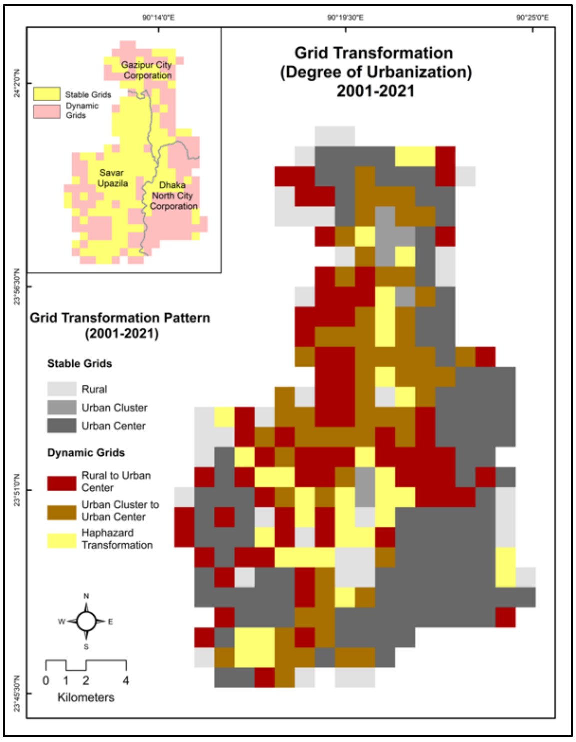


**Fig. 6.** Grid transformation within the study area (2001–2021)

### 3.5 Ratio of land consumption rate to population growth rate

The relationship between land consumption and population growth in the study area over three distinct years: 2001, 2011, and 2021, is clearly visible in Table 5. The value obtained from the calculation of LCRPGR is a meaningful figure offered by the UN-Habitat to arrive at SDG Indicator 11.3.1. The value of more than 1 indicates that land consumption is outpacing population growth. On the other hand, a value below 1 shows efficient land use of the area under consideration. The population density has grown tremendously over the years, from roughly 1.9 million in 2001 to more than 5 million in 2022, which was used for the 2021 analysis, because the 2021 census was delayed. As the urban extent grows, the built-up area per capita changes, reflecting how land is allocated on a per-person basis. Between 2001 and 2021, the built-up area increased nearly double and reached at 96.2 percent, which indicates intense expansion of urban areas. Likewise, a higher LCR means the accelerated use of land, converting other areas into impervious areas. Built-up area increased from 41.97 sq.km in 2001 to 100.45 sq.km in 2021, corresponding to a 139.39%. Similarly, the population increased from 1,908,148 to 5,031,092, representing a 163.71% increase over the same period. In the period between 2001 and 2011, the PGR was higher and recorded 5.4 percent. However, for the period between 2011 to 2022, the growth rate reduced to 3.8 percent. The highest LCRPGR of 1.775 between 2001 and 2011 suggests that land consumption far outpaced population growth. Over time, the pattern of urbanization changed from uncontrolled to a relatively controlled type, where the LCRPGR decreased to 0.513 in 2021. Though the built-up area continued to grow, the rate of its growth was slower than the rate of population growth. Thus, the first decade reflects unsustainable land consumption (LCRPGR > 1), whereas the second decade shows improved but still evolving land-use efficiency (LCRPGR < 1).

**Table 5.** Land consumption rate to population growth rate

| Year | Population | Built-up Area (sq.km) | Built-up Area (m²) | Built-up Area per Capita (m²) | Built-up Change (%) | LCR (annual) | PGR | LCRPGR |
|---|---|---|---|---|---|---|---|---|
| 2001 | 1,908,148 | 41.97 | 41,967,694 | 21.993 | – | – | – | – |
| 2011 | 3,282,034 | 82.37 | 82,371,226 | 25.097 | 0.962 | 0.096 | 0.054 | 1.775 |
| 2021 | 5,031,092 | 100.45 | 100,455,421 | 19.966 | 0.219 | 0.019 | 0.038 | 0.513 |

## 4.0 Discussion

### 4.1 Urban morphological dynamics

In the case of the Lower Turag River Basin, the entire area was predominantly rural with most of the land occupied by seasonal croplands, except the southeastern part having small area of urban fabric which has transformed into a completely urban agglomeration within two decades. The LULC transformation over two decades gives us a crystal-clear message that agricultural land is consumed faster than any other land type, and the built-up area is expanding at a frenetic pace. Every other land type is being reduced over time except built-up. Though the early decade depicted the increase of barren land with a slight increase of water bodies, which later reduced, and the latter decade shows a dramatic escalation of the natural growth of vegetation. This anomaly has a deep-rooted, strong connection. This seeming paradox is mostly attributed to transformations in cropland. Many croplands that had been productive in the first decade slowly turned barren due to constant industrial pollution, especially by the brickfields, tanneries, and garment-processing plants along the basin. With the reduced productivity of the soil, a high proportion of farmers abandoned agriculture to turn to industrial jobs. Fallow lands were then left idle, and, in the process, the natural vegetation and shrub cover grew. These regenerated fallow lands had higher NDVI values, which were categorized as vegetation during the latter decade. The vegetation growth in 2011-2021 is an indication of the natural vegetation regeneration on abandoned and degraded farmlands, not an indication of improved ecological conservation. Lambin and Meyfroidt (2010) identified the regeneration of vegetation on abandoned agricultural land as a key component of vegetation transitions driven by socioeconomic shifts, such as economic development.

The built-up area and population density distribution in 2001 reflect early phases of urban growth, which belong to DNCC at present, and highly populated areas are spreading more widely across the southern regions, mostly, however, also increasing towards the north and east, indicating rising demand for residential and commercial spaces. Lower concentration of population and a slower pace of urbanization have been shown in the central portion of the study area along the banks of the Lower Turag River. A sharp spatial alignment between population and impervious area expansion pattern is visible, where moderate to high density areas were extending from the high density /core area in DNCC towards Gazipur City Corporation. This clear visualization of a south-to-northward directional transformation of the city area is also evident from previous studies (Dewan and Yamaguchi, 2009). This urbanization was triggered by the prior population growth and their growing need for residential and commercial demands, which required improved connectivity and transportation facilities. Alongside, the southern and central portions of the basin have experienced intensified industrial expansion, where export-processing zones, garment factories, and ancillary services have attracted large volumes of migrant labor. These drivers explain the intense increase in built-up area and the high LCRPGR value during the first decade. These results are consistent with findings from other rapidly urbanizing regions, where early stages of urban growth are often characterized by high land consumption rates followed by gradual densification (Angel et al., 2011; Melchiorri et al., 2019)

### 4.2 LCRPGR in urban sustainability

The land consumption and population dynamics highlight important implications for urban sustainability in relation to SDG Indicator 11.3.1. The high LCRPGR value during 2001–2011 indicates inefficient land use and rapid urban sprawl, while the reduced value in the following decade reflects a relative improvement in land-use efficiency. However, the continued expansion of built-up areas into agricultural and ecologically sensitive zones signals ongoing pressure on food security, flood regulation, and environmental stability. These findings suggest that although urban growth has become somewhat more efficient, the pace and pattern of expansion still pose challenges for achieving sustainable land-use configurations in the basin. Moreover, the transforming grids are most noticeable in the southern and central parts of the study area close to the Lower Turag River, visible in Fig. 6. The availability of water has been instrumental in the expansion, hence leading to the conversion of rural land to urban use. The spatial patterns of land conversion reveal clear gaps in urban planning and regulatory enforcement. Areas designated as flood retention zones and ecological buffers in planning documents have undergone significant encroachment, reflecting weak implementation of land-use rules. These trends underscore the need for stronger integration of geospatial monitoring tools, such as LCRPGR-based assessments, into regular planning workflows. Improved zoning enforcement, compact development strategies, and protection of agricultural and wetland zones will be critical for managing future growth while reducing exposure to flooding and ecological degradation.

Interpretation of the detected patterns should consider certain limitations. Moderate-resolution Landsat imagery may obscure fine-scale heterogeneity, and misclassification between bare soil, fallow cropland, and built-up surfaces remains possible in densely changing environments. Logistical constraints to conduct extensive field surveys were another limitation. Population estimates rely on decadal census data, with the most recent count offset by one year from the 2021 LULC dataset, although this discrepancy is minimal for annualized change computations. Future assessments could benefit from integrating higher-resolution imagery, multi-source datasets, and more frequent population updates to reduce uncertainty.

## 5. Conclusions

This study examined the spatio-temporal dynamics of urban morphological change in the Lower Turag River Basin between 2001 and 2021 using multi-temporal Landsat imagery processed within the GEE platform. The results reveal a substantial expansion of built-up areas, largely driven by population growth, industrial development, and increasing demand for residential and commercial land. This rapid urban expansion has occurred primarily at the expense of agricultural land and natural vegetation, highlighting growing pressure on land resources and potential environmental consequences. Specifically, built-up areas increased by 139.39% between 2001 and 2021, while the population grew by 163.71%, reflecting intense urban transformation and land conversion dynamics. The analysis of LCRPGR indicates that urban land consumption exceeded population growth during the early decade (2001–2011), suggesting inefficient land use and unsustainable urban sprawl during the early phase of development. Although the LCRPGR value decreased in the following decade (2011–2021), indicating relatively improved land-use efficiency, continued encroachment of built-up areas into agricultural and ecologically sensitive zones remains a concern. The shift from an LCRPGR value of 1.775 (2001–2011) to 0.513 (2011–2021) indicates a transition from highly inefficient land consumption toward relatively improved, yet still evolving, urban land-use efficiency. Besides, this study demonstrates the effectiveness of GEE for analyzing long-term LULC changes and monitoring urban growth dynamics using cloud-based geospatial processing for understanding urbanization patterns and supporting evidence-based land-use planning. These findings directly reflect the performance of SDG Indicator 11.3.1, highlighting the imbalance between land consumption and population growth in rapidly urbanizing peri-urban regions. Overall, the findings highlight the need for sustainable urban development strategies, including improved land-use planning, protection of agricultural and wetland areas, and stronger enforcement of zoning regulations. Furthermore, integrating geospatial monitoring approaches such as LCRPGR-based assessments into urban management frameworks can support more balanced and sustainable urban growth in rapidly developing regions like the Lower Turag River Basin. Future research could incorporate higher-resolution datasets, more frequent population updates, and expanded field validation to further refine assessments of urban land-use efficiency and environmental impacts.

**Acknowledgments**

The authors would like to thank the USGS for providing the satellite data.

**Data availability**

The data will be made available upon request to the corresponding author.

**Conflict of interest**

The authors declare that there is no conflict of interest regarding the publication of this paper.

## References

Abbasi, M., Popy, S., Tan, Y. (2022). Quantifying spatiotemporal changes of the urban impervious surface of Dhaka district using remote sensing technology. Indonesia Journal of Geography 54 (3). https://doi.org/10.22146/ijg.72506

Aghlmand, M., Kaplan, G. (2021). Monitoring urban expansion using remote-sensing data aided by Google Earth Engine. European Journal of Geoscience 3(1), 1–8. https://doi.org/10.34154/2021-EJGS-0012/euraass

Akumu, C., Smith, R., Haile, S. (2021). Mapping and monitoring the canopy cover and greenness of southern yellow pines (loblolly, shortleaf, and Virginia pines) in central-eastern Tennessee using multi-temporal Landsat satellite data. Forests 12(4), 499. https://doi.org/10.3390/f12040499

Alam, K. (2003). Cleaning up of the Bunganga River, integrating the environment into decision making. PhD Dissertation, Murdoch University.

Amani, M., Ghorbanian, A., Ahmadi, S., Kakooei, M., Moghimi, A., Mirmazloumi, S. M. (2020). Google Earth Engine cloud computing platform for remote sensing big data applications: a comprehensive review. IEEE Journal of Selected Topics in Applied Earth Observations and Remote Sensing 13, 5326–5350. https://doi.org/10.1109/JSTARS.2020.3021052

Angel, S., Parent, J., Civco, D. L., Blei, A., Potere, D. (2011). The dimensions of global urban expansion: Estimates and projections for all countries, 2000–2050. Progress in Planning 75(2), 53–107. https://doi.org/10.1016/j.progress.2011.04.001

BBS (Bangladesh Bureau of Statistics). (2003, 2015, 2023). Population and Housing Census (2001, 2011, 2022). Government of Bangladesh. http://www.bbs.gov.bd

Census (2023) Banglapedia: The National Encyclopedia of Bangladesh. Available at: https://en.banglapedia.org/index.php/Census.

Choudhury, G.A., Choudhury, A. (2004). An assessment of water resources and flood management of Dhaka city. In: Water resources management and development in Dhaka City, Geothe-Institute, pp 35–47.

Cuypers, S., Nascetti, A., Vergauwen, M. (2023). Land use and land cover mapping with VHR and Multi-Temporal Sentinel-2 Imagery. Remote Sensing, 15(10). https://doi.org/10.3390/rs15102501

Dewan, A. M., Yamaguchi, Y. (2008). Using remote sensing and GIS to detect and monitor land use and land cover change in Dhaka metropolitan of Bangladesh during 1960–2005. Environmental Monitoring and Assessment 150(1–4), 237–249. https://doi.org/10.1007/s10661-008-0226-5

EUC (European Commission). (2020) Items for discussion and decision: demographic statistics –a recommendation on the method to delineate cities, urban and rural areas for international statistical comparisons. Prepared by the European Commission, Eurostat and DG for Regional and Urban Policy–ILO, FAO, OECD, UN-Habitat, World Bank. https://unstats.un.org/unsd/statcom/51st-session/documents/BG-Item3j-Recommendation-E.pdf

European Commission, Joint Research Centre (JRC) (2024) Global Human Settlement Layer (GHSL): Concepts and methods behind the data produced by the GHSL. https://human-settlement.emergency.copernicus.eu/images/Basics_3_01.png

Fernández, I., Morales, N. (2019). One-class land-cover classification using MaxEnt: the effect of modelling parameterization on classification accuracy. PeerJ 7, e7016. https://doi.org/10.7717/peerj.7016

Ghazaryan, G., Rienow, A., Oldenburg, C., Thonfeld, F., Trampnau, B., Sticksel, S., Jürgens, C. (2021). Monitoring of urban sprawl and densification processes in western Germany in the light of SDG Indicator 11.3.1 Based on an Automated Retrospective Classification Approach. Remote Sensing, 13(9). https://doi.org/10.3390/rs13091694

Huq, M.H., Rahman, M.M. (2022). Sustainability of rainwater management and land-use compliance – a case of greater Dhaka. International Journal of Latest Engineering Research and Applications 7(10), 38–61.

Jahan, K., Pradhanang, S. M., Ehsan Bhuiyan, M. A. (2021). Surface runoff responses to suburban growth: an integration of remote sensing, GIS, and Curve Number. Land, 10(5). https://doi.org/10.3390/land10050452

Karakuş, P., Karabork, H., Kaya, S. (2017). A comparison of the classification accuracies in determining the land cover of Kadirli region of Turkey by using the pixel based and object based classification algorithms. International Journal of Engineering and Geosciences, 2(2), 52-60. https://doi.org/10.26833/ijeg.298951

Kelly-Fair, M., Gopal, S., Koch, M., Kusumaningrum, H. P., Helmi, M., Khairunnisa, D., Kaufman, L. (2022). Analysis of Land Use and Land Cover Changes through the Lens of SDGs in Semarang, Indonesia. Sustainability, 14(13). https://doi.org/10.3390/su14137592

Lai, S. W., Fan, Y. L., Zhu, Y. H., Zhang, F., Guo, Z., Wang, B., Wan, Z., Liu, P. L., Yu, N., Qin, H. D. (2022). Machine learning-based dynamic prediction of lateral lymph node metastasis in patients with papillary thyroid cancer. Frontiers in Endocrinology, 13, 1019037. https://doi.org/10.3389/fendo.2022.1019037

Lambin, E. F., Meyfroidt, P. (2010). Land use transitions: Socio-ecological feedback versus socio-economic change. Land Use Policy 27(2), 108–118. https://doi.org/10.1016/j.landusepol.2009.09.003

Lehner, B., Verdin, K., Jarvis, A. (2008). New global hydrography derived from spaceborne elevation data. Eos, Transactions American Geophysical Union, 89(10), 93–94. https://www.hydrosheds.org

Malek, M. B., Shahed, M. H., Shabab, K. J., Habib, M. A., Rashid, M. S. (2024). Monitoring urban growth and its impact on arable land consumption in the Lower Turag Basin of Dhaka: A Google Earth Engine based study. Journal of Geographic Information System, 16(6). https://doi.org/10.4236/jgis.2024.166024

Melchiorri, M., Florczyk, A. J., Freire, S., Schiavina, M., Pesaresi, M., Kemper, T. (2018). Unveiling 25 years of planetary urbanization with remote sensing: perspectives from the global human settlement layer. Remote Sensing, 10(5). https://doi.org/10.3390/rs10050768

Melchiorri, M., Pesaresi, M., Florczyk, A. J., Corbane, C., Kemper, T. (2019). Principles and applications of the global human settlement layer as baseline for the land use efficiency indicator—SDG 11.3.1. ISPRS International Journal of Geo-Information, 8(2). https://doi.org/10.3390/ijgi8020096

Mishina, Y., Murata, R., Yamauchi, Y., Yamashita, T., Fujiyoshi, H. (2015). Boosted random forest. IEICE Trans Inf Syst E98.D(9), 1630–1636. https://doi.org/10.1587/transinf.2014OPP0004

Moniruzzaman, M., Thakur, P. K., Kumar, P., Alam, M. A., Garg, V., Rousta, I., Olafsson, H. (2020). Decadal urban land use/land cover changes and its impact on surface runoff potential for the Dhaka city and surroundings using remote sensing. Remote Sensing, 13(1). https://doi.org/10.3390/rs13010083

Mortoja, M. G., Yigitcanlar, T. (2020). How does peri-urbanization trigger climate change vulnerabilities? An investigation of the Dhaka megacity in Bangladesh. Remote Sensing, 12(23). https://doi.org/10.3390/rs12233938

Mosammam, H. M., Nia, J. T., Khani, H., Teymouri, A., Kazemi, M. (2017). Monitoring land use change and measuring urban sprawl based on its spatial forms: The case of Qom city. The Egyptian Journal of Remote Sensing and Space Sciences, 20(1), 103-116. https://doi.org/10.1016/j.ejrs.2016.08.002

Mundi, A. (2019). Rights of nature case study Turag River. http://files.harmonywithnatureun.org/uploads/upload1130.pdf

Mutanga, O., Kumar, L. (2019). Google Earth Engine applications. Remote Sensing 11(5). https://doi.org/10.3390/rs11050591

Pour, N. M., Oja, T. (2021). Urban Expansion Simulated by Integrated Cellular Automata and Agent-Based Models; An Example of Tallinn, Estonia. Urban Science, 5(4). https://doi.org/10.3390/urbansci5040085

Prayogo, L. (2021). Mangrove vegetation mapping using Sentinel-2A imagery based on Google Earth Engine cloud computing platform. International Journal of Science, Engineering and Information Technology, 6(1), 249–255. https://doi.org/10.21107/ijseit.v6i1.12175

Rahman, M., Islam, M. M., Kim, H. J., Sadiq, S., Alam, M., Siddiqua, T., Mamun, M. A., Hossen Gazi, M. A., Raju, M. R., Chen, N., Hossain, M. A., Dewan, A. (2023). Assessing the Influence of Land Cover and Climate Change Impacts on Runoff Patterns Using CA-ANN Model and CMIP6 Data. ISPRS International Journal of Geo-Information, 12(10). https://doi.org/10.3390/ijgi12100401

Rastogi, A. K., Thakur, P. K., Rao, G. S., Aggarwal, S. P., Dadhwal, V. K., Chauhan, P. (2018). Integrated flood study of Bagmati River basin with hydro processing, flood inundation mapping and 1-D hydrodynamic modeling using remote sensing and GIS. ISPRS Annals of the Photogrammetry, Remote Sensing and Spatial Information Sciences, IV-5,165–172. https://doi.org/10.5194/isprs-annals-iv-5-165-2018

Stehman, S.V. (2009). Sampling designs for accuracy assessment of land cover. International Journal of Remote Sensing, 30(20), 5243–5272. https://doi.org/10.1080/01431160903131000

Tabunshchik, V., Gorbunov, R., Gorbunova, T., Pham, C. N., Klyuchkina, A. (2023). Identification of river basins within northwestern slope of Crimean Mountains using various digital elevation models (ASTER GDEM, ALOS World 3D, Copernicus DEM, and SRTM DEM). Frontiers in Earth Science, 11, 1218823. https://doi.org/10.3389/feart.2023.1218823

Teklemariam, N. (2022). Sustainable development goals and equity in urban planning: a comparative analysis of Chicago, São Paulo, and Delhi. Sustainability, 14(20). https://doi.org/10.3390/su142013227

Uddin, H. M. (2005). Initial environmental impact assessment of the Turag–Buriganga naval transport. Master’s thesis, Department of Geography and Environment, Jahangirnagar University, Savar, Dhaka, Bangladesh.

UN-Habitat (2018) SDG Indicator 11.3.1 Training Module: Land Use Efficiency. United Nations Human Settlements Programme (UN-Habitat), Nairobi. https://unhabitat.org/sites/default/files/2021/08/indicator_11.3.1_training_module_land_use_efficiency.pdf

United Nations, Department of Economic and Social Affairs, Population Division (2019). World urbanization prospects: The 2018 revision (ST/ESA/SER.A/420). United Nations, New York. https://population.un.org/wup/assets/WUP2018-Report.pdf

UNSD (United Nations Statistics Division). (2021). Metadata for Sustainable Development Goal Indicator 11.3.1: Ratio of Land Consumption Rate to Population Growth Rate. United Nations Department of Economic and Social Affairs. https://unstats.un.org/sdgs/metadata/files/Metadata-11-03-01.pdf

USGS (United States Geological Survey). (2014). Shuttle Radar Topography Mission (SRTM) 1 Arc-Second Global. https://www.usgs.gov/centers/eros/science/usgs-eros-archive-digital-elevation-shuttle-radar-topography-mission-srtm

USGS (United States Geological Survey). (2020). Landsat Collection 2 Level-1 data. https://www.usgs.gov/landsat-missions/landsat-collection-2

Wiatkowska, B., Słodczyk, J., Stokowska, A. (2021). Spatial-Temporal land use and land cover changes in urban areas using remote sensing images and GIS Analysis: the case study of Opole, Poland. Geosciences, 11(8). https://doi.org/10.3390/geosciences11080312

# Guide for Authors

## A. Guidelines for writing and formatting

Manuscripts should be written in clear, concise, and grammatically correct English to be intelligible to the professional reader who is not a specialist in any particular field. The Journal of Remote Sensing and Environment offers *a free-format submission* for a simplified and streamlined submission process. However, the manuscript should contain the following sections sequentially.

> a) Abstract, b) Introduction, c) Materials and methods/Experimental set-up, d) Results and discussion, e) Conclusions, Acknowledgements (if any) and References.

***File format:*** We request you to provide an editable Word file for the entire submission (using the extension .doc/.docx). Font size of the writing should be 12 in Times New Roman with double spacing.

***Title page:*** Article titles should be concise, with a complete reflection of the study. Please avoid abbreviations and formulae. Provide the full name of each author with accurate spelling. Add present affiliation addresses and the email address of each author. Clearly indicate who will correspond during the whole publication process.

***Abstract:*** We ask you to provide a factual and brief abstract which should not exceed 300 words. The abstract should briefly state the purpose of your research, main results, and major conclusions. Avoid references if they are not essential.

***Keywords:*** You are required to provide 3 to 5 keywords. Please try to avoid keywords consisting of multiple words.

***Tables:*** Insert the tables in the body of the article. Tables must be submitted as editable text, not as images. Number the tables consecutively according to their appearance in the text. Please provide captions explicitly along with the tables. Place table notes below the body of the table (if necessary). Cite all tables in the manuscript text. Please, provide the tables which are necessary to show. We recommend that you use tables sparingly, ensuring that any data presented in tables is not duplicating results described elsewhere in the article.

***Figures, images, and artwork:*** Insert the Figures/images/diagrams in the body of the article. Do not paste the Figures/images/diagrams within a Table. Number the Figures consecutively according to their appearance in the text. Please provide captions explicitly below of each Figure. Cite all Figures in the manuscript text.

***Acknowledgements:*** Contributions from anyone who does not meet the criteria for authorship should be listed in an Acknowledgments section, with permission from the contributor. You can also mention the financial and material support information in this section. Acknowledgements should be placed in a separate section, which appears directly before the reference list.

***Reference and citation format:*** Any references cited within your article should also be present in your reference list and vice versa. Do not include unpublished results in the reference list. Author names, journal or book titles, chapter or article titles, year of publication, volume numbers, article numbers, or pagination must be included, where applicable. Use of DOIs is recommended. This journal prefers the Harvard reference style, i.e., the author, date system. In the text, give the author's name followed by the year in parentheses: Smith (2000). You should cite the statement (Smith, 2000) or (Smith and Robin, 2005) or (Smith et al., 2015) if the author number is one or two, or more than two, respectively. If several papers by the same authors and from the same year are cited, a, b, c, etc. should be inserted after the year of publication.

In the reference list, references should be listed in alphabetical order. Some examples are given below:

***Journals:*** Hurley, J.V. and Boos, W. R. (2015). A global climatology of monsoon low-pressure systems. *Quarterly Journal of the Royal Meteorological Society,* 141(689), 1049-1064. https://doi.org/10.1002/qj.2447

Sun, J., Fu, S., Wang, H., Zhang, Y., Chen, Y., Su, A., Wang, Y., Tang, H. and Ma, R. (2023). Primary characteristics of the extreme heavy rainfall event over Henan in July 2021. Atmospheric Science Letters, 24(1), p.e1131. https://doi.org/10.1002/asl.1131

***Books:*** Smith, J.A. and Brown, L. (2020). Climate variability and river systems. In: Johnson, P. and Lee, R. (eds.) Hydrology and Climate Change: An Integrated Approach. 2nd ed. London: Routledge, pp. 45–67.

Jones, L., Patel, R. and Wong, H. (2021). Ecosystem services and climate adaptation. In: Harrison, D. and Smith, B. (eds.) Climate Change and Natural Resources. Cambridge: Cambridge University Press, pp. 202–230.

***Newspapers:*** Print: Ionesco, J 2001, 'Federal election: new Chip in politics', The Advertiser 23 October, p. 10.

***From website:*** Hilts, PJ 1999, 'In forecasting their emotions, most people flunk out', The New York Times 16 February. Available from <http://www.nytimes.com>. [19 February 2000].

**B. Submission guidelines:** Manuscripts submitted before 01 March in each year should be considered for publication in the upcoming volume (30 June). The manuscript should be submitted as an email attachment to the Editorial Office at refatfaisal@yahoo.com and CC to jrse@sparrso.gov.bd, mentioning 'new manuscript submission' in the subject area.

**C. Publication Fee:** This journal does not charge any article processing fee for publication. The Journal will be published annually in June every year (Online and print versions). Each article is assigned a unique Digital Object Identifier (DOI), registered through Crossref to ensure global visibility.

For more information, please do not hesitate to contact us.

Editor

Journal of Remote Sensing and Environment.

Bangladesh Space Research and Remote Sensing Organization (SPARRSO),

Agargaon, Sher e-Bangla Nagar, Dhaka-1207.

E-mail: refatfaisal@yahoo.com or jrse@sparrso.gov.bd;

Cell no: +8801919491335 or +8801743677175;

Website: http://www.sparrso.gov.bd or

https://sites.google.com/view/jrse-sparrso-bd-com

Journal of Remote Sensing and Environment
Volume 5, 2026

## Table of Content



Mohakash Biggyan Bhaban, Agargaon, Sher-e-Bangla Nagar, Dhaka 1207, Bangladesh
Phone: +88-02-48117692, Fax: +88-02-48111169
E-mail: admin@sparrso.gov.bd or jrse@sparrso.gov.bd
Website : www.sparrso.gov.bd or https://sites.google.com/view/jrse-sparrso-bd-com/home